UNIVERSITY OF CALIFORNIA, SAN DIEGO

# Advanced Fluid–Structure Interaction Techniques in Application to Horizontal and Vertical Axis Wind Turbines

A dissertation submitted in partial satisfaction of the
requirements for the degree
Doctor of Philosophy

in

Structural Engineering with a Specialization in Computational Scince

by

Artem Korobenko

Committee in charge:

Professor Yuri Bazilevs, Chair
Professor David J. Benson
Professor Jiun-Shyan Chen
Professor Michael Holst
Professor Alison Lesley Marsden

2014





ProQuest LLC.
789 East Eisenhower Parkway
P.O. Box 1346
Ann Arbor, MI 48106 - 1346

The Dissertation of Artem Korobenko is approved, and it is acceptable in quality and form for publication on microfilm and electronically:

_____

_____

_____

_____

_____

Chair

University of California, San Diego

2014

DEDICATION

To my wife and my parents.

TABLE OF CONTENTS

LIST OF FIGURES

LIST OF TABLES

ACKNOWLEDGEMENTS

I would like to express all appreciation and gratefulness to my advisor, Prof. Yuri Bazilevs, for his invaluable help and guidelines during my research and beyond. His broad knowledge in a field of computational mechanics and adjacent areas inspired me to set a highest standard in academic research no mater how hard the problem could be. Without his helpful suggestions and encouragement this work would have not been possible.

I would also like to thank my committee members, Prof. David Benson, Prof. Jiun-Shyan Chen, Prof. Michael Holst and Prof. Alison Marsden for sharing their experience and knowledge with me throughout my research.

I am thankful to my colleges I had chance to work with at UCSD, Dr. Ming-Chen Hsu, Dr. Ido Akkerman, Dr. Xiaowei Deng, Jinhui Yan and Kenny Benner.

And finally I would like to express all my sincere appreciation to my lovely wife, Elina Karimullina, for her sincere love, support and encouregments for further achievements. I would have not been here without her. And with greatest respect and love I want to say "Thank you!" to my parents, Tatiana Korobenko and Alexander Korobenko, for believing in me, inspiring me and supporting me all the time.

Chapter 2, in part, is a reprint of the material as it appears in: "Aerodynamic simulation of vertical-axis wind turbines," (with M.-C. Hsu, I. Akkerman and Y. Bazilevs), *Journal of Applied Mechanics*, 2013 and "FSI Modeling of Vertical- Axis Wind Turbines," (with Y. Bazilevs, X. Deng, J. Yan, M. Kinzel and J.O. Dabiri), *Journal of Applied Mechanics*, 2014. The dissertation author was the primary investigator and author of this paper.

Chapter 3, in part, is a reprint of the material as it appears in: "Structural mechanics modeling and FSI simulation of wind turbines," (with M.-C. Hsu, I. Akkerman, J. Tippmann and Y. Bazilevs), *Mathematical Models and Methods in Applied Science*, 2013 and "Novel Structural Modeling and Mesh Moving Techniques for Advanced FSI Simulation of Wind Turbines," (with Y. Bazilevs, X. Deng and J. Yan), *International Journal for Numerical Methods in Engineering*, 2014. The dissertation author was the primary investigator and author of this paper.

Chapter 4, in part, is a reprint of the material as it appears in: "Structural me-

chanics modeling and FSI simulation of wind turbines," (with M.-C. Hsu, I. Akkerman, J. Tippmann and Y. Bazilevs), *Mathematical Models and Methods in Applied Science*, 2013 and "FSI Modeling of Vertical- Axis Wind Turbines," (with Y. Bazilevs, X. Deng, J. Yan, M. Kinzel and J.O. Dabiri), *Journal of Applied Mechanics*, 2014 and "Novel Structural Modeling and Mesh Moving Techniques for Advanced FSI Simulation of Wind Turbines," (with Y. Bazilevs, X. Deng and J. Yan), *International Journal for Numerical Methods in Engineering*, 2014. The dissertation author was the primary investigator and author of this paper.

## VITA

| | |
|---|---|
| 2008 | Bachelor of Science, National Aerospace University "Kharkov Aviation Institute" |
| 2011 | Master of Science, Clemson University |
| 2014 | Doctor of Philosophy, University of California, San Diego |

## PUBLICATIONS

"FSI Modeling of Vertical- Axis Wind Turbines," (with Y. Bazilevs, X. Deng, J. Yan, M. Kinzel and J.O. Dabiri), *Journal of Applied Mechanics*, 2014.

"Novel Structural Modeling and Mesh Moving Techniques for Advanced FSI Simulation of Wind Turbines," (with Y. Bazilevs, X. Deng and J. Yan), *International Journal for Numerical Methods in Engineering*, 2014.

"Aerodynamic simulation of vertical-axis wind turbines," (with M.-C. Hsu, I. Akkerman and Y. Bazilevs), *Journal of Applied Mechanics*, 2013.

"Structural mechanics modeling and FSI simulation of wind turbines," (with M.-C. Hsu, I. Akkerman, J. Tippmann and Y. Bazilevs), *Mathematical Models and Methods in Applied Science*, 2013. The dissertation author was the primary investigator and author of this paper.

ABSTRACT OF THE DISSERTATION

**Advanced Fluid–Structure Interaction Techniques in Application to Horizontal and Vertical Axis Wind Turbines**

by

Artem Korobenko

Doctor of Philosophy in Structural Engineering with a Specialization in Computational Scince

University of California, San Diego, 2014

Professor Yuri Bazilevs, Chair

During the last several decades engineers and scientists put significant effort into developing reliable and efficient wind turbines. As a wind power production demands grow, the wind energy research and development need to be enhanced with high-precision methods and tools. These include time-dependent, full-scale, complex-geometry advanced computational simulations at large-scale. Those, computational analysis of wind turbines, including fluid-structure interaction simulations (FSI) at full scale is important for accurate and reliable modeling, as well as blade failure prediction and design optimization.

In current dissertation the FSI framework is applied to most challenging class

of problems, such as large scale horizontal axis wind turbines and vertical axis wind turbines. The governing equations for aerodynamics and structural mechanics together with coupled formulation are explained in details. The simulations are performed for different wind turbine designs, operational conditions and validated against field-test and wind tunnel experimental data.

# Chapter 1

# Introduction

Starting as the technologies of the rural electrification program, the electricity-generating wind turbines has been developed to one of the biggest renewable energy power production facilities on the planet. Latest estimates from the International Renewable Energy Agency (IRENA) [7] shows that onshore wind is already at grid parity with fossil fuel electricity . According to latest reports of the Energy Information Administration of the U.S. Department of Energy [8] and annual energy report of the European Commission [9], the levelized cost of energy (LCOE) for the onshore wind falls within a range of $0.04 - $0.10 per kWh, making them extremely cost-competitive with conventional power sources as coal, integrated gasification combined cycle and nuclear energy ($0.06-$0.12 per kWh). Moreover, the wind energy is the fastest growing power production sector. To provide a comparison: during the period of 2000 to 2012, the installed capacity from nuclear power plants only increased by 9 GW, while the increase for wind power was 266 GW and around 100 GW for solar power plants [10]. Further, the wind turbines technologies have the largest remaining cost reduction potential [7] which can be achieved through advanced research and developments.

During the last several decades engineers and scientists put significant effort into developing reliable and efficient wind turbines. Since the 1970's most of the work focused on the development of horizontal-axis wind turbines (HAWTs). Vertical-axis wind turbines (VAWTs) were generally considered as a promising alternative to HAWTs. Before the mid-90's VAWTs were economically competitive with HAWTs for the same rated power. However, as the market demands for electric power grew, VAWTs were

found to be less efficient than HAWTs for large-scale power production. In recent years the offshore wind energy are getting increased attention. The total global installed capacity of offshore wind reached 4.1GW at the end of 2011 [7]. Far from the shore energy can be harvested from stronger and more sustained winds. Also, the noise generation and visual impact is no more a limitations in turbine designs. In the offshore environments large-size HAWTs are at the leading edge. They are equipped with complicated pitch and yaw control mechanisms to keep the turbine in operation for wind velocities of variable magnitude and direction, such as wind gusts. One of the most challenging offshore wind turbine designs is a floating wind turbine. Starting 2009, the practical feasibility and per-unit economics of deep-water, floating-turbine offshore wind was seen. The world's first floating full-scale offshore wind turbine has been lunched in the North Sea off the coast of Norway by Norwegian energy giant StatoilHydro in 2009. The turbine, known as Hywind, rests upon a floating stand that is anchored to the seabed by three cables. Water and rocks are placed inside the stand to provide ballast. The world's second full-scale floating wind turbine, named WindFloat, was designed by Principle Power and lunched in 2011 by the coast of Portugal. In 2013, as a part of US Department of Energy's Wind Program, the VolturnUS, first offshore wind turbine in Americas was powered up to provide electricity. Later, the same year, Japan switched on the first floating turbine at a wind farm 20 kilometeres off the coast of Fukushima. Up-to-date there are many projects on building the floating wind turbine farms in Asia, Europe and Americas. Moreover, wind-energy technologies are maturing, and several studies were recently initiated that involve placing VAWTs off shore, such as DeepWind project by Riso DTU National Laboratory for Sustainable Energy and other [11, 12].

As the problem remains for large-scale wind turbines, especially offshore, with grid connection and energy storage, the urban areas, closer to direct consumer become very attractive. Recently VAWTs resurfaced as a good source of small-scale electric power for urban areas. There are two main configurations of VAWTs, employing the Savonius or Darrieus rotor types [13]. The Darrieus configuration is a lift-driven turbine: The power is produced from the aerodynamic torque acting on the rotor. It is more efficient than the Savonius configuration, which is a drag-type design, where the power is generated using momentum transfer. The main advantage of VAWTs over the HAWTs

is their compact design. The generator and drive train components are located close to the ground, which allows for easier installation, maintenance and repair. Another advantage of VAWTs is that they are omidirectional (i.e., they don't have to be oriented into the main wind direction), which obviates the need to include expensive yaw control mechanisms in their design. However, this brings up issues related to self-starting. The ability of VAWTs to self-start depends on the wind conditions as well as on airfoil designs employed [14]. Studies in [15, 16] reported that a three-bladed H-type Darrieus rotor using a symmetric airfoil is able to self-start. In [17] the author showed that significant atmospheric wind transients are required to complete the self-starting process for a fixed-blade Darieus turbine when it is initially positioned in a dead-band region defined as the region with the tip-speed-ratio values that result in negative net energy produced per cycle. Self-starting remains an open issue for VAWTs, and an additional starting system is often required for successful operation.

As a wind power production demands grow, the wind energy research and development need to be enhanced with high-precision methods and tools. These include time-dependent, full-scale, complex-geometry advanced computational simulations at large-scale. Those, computational analysis of wind turbines, including fluid-structure interaction simulations at full scale is important for accurate and reliable modeling, as well as blade failure prediction and design optimization.

Due to increased recent emphasis on renewable energy, and, in particular, wind energy, aerodynamics modeling and simulation of HAWTs in 3D has become a popular research activity [5, 18–25]. FSI modeling of HAWTs is less developed. Accurate and robust full-machine wind-turbine FSI simulations engender several significant challenges when it comes to modeling of the aerodynamics. In the near-tip region of the offshore wind turbine blades the flow Reynolds number is $O(10^7)$, which results in fully-turbulent, wall-bounded flow. In order to accurately predict the blade aerodynamic loads in this regime, the numerical formulation must be stable and sufficiently accurate in the presence of thin, transitional turbulent boundary layers. Recently, several studies were reported showing validation at full-scale against field-test data for medium-size turbines [26], and demonstrating feasibility for application to larger-size offshore wind-turbine designs [18, 27, 28]. However, 3D aerodynamics and FSI modeling of

VAWTs is lagging behind. The majority of the computations for VAWTs are reported in 2D [29–31], while a recent 3D simulation in [32] employed a quasi-static representation of the air flow instead of solving the time-dependent problem.

The aerodynamics and FSI computational challenges in VAWTs are different than in HAWTs due to the differences in their aerodynamic and structural design. Because the rotation axis is orthogonal to the wind direction, the wind-turbine blades experience rapid and large variations in the angle of attack resulting in an air flow that is constantly switching from being fully attached to being fully separated, even under steady wind and rotor speeds. This, in turn, leads to high-frequency and high-amplitude variations in the aerodynamic torque acting on the rotor, requiring finer mesh resolution and smaller time-step size for accurate simulation [33]. VAWT blades are typically long and slender by design. The ratio of cord length to blade height is very low, requiring finer mesh resolution also in the blade height direction in order to avoid using high-aspect-ratio surface elements, and to better capture turbulent fluctuations in the boundary layer. High-fidelity modeling of the underlying aerodynamics requires a numerical formulation that properly accounts for this flow unsteadiness, and is valid for all flow regimes present. It is precisely this unsteady nature of the flow that creates significant challenges for the application of low-fidelity methods and tools (such as, for example, the FAST code [34]) to VAWTs. Another challenge is to represent how the turbulent flow features generated by the upstream blades affect the aerodynamics of the downstream blades [35]. The VAWT simulation complexity is further increased when several VAWTs are operating in close proximity to one another. Due to their compact design, VAWTs are often placed in arrays with spacing that is a little over one diameter between the turbine towers. In [1], this type placement was found beneficial for increased energy production.

When the FSI analysis of VAWTs is performed the simulation complexity is further increased. As can be seen in [36] the flexibility in VAWTs does not come from the blades, which are practically rigid (although blades deform at high rotational speeds), but rather from the tower itself, and its connection to the rotor and ground. As a result, the main FSI challenge is to be able to simulate a spinning rotor that is mounted on a flexible tower.

In order to account for addressed challenges, the FSI formulation should be robust, accurate and efficient for the targeted class of problems. The FSI framework used in current work was originally developed in [37, 38]. The aerodynamics formulation makes use of FEM-based moving-mesh ALE-VMS technique [37,39,40] combined with weakly-enforced essential boundary conditions [41–43]. The former acts as a turbulence model, while the latter relaxes the mesh size requirements in the boundary layer without sacrificing the solution accuracy. As shown in [44] this gives a good combination of accuracy and efficiency for this problem class. Having a well-designed boundary-layer mesh in wind-turbine simulations is critical for achieving engineering accuracy with a reasonable number of degrees of freedom. During operation, wind turbine blades undergo large global rotational motions, as well as local flapwise and edgewise bending, and axial torsion deformations. As a result, in order to account for the blade motion and to simultaneously maintain good-quality boundary-layer discretization, a moving-mesh technique should be employed where the boundary-layer mesh follows the blades as they moves through space. In the case of standalone wind-turbine-rotor FSI computations this may be accomplished by applying a global rotation to the entire aerodynamics mesh, and handling the remaining blade deflection using elastic mesh moving as in [18]. A jacobian-based stiffening technique in elastic mesh moving is essential for maintaining the integrity of the elements in the blade boundary layers [45–49].

In the case a full machine (i.e., tower, rotor, and nacelle) is considered, the spinning rotor interacts with the tower. This interaction is strong and needs to be modeled explicitly. In the recent wind-turbine FSI computations presented in [18, 26, 27, 50] the wind-turbine hub (or nacelle) was assumed to spin with a fixed, prescribed angular velocity, and the tower was assumed to be stationary. The aerodynamics of rotor-tower interaction was handled using a sliding-interface technique [24, 27, 33, 51]. In this technique, rather than rotating the entire computational domain, only the inner cylindrical subdomain that encloses the rotor undergoes a spinning motion inside the cylindrical cut-out of the outer stationary domain. The two domains do not overlap, and, as a result, create a sliding cylindrical interface with a priori nonmatching discretizations on each side. The continuity of the kinematic and traction variables across the nonmatching sliding interface is enforced weakly.

In order to simulate more complicated FSI scenarios, such as rotor yawing for HAWTs, or even basic operation for VAWTs, additional computational technology is required. In the case of HAWT rotor yawing motion, the entire gearbox undergoes rotation parallel to the tower axis, and this rotation must be transferred to the rotor and hub without interfering with the rotor spinning motion. In the case of basic VAWT operation, the air flow spins the rotor, which is connected to a flexible tower with struts. Furthermore, the moving-mesh aerodynamics formulation for this expanded problem class can no longer have a fixed sliding interface. For example, in the case of the rotor yawing motion, in order to keep the good quality of the aerodynamics mesh and prevent the rotor blades from crossing the boundary of the rotor cylindrical domain, it is preferred that the sliding interface follows the motion of the gearbox, while accommodating the spinning rotor. This results in two cylindrical surfaces moving together while one spins inside the other.

Another challenge in FSI simulations is to model the geometrically complex structures with its nonlinear material distribution, which undergoes large deformation. A combination of a rotation-free multilayer composite Kirchhoff–Love shell [18, 52, 53] and beam [54] allows for the rotor to spin freely and for the tower and blades to undergo elastic deformations. An isogeometric analysis (IGA) [55, 56] with NURBS-based (nonuniform rational B-splines) [57] elements representation is used to construct analysis-suitable geometry. The NURBS-based IGA may be seen as a combination of CAD basis functions and the isoparametric concept and may be extended to T-splines and subdivision surfaces. Because of the rational nature of the basis functions the circular shapes can be represented exactly which reduce the geometrical-approximation error when modeling complex-shaped wind turbine blades. Furthermore, the higher-order continuity is achieved with NURBS basis functions and the geometry is preserved unchanged under the mesh refinement process, which is not the case in FEM.

The dissertation is outlined as follows. In Chapter 2 we state the ALE-VMS formulation of aerodynamics in combination with our sliding interface approach for the simulation of mechanical components in relative motion. To validate our aerodynamic formulation we show the computations of a small-scale Darrieus-type wind turbines. One is a 3.5 kW wind turbine tested in NRC wind tunnel [32, 58]. For this turbine

two cases were simulated: A single turbine, and two counter-rotating turbines placed side-by-side in close proximity to one another. For a single turbine a mesh refinement study was performed, and results were compared to experimental data. Another turbine is designed by Windspire with rated power of 1.2 kW [36]. For this case the computational results were compared to a field test experiments conducted by the National Renewable Energy Lab (NREL) [3] and Caltech Field Laboratory for Optimized Wind Energy (FLOWE) [1, 2]. In Chapter 3 we present the coupled Kirchhoff–Love shell for an arbitrary composite layup of wind turbine blades. To verify the model we perform the eigenfrequency analysis of recently designed offshore wind turbine blade and CX-100 blade, which compare favorably to the experimental data. In Chapter 4 we introduce the coupled FSI formulation employed in this work with non matching discretization of the aerodynamic and structural domains. Later in the chapter we present FSI computations of the Micon 65/13M wind turbine. Both the aerodynamics and FSI torque results fall within the range predicted by the field tests for this wind turbine. The FSI case shows high-frequency fluctuations in the aerodynamic torque, which are due to the high-frequency vibration of the blades. Next, the FSI computations of offshore HAWT under yawing motion is presented and the discretization techniques employed and the aforementioned enhancement of the sliding-interface formulation are described. We conclude with the FSI computations of the Windspire VAWT and discuss start-up issues. In Chapter 5 we draw conclusions and discuss possible future research directions.

# Chapter 2

# Methods for Modeling and Simulation of Wind Turbine Aerodynamics

## 2.1 Aerodynamics formulation

The wind turbine aerodynamics is governed by the Navier–Stokes equations of incompressible flows. The incompressible-flow assumption is valid for our application due to low values of the Mach number (less than 0.3). The Navier–Stokes equations is written in the Arbitrary Lagrangian–Eulerian (ALE) frame [39] to accommodate the moving aerodynamics domain (or the part of domain that encloses a spinning rotor). At a continuous level the problem may be written as follows:

$$\rho_1 \left( \left. \frac{\partial \mathbf{u}_1}{\partial t} \right|_{\hat{x}} + (\mathbf{u}_1 - \hat{\mathbf{u}}) \cdot \boldsymbol{\nabla} \mathbf{u}_1 - \mathbf{f}_1 \right) - \boldsymbol{\nabla} \cdot \boldsymbol{\sigma}_1 = \mathbf{0}, \tag{2.1}$$

$$\boldsymbol{\nabla} \cdot \mathbf{u}_1 = 0, \tag{2.2}$$

where $\rho_1$ is the density, $\mathbf{f}_1$ is the external force per unit mass, $\mathbf{u}_1$ and $\hat{\mathbf{u}}$ are velocities of the fluid and fluid domain, respectively. The stress tensor $\boldsymbol{\sigma}_1$ is defined as

$$\boldsymbol{\sigma}_1 (\mathbf{u}_1, p) = -p\mathbf{I} + 2\mu \boldsymbol{\varepsilon} (\mathbf{u}_1), \tag{2.3}$$

where $p$ is the pressure, $\mathbf{I}$ is the identity tensor, $\mu$ is the dynamic viscosity, and $\boldsymbol{\varepsilon} (\mathbf{u}_1)$ is the strain-rate tensor given by

$$\boldsymbol{\varepsilon} (\mathbf{u}_1) = \frac{1}{2} \left( \boldsymbol{\nabla} \mathbf{u}_1 + \boldsymbol{\nabla} \mathbf{u}_1^T \right). \tag{2.4}$$

In Eq. (2.1), $\left|_{\hat{x}}\right.$ denotes the time derivative taken with respect to a fixed referential domain spatial coordinates $\hat{\mathbf{x}}$. The spatial derivatives in the above equations are taken with respect to the spatial coordinates $\mathbf{x}$ of the current configuration.

The semi-discrete formulation of a Navier–Stokes equation is obtained using the arbitrary Lagrangian–Eulerian variational multi-scale (ALE-VMS) formulation of aerodynamics, which is a moving-domain extension of the residual-based variational multiscale (RBVMS) formulation proposed in [59] in the context of nonmoving domain problems. The ALE-VMS formulation acts as a turbulence model and relies on a-priori scale separation, where the coarse scale are identified with numerical approximation and fine-sale solutions for velocity and pressure are assumed to be proportional to the residuals of the large-scale equations. In contrast to the classical Large-Eddy Simulation (LES) turbulence model the ALE-VMS formulation do not introduce any ad hoc viscosity terms.

The ALE–VMS formulation of aerodynamics is given by: find $\mathbf{u}_1^h \in \mathcal{S}_u^h$ and $p^h \in \mathcal{S}_p^h$, such that, $\forall \mathbf{w}_1^h \in \mathcal{V}_u^h$ and $\forall q^h \in \mathcal{V}_p^h$,

$$
\begin{aligned}
&\int_{(\Omega_t)_1} \mathbf{w}_1^h \cdot \rho_1 \left( \left.\frac{\partial \mathbf{u}_1^h}{\partial t}\right|_{\hat{x}} + \left(\mathbf{u}_1^h - \hat{\mathbf{u}}^h\right) \cdot \boldsymbol{\nabla} \mathbf{u}_1^h - \mathbf{f}_1^h \right) \mathrm{d}\Omega \\
&+ \int_{(\Omega_t)_1} \boldsymbol{\varepsilon}\left(\mathbf{w}_1^h\right) : \boldsymbol{\sigma}_1\left(\mathbf{u}_1^h, p^h\right) \mathrm{d}\Omega - \int_{(\Gamma_t)_{1h}} \mathbf{w}_1^h \cdot \mathbf{h}_1^h \, \mathrm{d}\Gamma + \int_{(\Omega_t)_1} q^h \boldsymbol{\nabla} \cdot \mathbf{u}_1^h \, \mathrm{d}\Omega \\
&+ \sum_{e=1}^{N_{\mathrm{el}}} \int_{\left(\Omega_t^e\right)_1} \tau_{\mathrm{M}} \left( \left(\mathbf{u}_1^h - \hat{\mathbf{u}}^h\right) \cdot \boldsymbol{\nabla} \mathbf{w}_1^h + \frac{\boldsymbol{\nabla} q^h}{\rho_1} \right) \cdot \mathbf{r}_{\mathrm{M}}\left(\mathbf{u}_1^h, p^h\right) \mathrm{d}\Omega \\
&+ \sum_{e=1}^{N_{\mathrm{el}}} \int_{\left(\Omega_t^e\right)_1} \rho_1 \tau_{\mathrm{C}} \boldsymbol{\nabla} \cdot \mathbf{w}_1^h r_{\mathrm{C}}\left(\mathbf{u}_1^h, p^h\right) \mathrm{d}\Omega \\
&- \sum_{e=1}^{N_{\mathrm{el}}} \int_{\left(\Omega_t^e\right)_1} \tau_{\mathrm{M}} \mathbf{w}_1^h \cdot \left( \mathbf{r}_{\mathrm{M}}\left(\mathbf{u}_1^h, p^h\right) \cdot \boldsymbol{\nabla} \mathbf{u}_1^h \right) \mathrm{d}\Omega \\
&- \sum_{e=1}^{N_{\mathrm{el}}} \int_{\left(\Omega_t^e\right)_1} \frac{\boldsymbol{\nabla} \mathbf{w}_1^h}{\rho_1} : \left(\tau_{\mathrm{M}} \mathbf{r}_{\mathrm{M}}\left(\mathbf{u}_1^h, p^h\right)\right) \otimes \left(\tau_{\mathrm{M}} \mathbf{r}_{\mathrm{M}}\left(\mathbf{u}_1^h, p^h\right)\right) \mathrm{d}\Omega = \mathbf{0}, \qquad (2.5)
\end{aligned}
$$

Here the spatial domain $(\Omega_t)_1$ of aerodynamic problem with boundary $(\Gamma_t)_1$ at time $t \in (0, T)$ is divided into $N_{\mathrm{el}}$ individual spatial finite element subdomains denoted by $(\Omega_t^e)_1$. The subscript $t$ indicates the time-dependancy of the spatial domain and the boundary.

The finite-dimensional trial function spaces $\mathcal{S}_u^h$ for the velocity and $\mathcal{S}_p^h$ for the pressure, as well as the corresponding test function spaces $\mathcal{V}_u^h$ and $\mathcal{V}_p^h$ are assumed to be of equal order. Although in this work these are comprised of piece-wise linear FEM functions and assumed to be of equal order, the formulation is well suited for discretization using higher-order FEM and IGA (see, e.g., [60, 61]). In Eq. (2.5), $\mathbf{h}_1$ is the natural boundary condition, $(\Gamma_t)_{1\mathrm{h}}$ is the part of the boundary where we specify that natural boundary condition, $\hat{\mathbf{u}}^h$ is the mesh velocity, and $\mathbf{r}_\mathrm{M}$ and $r_\mathrm{C}$ are the residuals of the momentum and continuity (incompressibility constraint) equations, respectively, given by

$$\mathbf{r}_\mathrm{M}(\mathbf{u}_1^h, p^h) = \rho_1 \left( \left.\frac{\partial \mathbf{u}_1^h}{\partial t}\right|_{\hat{\mathbf{x}}} + \left(\mathbf{u}_1^h - \hat{\mathbf{u}}^h\right) \cdot \boldsymbol{\nabla} \mathbf{u}_1^h - \mathbf{f}_1^h \right) - \boldsymbol{\nabla} \cdot \boldsymbol{\sigma}_1 \left(\mathbf{u}_1^h, p^h\right), \tag{2.6}$$

and

$$r_\mathrm{C}(\mathbf{u}_1^h, p^h) = \boldsymbol{\nabla} \cdot \mathbf{u}_1^h. \tag{2.7}$$

Also in Eq. (2.5), $\tau_\mathrm{M}$ and $\tau_\mathrm{C}$ are the stabilization parameters [41–44, 49, 59, 62–72], defined as

$$\tau_\mathrm{M} = \left( \frac{4}{\Delta t^2} + \left(\mathbf{u}_1^h - \hat{\mathbf{u}}^h\right) \cdot \mathbf{G} \left(\mathbf{u}_1^h - \hat{\mathbf{u}}^h\right) + C_I \nu^2 \mathbf{G} : \mathbf{G} \right)^{-1/2} \tag{2.8}$$

and

$$\tau_\mathrm{C} = \left(\mathrm{tr}\mathbf{G}\ \tau_\mathrm{M}\right)^{-1}, \tag{2.9}$$

where

$$\mathrm{tr}\mathbf{G} = \sum_{i=1}^{d} G_{ii} \tag{2.10}$$

is the trace of the element metric tensor $\mathbf{G}$, $\Delta t$ is the time-step size, and $C_I$ is a positive constant, independent of the mesh size, derived from an appropriate element-wise inverse estimate (see, e.g., [73–75]).

The ALE-VMS formulation is augmented with weakly enforced essential boundary conditions, which were introduced in [41] to improve the performance in the presence of unresolved boundary layers [42, 43, 71]. To account for the weak enforcement of the essential boundary condition they are removed from trial and test function sets $\mathcal{S}_u^h$

and $\mathcal{V}_u^h$ and the following terms are added to the left-hand side of Eq. (2.5):

$$
\begin{aligned}
&- \sum_{b=1}^{N_{\text{eb}}} \int_{\Gamma_t^b \bigcap (\Gamma_t)_g} \mathbf{w}_1^h \cdot \boldsymbol{\sigma}_1 \left(\mathbf{u}_1^h, p^h\right) \mathbf{n}_1 \, \mathrm{d}\Gamma \\
&- \sum_{b=1}^{N_{\text{eb}}} \int_{\Gamma_t^b \bigcap (\Gamma_t)_g} \left(2\mu \boldsymbol{\varepsilon}\left(\mathbf{w}_1^h\right) \mathbf{n}_1 + q^h \mathbf{n}_1\right) \cdot \left(\mathbf{u}_1^h - \mathbf{g}^{\mathbf{h}}\right) \mathrm{d}\Gamma \\
&- \sum_{b=1}^{N_{\text{eb}}} \int_{\Gamma_t^b \bigcap (\Gamma_t)_g^-} \mathbf{w}_1^h \cdot \rho_1 \left(\left(\mathbf{u}_1^h - \hat{\mathbf{u}}^h\right) \cdot \mathbf{n}_1\right) \left(\mathbf{u}_1^h - \mathbf{g}^{\mathbf{h}}\right) \mathrm{d}\Gamma \\
&+ \sum_{b=1}^{N_{\text{eb}}} \int_{\Gamma_t^b \bigcap (\Gamma_t)_g} \tau_{\text{B}} \mathbf{w}_1^h \cdot \left(\mathbf{u}_1^h - \mathbf{g}^{\mathbf{h}}\right) \mathrm{d}\Gamma,
\end{aligned}
\tag{2.11}
$$

Here the part of the boundary $(\Gamma_t)_g$ with prescribed velocity $\mathbf{g}^{\mathbf{h}}$ is decomposed into $N_{\text{eb}}$ surface elements denoted by $\Gamma_t^b$, and $(\Gamma_t)_g^-$ is defined as the "inflow" part of $(\Gamma_t)_g$:

$$
(\Gamma_t)_g^- = \left\{ \mathbf{x} \;\middle|\; \left(\mathbf{u}_1^h - \hat{\mathbf{u}}^h\right) \cdot \mathbf{n}_1 < 0, \; \forall \mathbf{x} \subset (\Gamma_t)_g \right\}, \tag{2.12}
$$

where $\mathbf{n}_1$ is the outward wall-normal unit vector. In Eq. (2.11) the term in the first line is the so-called consistency term. It is necessary to ensure that the discrete formulation is identically satisfied by the exact solution of the Navier–Stokes equations, which, in turn, has implications on the accuracy of the discrete formulation. Also note that this term cancels with the contributions coming from the integration-by-parts of the stress terms in Eq. (2.5), thus correctly removing traction boundary conditions from the no-slip boundary. The term in the second line is the so-called adjoint consistency term. Its role is less intuitive, as it ensures that the analytical solution of the adjoint equations, when introduced in place of the linear momentum and continuity equation test functions, also satisfies the discrete formulation. Adjoint consistency is linked to optimal convergence of the discrete solution in lower-order norms (see, e.g., [76]). The term in the third line leads to better satisfaction of the inflow boundary conditions. The last term are penalty-like, in that it penalize the deviation of the discrete solution from its prescribed value at the boundary. These term are necessary to ensure the stability of the discrete formulation, when introducing the consistency and adjoint consistency terms. The stabilization parameter $\tau_{\text{B}}$ is defined as

$$
\tau_{\text{B}} = \frac{C_I^B \mu}{h_n}, \tag{2.13}
$$

where $h_n$ is the wall-normal element size, and $C_I^B$ is a sufficiently large positive constant computed from an appropriate element-level inverse estimate (see, e.g., [73–75]).

## 2.2 Sliding interface formulation for objects in relative motion

To perform the full wind turbine simulation and capture the rotor-tower interaction the fluid domain is divided into two parts as shown in Figure 2.1. The moving subdomain containing the rotor is in motion while the stationary subdomain encloses the rest of the wind turbine. Because of the relative motion between the subdomains, the shared sliding cylindrical interface has nonmatching meshes on each side (see Figure 2.2). The compatibility conditions enforced at the sliding interface are:

$$\mathbf{u}_{1\mathrm{M}} - \mathbf{u}_{1\mathrm{S}} = \mathbf{0}, \tag{2.14}$$

$$\left(-p_{\mathrm{S}}\mathbf{I} + 2\mu\boldsymbol{\varepsilon}\left(\mathbf{u}_{1\mathrm{S}}\right)\right)\mathbf{n}_{\mathrm{S}} + \left(-p_{\mathrm{M}}\mathbf{I} + 2\mu\boldsymbol{\varepsilon}\left(\mathbf{u}_{1\mathrm{M}}\right)\right)\mathbf{n}_{\mathrm{M}} = \mathbf{0}, \tag{2.15}$$

where all quantities with subscripts "$S$" and "$M$" refer to the stationary and moving subdomains, respectively (see Figure 2.1), and $\mathbf{n}_{\mathrm{S}}$ and $\mathbf{n}_{\mathrm{M}}$ are the unit outward normal vectors. In the case of multiple wind turbines, each rotor is enclosed by its spinning cylindrical subdomain, and multiple sliding interfaces are present in the computation where the compatibility conditions given by Eqs. (2.14) and (2.15) are enforced.

To ensure proper coupling at the sliding interface additional numerical procedures is required. A method that is based on the weak enforcement of the kinematic and traction compatibility conditions at the sliding interface was first proposed in [51] in the context of flows about rotating components using NURBS-based IGA. The advantage of IGA for rotating-component flows is that the cylindrical sliding interfaces are represented exactly, and no geometry errors are incurred. In the case of standard FEM employed here, the geometric compatibility is only approximate.

The semi-discrete ALE-VMS formulation that weakly imposes continuity of the fluid velocity and traction vectors at the sliding interface is stated as: find $\{\mathbf{u}_{1\mathrm{S}}^h, p_{\mathrm{S}}^h\}$ and

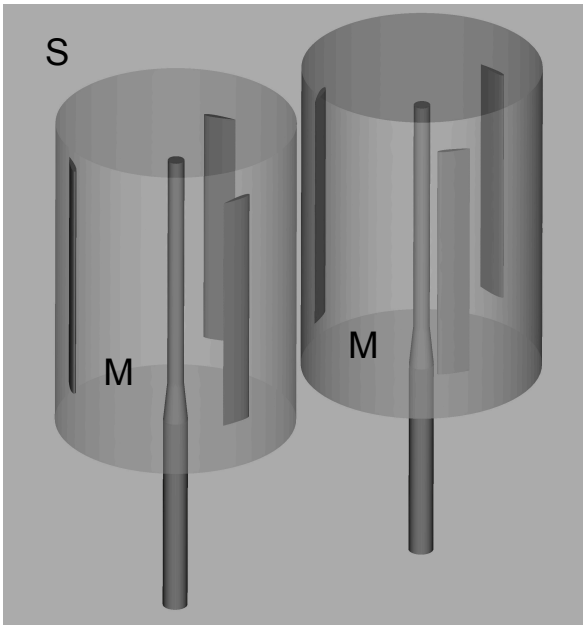


**Figure 2.1**: Computational domain for the two-VAWT case: Zoom on the rotating subdomains. The two cylindrical subdomains (labeled "$M$") spin with the rotors, while the remaining subdomain (labeled "$S$") is stationary.

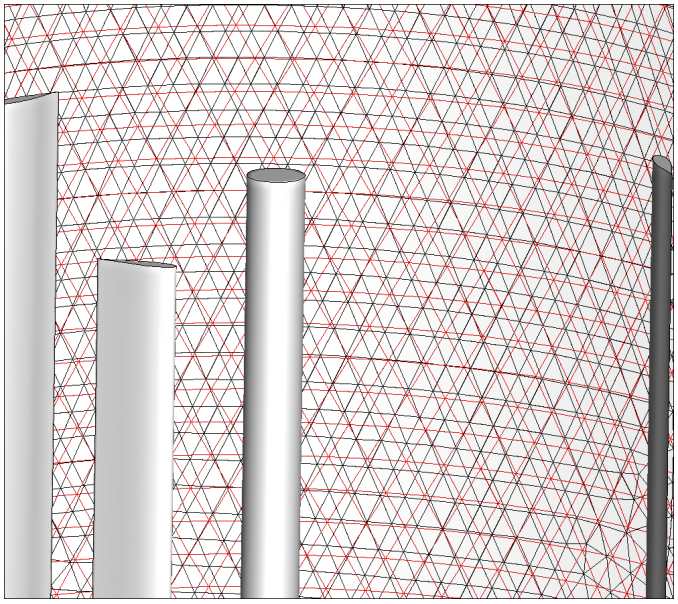

**Figure 2.2**: Nonmatching meshes at the sliding interface between the stationary and moving subdomains.

$\{\mathbf{u}^h_{1\mathrm{M}}, p^h_{\mathrm{M}}\}$, such that $\forall\{\mathbf{w}^h_{1\mathrm{S}}, q^h_{\mathrm{S}}\}$ and $\forall\{\mathbf{w}^h_{1\mathrm{M}}, q^h_{\mathrm{M}}\}$,

$$
\begin{aligned}
&B_{1\mathrm{S}}(\{\mathbf{w}^h_{1\mathrm{S}}, q^h_{\mathrm{S}}\}, \{\mathbf{u}^h_{1\mathrm{S}}, p^h_{\mathrm{S}}\}; \hat{\mathbf{u}}^h_{\mathrm{S}}) - F_{1\mathrm{S}}(\{\mathbf{w}^h_{1\mathrm{S}}, q^h_{\mathrm{S}}\}) \\
&+ B_{1\mathrm{M}}(\{\mathbf{w}^h_{1\mathrm{M}}, q^h_{\mathrm{M}}\}, \{\mathbf{u}^h_{1\mathrm{M}}, p^h_{\mathrm{M}}\}; \hat{\mathbf{u}}^h_{\mathrm{M}}) - F_{1\mathrm{M}}(\{\mathbf{w}^h_{1\mathrm{M}}, q^h_{\mathrm{M}}\}) \\
&- \sum_{b=1}^{N_{\mathrm{eb}}} \int_{\Gamma^b_t \bigcap (\Gamma_t)_{\mathrm{SI}}} \left(\mathbf{w}^h_{1\mathrm{S}} - \mathbf{w}^h_{1\mathrm{M}}\right) \cdot \frac{1}{2} \left(\boldsymbol{\sigma}_{1\mathrm{S}} \mathbf{n}_{1\mathrm{S}} - \boldsymbol{\sigma}_{1\mathrm{M}} \mathbf{n}_{1\mathrm{M}}\right) \mathrm{d}\Gamma \\
&- \sum_{b=1}^{N_{\mathrm{eb}}} \int_{\Gamma^b_t \bigcap (\Gamma_t)_{\mathrm{SI}}} \frac{1}{2} \left(\delta\boldsymbol{\sigma}_{1\mathrm{S}} \mathbf{n}_{1\mathrm{S}} - \delta\boldsymbol{\sigma}_{1\mathrm{M}} \mathbf{n}_{1\mathrm{M}}\right) \cdot \left(\mathbf{u}^h_{1\mathrm{S}} - \mathbf{u}^h_{1\mathrm{M}}\right) \mathrm{d}\Gamma \\
&- \sum_{b=1}^{N_{\mathrm{eb}}} \int_{\Gamma^b_t \bigcap (\Gamma_t)_{\mathrm{SI}}} \mathbf{w}^h_{1\mathrm{S}} \cdot \rho \left\{\left(\mathbf{u}^h_{1\mathrm{S}} - \hat{\mathbf{u}}^h_{\mathrm{S}}\right) \cdot \mathbf{n}_{1\mathrm{S}}\right\}_- \left(\mathbf{u}^h_{1\mathrm{S}} - \mathbf{u}^h_{1\mathrm{M}}\right) \mathrm{d}\Gamma \\
&- \sum_{b=1}^{N_{\mathrm{eb}}} \int_{\Gamma^b_t \bigcap (\Gamma_t)_{\mathrm{SI}}} \mathbf{w}^h_{1\mathrm{M}} \cdot \rho \left\{\left(\mathbf{u}^h_{1\mathrm{M}} - \hat{\mathbf{u}}^h_{\mathrm{M}}\right) \cdot \mathbf{n}_{1\mathrm{M}}\right\}_- \left(\mathbf{u}^h_{1\mathrm{M}} - \mathbf{u}^h_{1\mathrm{S}}\right) \mathrm{d}\Gamma \\
&+ \sum_{b=1}^{N_{\mathrm{eb}}} \int_{\Gamma^b_t \bigcap (\Gamma_t)_{\mathrm{SI}}} \tau_{\mathrm{B}} \left(\mathbf{w}^h_{1\mathrm{S}} - \mathbf{w}^h_{1\mathrm{M}}\right) \cdot \left(\mathbf{u}^h_{1\mathrm{S}} - \mathbf{u}^h_{1\mathrm{M}}\right) \mathrm{d}\Gamma = 0,
\end{aligned}
\tag{2.16}
$$

where

$$
\delta\boldsymbol{\sigma}_1 \left(\mathbf{w}^h_1, q^h\right) = q^h \mathbf{I} + 2\mu\boldsymbol{\varepsilon}\left(\mathbf{w}^h_1\right). \tag{2.17}
$$

The terms on the first line of Eq. (2.16) correspond to the ALE–VMS formulation with weak boundary conditions in the stationary and rotating subdomains given by Eqs. (2.5) and (2.11). The rest of the terms in Eq. (2.16) are associated with weak enforcement of the kinematic and traction compatibility at the sliding interface $(\Gamma_t)_{\mathrm{SI}}$. The structure of these terms is similar to those in Eq. (2.11). The significance of each term is explained in detail in [51]. In the above formulations, $\{\mathcal{A}\}_-$ denotes the negative part of $\mathcal{A}$, that is, $\{\mathcal{A}\}_- = \mathcal{A}$ if $\mathcal{A} < 0$ and $\{\mathcal{A}\}_- = 0$ if $\mathcal{A} \geq 0$. The formulation may be see as a Discontinuous Galerkin method (see, e.g., Arnold *et al.* [76]), where the continuity of the basis function is enforced everywhere in the interior of the two subdomains, but not at the sliding interface between them. Note that, in this case, $\hat{\mathbf{u}}^h_{\mathrm{S}} = \mathbf{0}$, because the domain is stationary. However, the formulation is able to handle situations where both subdomains are in motion.

**Remark** We note that rotation is handled with the ALE technique rather than using the

Navier–Stokes equations written in the rotating reference frame. We favor using ALE (or other moving-domain techniques, such as space–time methods [21, 22, 77, 78]) for this class of problems because it naturally leads to a kinematically consistent treatment of rotor-stator interaction.

## 2.3 Aerodynamics simulations of vertical axis wind turbines with Darrieus H-type rotor

### 2.3.1 Validation study using wind tunnel experiment

The aerodynamics simulations are performed for a three-blade, high-solidity VAWT with the rated power of 3.5 kW. The prototype is a Darrieus H-type turbine designed by Cleanfield Energy Corporation. Full-scale tests for this turbine were conducted in the National Research Council (NRC) low-speed wind tunnel at McMaster University (see Figure 2.3). Experimental studies for this turbine focused on the application of VAWTs in urban areas [58].

The turbine has a tower height of 7 m. The blades, 3 m in height, are connected to the tower by the struts of length 1.25 m. This value is taken as the rotor radius. A symmetric NACA0015 airfoil profile with chord length of 0.4 m is employed along the entire length of the blades. See Figure 2.1 for an illustration.

The computations were carried out for constant inflow wind speed of 10 m/s, and constant, fixed rotor speed of 115 rpm. This set up corresponds to the tip speed ration of 1.5, which gave maximum rotor power as reported in [32, 58]. However, it was also reported for the wind tunnel tests that the control mechanism employed was able to maintain an *average* rotor speed of 115 rpm with the deviation of ±2.5 rpm. This means the actual rotor speed was never constant.

The air density and viscosity are set to 1.23 kg/m$^3$ and $1.78 \times 10^{-5}$ kg/(m·s), respectively. On the inflow, the wind speed of 10 m/s is prescribed. On the top, bottom and side surfaces of the stationary domain no-penetration boundary conditions are prescribed, while zero traction boundary condition is set on the outflow. No-slip boundary conditions are imposed weakly on the rotor blades and tower. The struts are not modeled

**Figure 2.3**: Full-scale prototype of VAWT with Darrieus H-type rotor in NRC low-speed wind tunnel at McMaster University.

in this work to reduce computational cost. The struts are not expected to significantly influence the results for this VAWT design.

The computations were carried out in a parallel computing environment. The meshes, which consist of linear triangular prisms in the boundary layers and linear tetrahedra elsewhere, are partitioned into subdomains using METIS [79], and each subdomain is assigned to a compute core. The parallel implementation of the methodology may be found in [80]. The time step is set to $1.0 \times 10^{-5}$ s for all cases.

**Single turbine simulation**

We first compute a single VAWT and assess the resolution demands for this class of problems. The stationary domain has the outer dimensions of 50 m, 20 m, and 30 m in the stream-wise, vertical, and span-wise directions, respectively. The VAWT centerline is located 15 m from the inflow and side boundaries. The radius and height of the spinning cylinder are both 4 m.

Three meshes are used with increasing levels of refinement. The overall mesh statistics are summarized in Table 2.1. The finest mesh has over 17M elements. The details of the boundary-layer discretization are as follows. For Mesh 1, the size of the first element in the wall-normal direction is 0.000667 m, and 15 layers of prismatic elements were generated with a growth ratio of 1.15. For Mesh 2, the size of the first element in the wall-normal direction is 0.000470 m, and 21 layers of prismatic elements were generated with a growth ratio of 1.1. For Mesh 3, the size of the first element in the wall-normal direction is 0.000333 m, and 30 layers of prismatic elements were generated with a growth ratio of 1.05. Figure 2.14 shows a 2D slice of Mesh 2, focusing on the boundary-layer discretization of the blade.

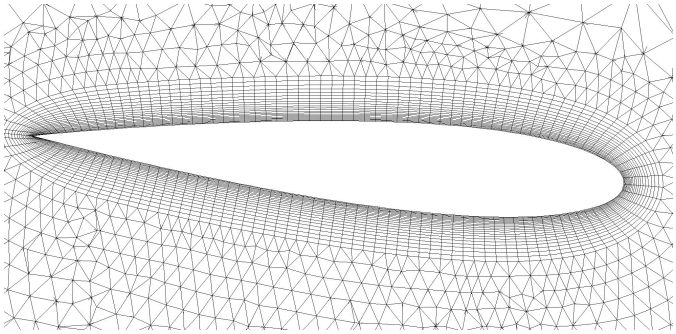

**Figure 2.4**: 2D slice of Mesh 2, focusing on the blade boundary-layer discretization.

**Table 2.1**: Statistics of the FEM meshes of the VAWT.

| | Number of Nodes | Number of Elements |
|---|---|---|
| Mesh 1 | 1,143,609 | 4,064,358 |
| Mesh 2 | 2,478,993 | 7,324,964 |
| Mesh 3 | 6,401,238 | 17,434,372 |

Time history of the computed aerodynamic torque is plotted in Figure 2.5 together with the experimental value reported for these operating conditions. Only the mean value of the torque was reported in [32, 58]. Note that after a couple of cycles a nearly periodic solution is attained. Mesh 1 predicts the average torque of about 52 Nm, Mesh 2 gives the average torque of about 70 Nm, and Mesh 3 predicts the average torque of about 80 Nm, while the targeted experimental value is about 90 Nm. Looking further at the curves we observe that the largest differences between the predicted values of the torque between the meshes occur at the maxima and minima of the curves. Also note that the torque fluctuation during the cycle is nearly 200 Nm, which is over twice the average. One way to mitigate such high torque variations is to allow variable rotor speed.

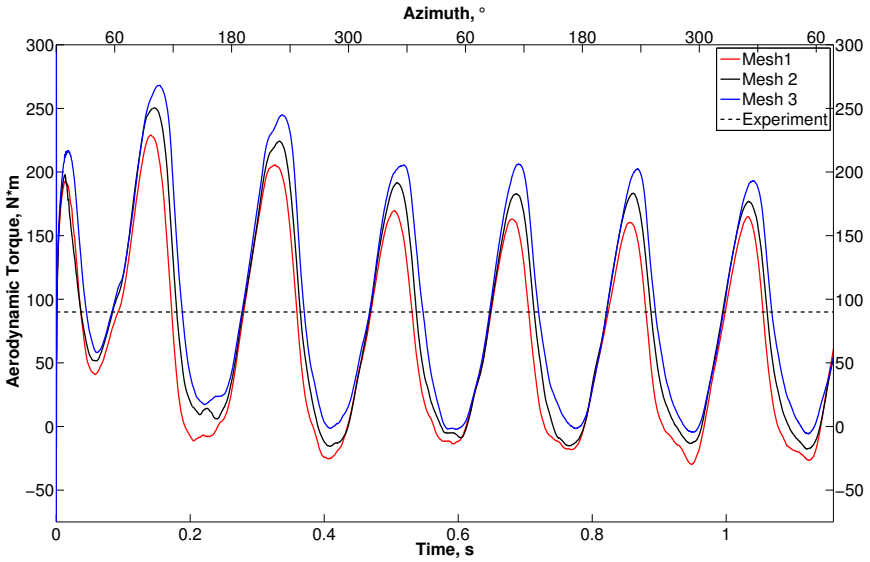


**Figure 2.5**: Time history of the aerodynamic torque for the three meshes used. The experimental result is plotted for comparison.

Figure 2.6 shows a snapshot of vorticity colored by flow speed. The upstream blade generates tip vortices near its top and bottom sections. Note that no large vortices are present in the middle section of the blade. There, as the flow separates on the airfoil surface, larger vortices immediately break up into fine-grained trailing-edge turbulence. The tip vortex and trailing-edge turbulence are then convected with the ambient wind

velocity, and impact the tower, as well as the blade that happens to be in the downwind position in the spin cycle. However, as it is evident from the torque time histories shown in Figure 2.5, these do not produce a major impact on the rotor loads, at least for a chosen set of wind and rotor speeds. The situation may, of course, change for a different set of operating conditions.

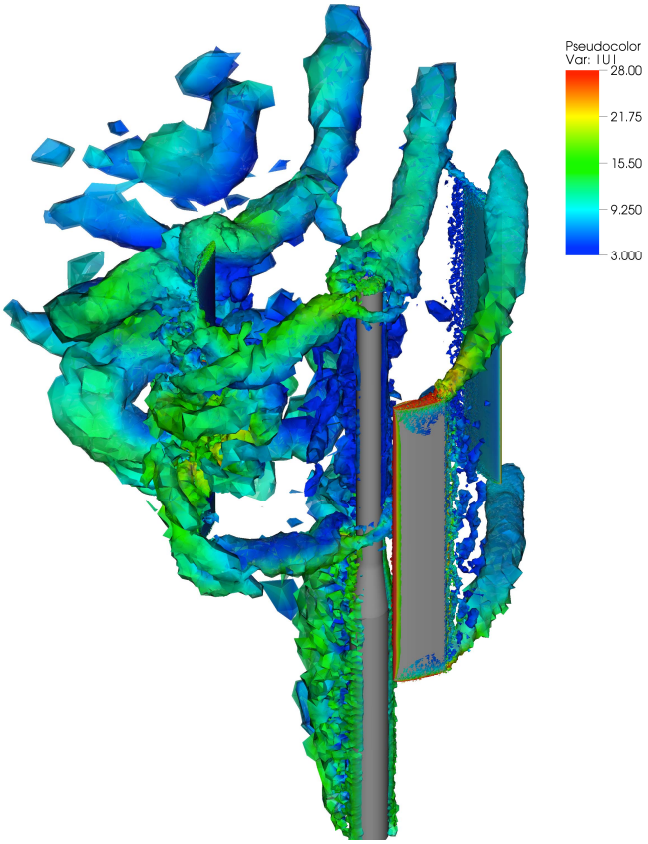


**Figure 2.6**: Vorticity isosurfaces at a time instant colored by velocity magnitude.

### Multiple turbine simulation

Here we investigate two counter-rotating turbines placed side-by-side in close proximity to one another. The wind and rotor speeds are the same as before, however, the turbines rotate out of phase, with the difference of 60°. The distance between the towers of the two turbines is $2.64R$, where $R$ =1.25 m is the rotor radius. This distance between the turbines falls in the range investigated in the experimental work of [1].

The stationary domain has the outer dimensions of 50 m, 20 m, and 33.3 m in the stream-wise, vertical, and span-wise directions, respectively. The centerline of each VAWT is located 15 m from the inflow and 15 m from its closest side boundary. The radius and height of the spinning cylinders are 1.45 m and 4 m, respectively.

A 2D slice of the computational-domain mesh focusing on the two rotors is shown in Figure 2.7. The boundary layer discretization employed for this computation is the same as that of Mesh 2 in the previous section.

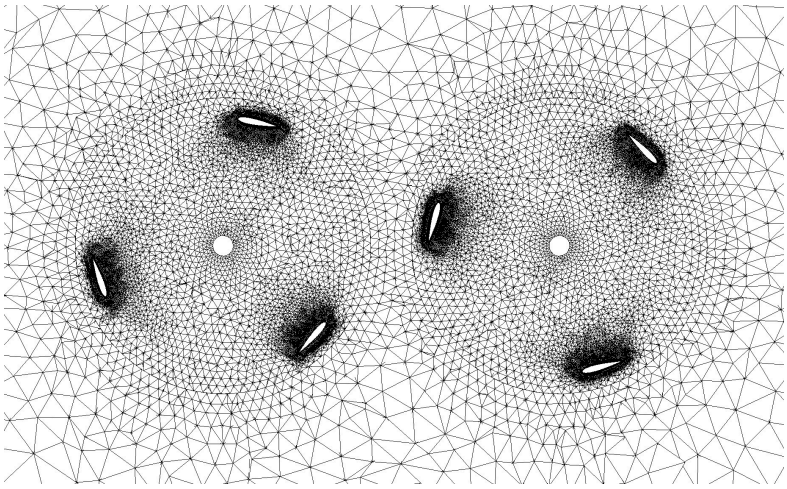

**Figure 2.7**: Cross-section of the mesh for the two-VAWTs rotating counterclockwise.

Figure 2.8 shows the time history of the aerodynamic torque for the two-turbine case. The curve corresponding to the second turbine is shifted by 60° such that both curves are in phase. The time history of the torque for a single VAWT simulation is shown for comparison. Note that while the maxima of all curves are virtually coincident, the minima are lower for the case of multiple turbines. Also note that the multiple-turbine torque curves exhibit some fluctuation near their minima, while the single-turbine torque curve is smooth near its minima. This is likely due to the fact that the blade from one turbine, as it approaches the plane defined by the centerlines of the two towers, encounters the wake of the blade from another turbine. This, in turn, produces higher drag on that blade and results in reduction of the aerodynamic torque. A snapshot of vorticity colored by flow speed depicted in Figure 2.9 shows that the short distance between the turbines has a noticeable effect on the resulting aerodynamics. This

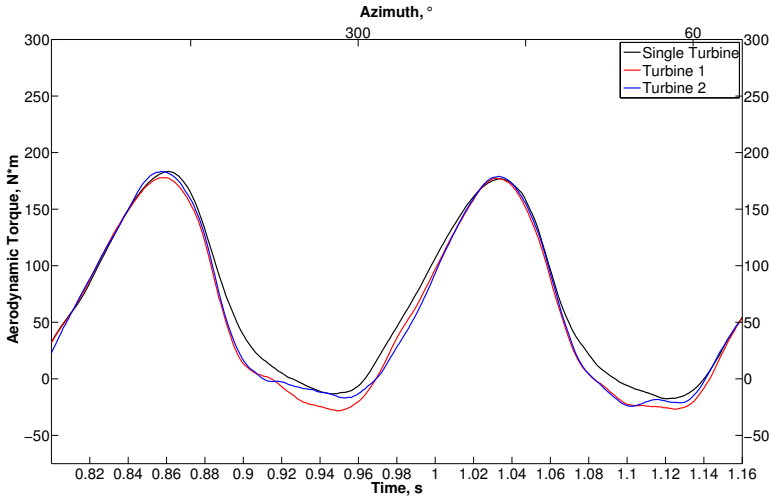


**Figure 2.8**: Time history of the aerodynamic torque for two VAWTs. The data for the second turbine is shifted by 60° to be in phase with the first turbine. Results from a single turbine simulation are plotted for comparison.

effect may be seen more clearly in Figure 2.10, which shows that one of the blades from the VAWT on the right is about to enter the turbulent region between the turbines.

### 2.3.2 Validation study using field test data

The computations presented in this section are performed for a 1.2 kW Windspire design [36], a three-bladed Darrieus VAWT (see Figure 2.11). The total height of the VAWT tower is 9.0 m, and the rotor height is 6.0 m. The rotor uses the DU06W200 airfoil profile with the chord length of 0.127 m, and is of the Giromill type with straight vertical blade sections attached to the main shaft with horizontal struts.

The aerodynamics simulations are carried out at realistic operating conditions, reported in the field test experiments conducted by the National Renewable Energy Lab (NREL) [3] and Caltech Field Laboratory for Optimized Wind Energy (FLOWE) [1,2]. For all cases, the air density and viscosity are set to 1.23 kg/m$^3$ and $1.78\times10^{-5}$ kg/(m·s), respectively.

The outer aerodynamics computational domain has the dimensions of 50 m, 20 m, and 30 m in the stream-wise, vertical, and span-wise directions, respectively,

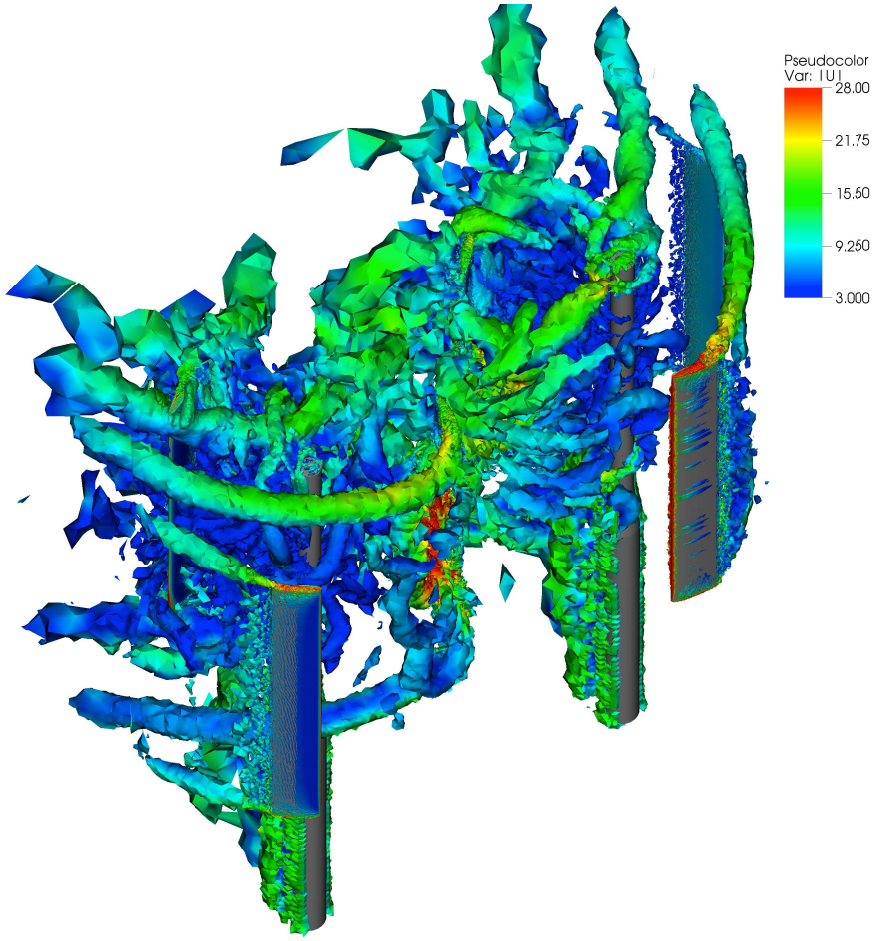


**Figure 2.9**: Vorticity isosurfaces at a time instant colored by flow speed for two VAWTs rotating counterclockwise.

and is shown in Figure 2.12. The VAWT centerline is located 15 m from the inflow and side boundaries. The radius and height of the inner cylindrical domain that encloses the rotor are 1.6 m and 7 m, respectively.

At the inflow, a uniform wind velocity profile is prescribed. On the top, bottom and side surfaces of the outer domain no-penetration boundary conditions are prescribed, while zero traction boundary conditions are set at the outflow.

The aerodynamics mesh has about 8 M elements, which are linear triangular prisms in the blade boundary layers, and linear tetrahedra elsewhere. The boundary layer mesh is constructed using 18 layers of elements, with the size of the first element

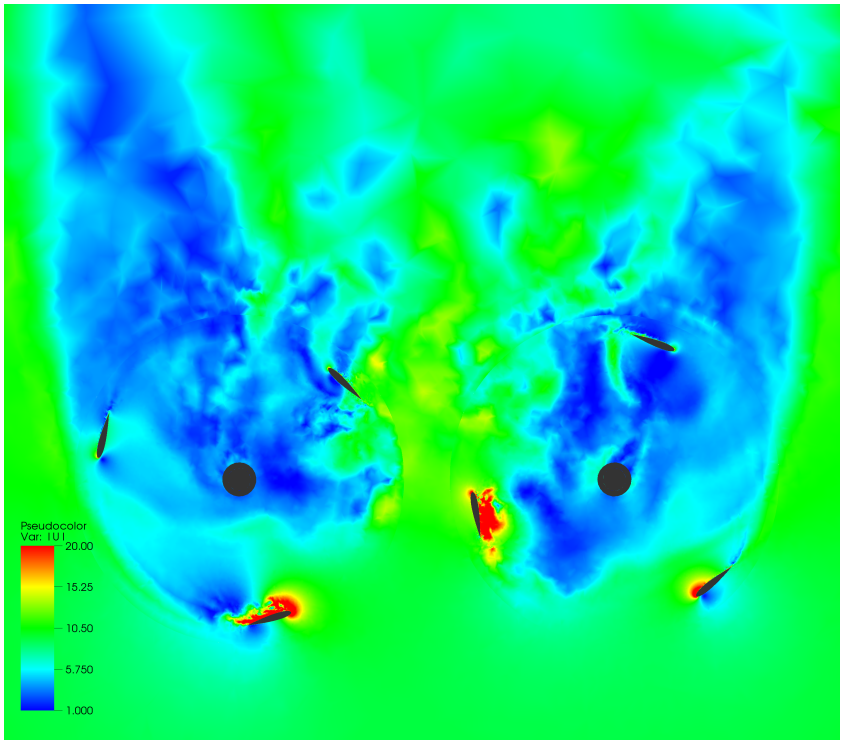


**Figure 2.10**: Air speed at a 2D cross-section for the two-VAWTs rotating counterclockwise.

in the wall-normal direction of 0.0003 m, and growth ratio of 1.1. The 2D slice of the mesh near the rotor is shown in Figure 2.13. Blade 1 is placed parallel to the flow with the airfoil leading edge facing the wind. Blades 2 and 3 are placed at an angle to the flow with the trailing edge facing the wind. (Blade numbering is shown in the figure.) Figure 2.14 shows the zoom on the boundary-layer mesh near one of the blades. The mesh design employed in this simulation is based on a refinement study performed for a Darrieus-type experimental turbine in Section 2.3.1.

All computations are carried out in a parallel computing environment. The mesh is partitioned into subdomains using METIS [79], and each subdomain is assigned to a compute core. The parallel implementation of the methodology may be found in [80]. The time step is set to $1.0 \times 10^{-5}$ s.

Two aerodynamic simulations are performed for the Windspire VAWT, one using the wind speed of 8.0 m/s and rotor speed of 32.7 rad/s, and another using the wind speed

**Figure 2.11**: A snapshot of Windspire VAWT from Caltech Field Laboratory for Optimized Wind Energy (FLOWE) [1, 2].

of 6.0 m/s and rotor speed of 20.6 rad/s. The time history of the aerodynamic torque for both cases is plotted in Figure 2.15 together with the experimental values reported from field-test experiments [1–3].

After the rotor undergoes a full revolution, a nearly periodic solution is attained in both cases. For 8.0 m/s wind the predicted average torque is 18.9 Nm, while its the experimentally reported value is about 12.7 Nm. For 6.0 m/s wind the predicted average torque is 9.5 Nm, while its the experimentally reported value is about 4.8 Nm.

In both cases the experimental value of the aerodynamic torque is derived from the average power produced by the turbine at the target rotor speed. The difference in the predicted and experimentally reported aerodynamic torque is likely due to the mechanical and electrical losses in the system, which are not reported. To estimate

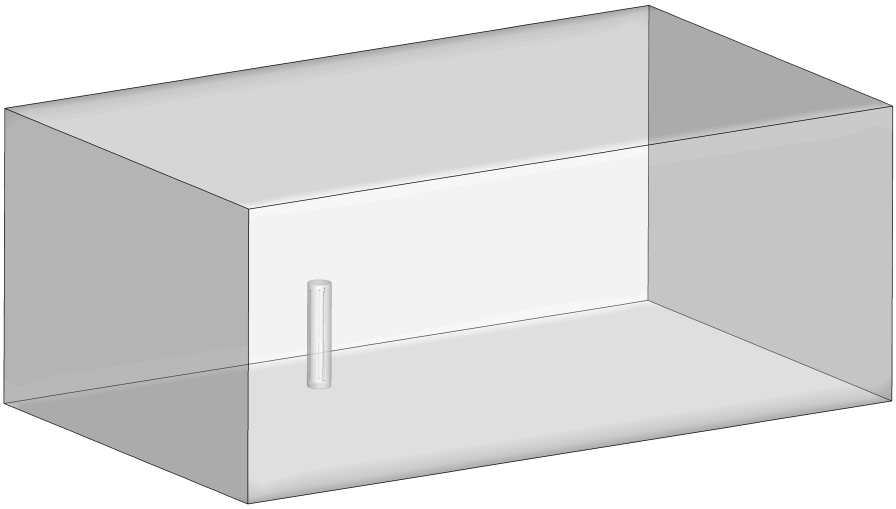

**Figure 2.12**: The VAWT aerodynamics computational domain in the reference configuration including the inner cylindrical region, outer region, and sliding interface that is now allowed to move in space as a rigid object.

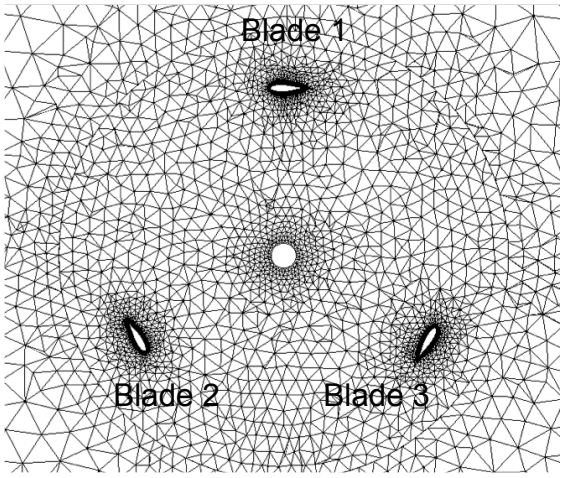


**Figure 2.13**: A 2D cross-section of the computational mesh along the rotor axis. The view is from the top of the turbine, and the blades are numbered counter-clock-wise, which is the expected direction of rotation. The sliding interface may be seen along a circular curve where the mesh appears to be non-conforming.

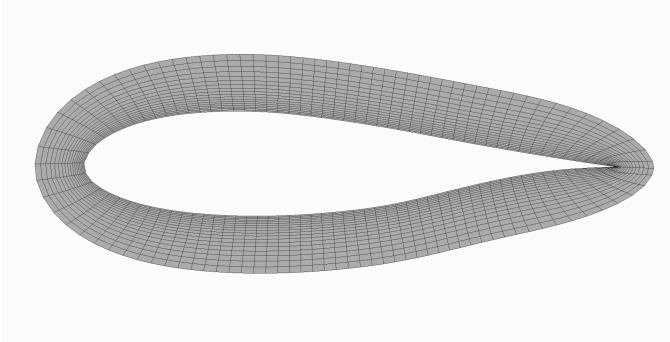

**Figure 2.14**: A 2D cross-section of the blade boundary-layer mesh consisting of triangular prisms.

those, we perform the following analysis. For simplicity, we assume that the torque loss is proportional to the rotational speed of the turbine, that is,

$$T_{\text{loss}} = c_{\text{loss}}\dot{\theta}. \tag{2.18}$$

Here $T_{\text{loss}}$ is taken as the difference between the predicted and reported torque values, $\dot{\theta}$ is the rotation speed, and $c_{\text{loss}}$ is the "loss" constant that characterizes the turbine. The data for the 8.0 m/s wind gives $c_{\text{loss}} = 0.19$ kg m$^2$/rad, while for 6.0 m/s wind we find that $c_{\text{loss}} = 0.23$ kg m$^2$/rad. The two values are reasonably close, which suggests that the torque overestimation is consistent with the loss model. In fact, this technique of combining experimental measurements and advanced computation may be employed to approximately estimate losses in wind turbines.

## 2.4 Acknowledgements

Chapter 2, in part, is a reprint of the material as it appears in: "Aerodynamic simulation of vertical-axis wind turbines," (with M.-C. Hsu, I. Akkerman and Y. Bazilevs), *Journal of Applied Mechanics*, 2013 and "FSI Modeling of Vertical- Axis Wind Turbines," (with Y. Bazilevs, X. Deng, J. Yan, M. Kinzel and J.O. Dabiri), *Journal of Applied Mechanics*, 2014. The dissertation author was the primary investigator and author of this paper.

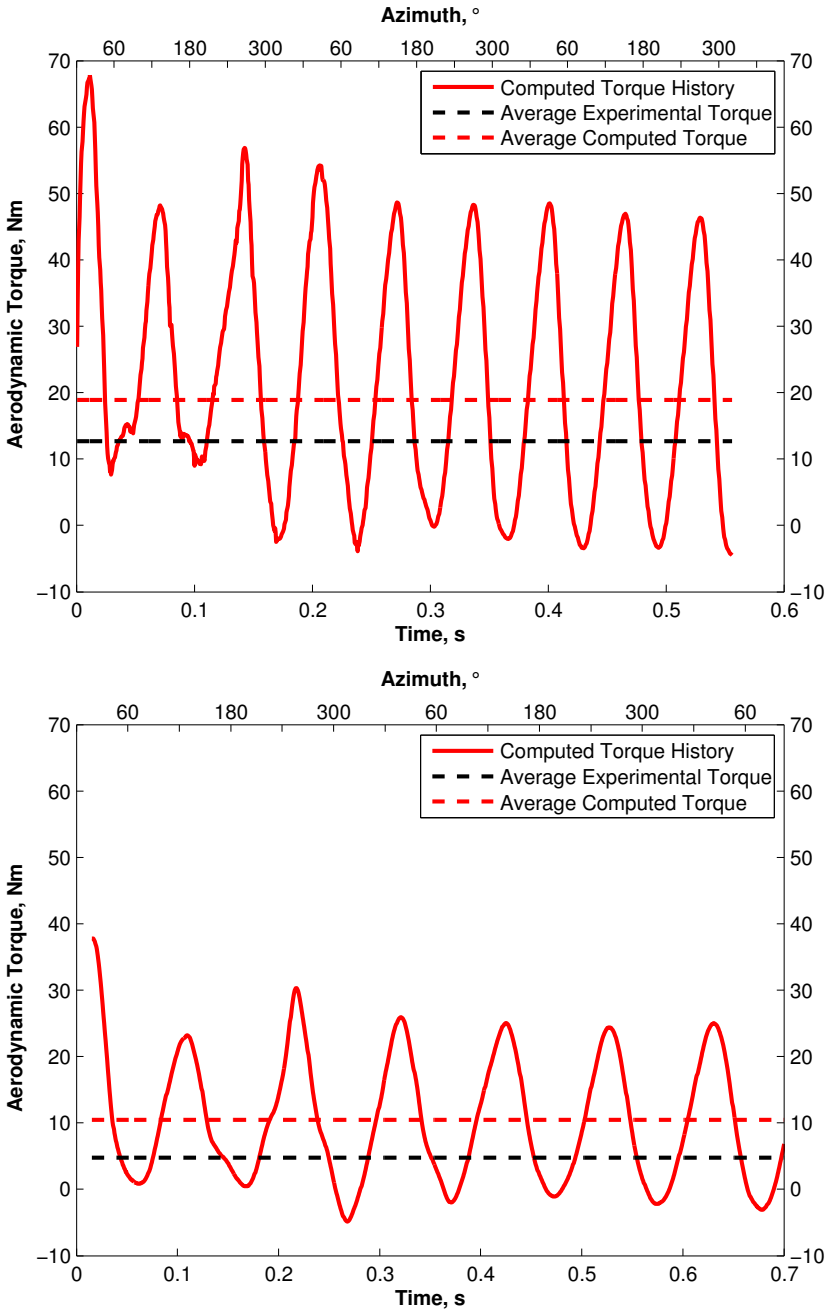


**Figure 2.15**: Time history of the aerodynamic torque for the pure aerodynamics simulations. a) 8.0 m/s wind with experimental data from [3]. b) 6.0 m/s wind with experimental data from [1, 2].

# Chapter 3

# Structural Mechanics Formulation

## 3.1 3D continuum description of structural mechanics

The main structural components of wind turbines are modeled using a combination of the recently proposed displacement-based Kirchhoff–Love shell [18, 52] and beam/cable [54] formulations. The shell formulation is used to represent wind turbine rotor, nacelle and a tower while the beam/cable formulation is used to describe the main shaft, struts in VAWT design and mooring cables in an application to offshore turbine designs, which however would not be covered in this work (see Figure 3.1 for examples). Both are discretized using IGA [55, 56] techniques based on Non-Uniform Rational B-Splines (NURBS) [57]. This approach gives a good combination of structural-mechanics accuracy due to the higher-order and higher-continuity representation of the geometry and solution, and efficiency due to the lack of rotational degrees of freedom in the formulation.

The governing equations of structural mechanics written in the Lagrangian frame [81] consist of the local balance of linear momentum, and are given by:

$$\rho_2 \left( \frac{\mathrm{d}^2 \mathbf{y}}{\mathrm{d}t^2} - \mathbf{f}_2 \right) - \boldsymbol{\nabla} \cdot \boldsymbol{\sigma}_2 = \mathbf{0}, \tag{3.1}$$

where $\rho_2$ is the structural density, $\mathbf{f}_2$ is the body force per unit mass, $\boldsymbol{\sigma}_2$ is the structural Cauchy stress, and $\mathbf{y}$ is the unknown structural displacement vector.

To state the variational formulation of structural mechanics we use a principal of

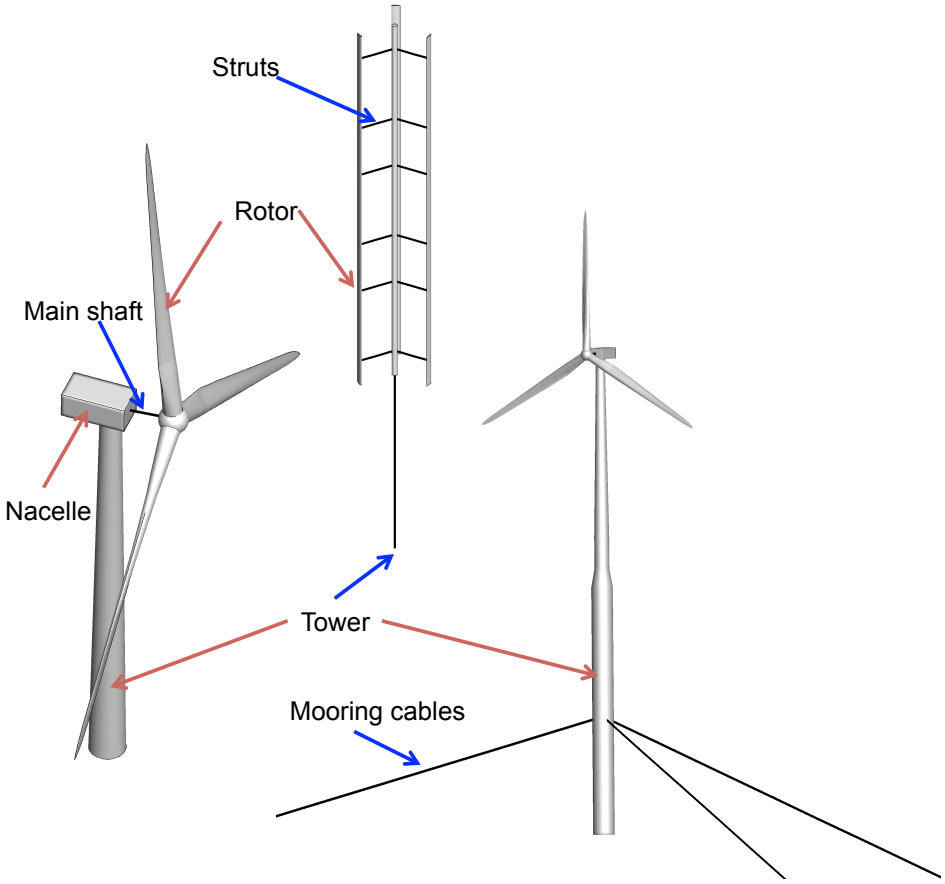


**Figure 3.1**: NURBS-based IGA structural model of a HAWT, VAWT and floating HAWT.

virtual work (see e.g. [81]), that is:

$$\delta W = \delta W_{int} + \delta W_{ext} = 0\,, \tag{3.2}$$

where $W$, $W_{int}$, and $W_{ext}$ are the total, internal, and external work, respectively, and $\delta$ denotes a variation with respect to the virtual displacement $\mathbf{w}_2$. Given the structural displacement $\mathbf{y}$, $\delta W$ is computed by taking the directional derivative of $W$ as

$$\delta W = \frac{d}{d\epsilon} W\left(\mathbf{y} + \epsilon \mathbf{w}_2\right)\Big|_{\epsilon=0}\,. \tag{3.3}$$

Here $\delta W_{ext}$ includes the virtual work done by inertia and body forces, and surface tractions, and is given by

$$\delta W_{ext} = \int_{\Omega_t^s} \mathbf{w}_2^h \cdot \rho_2 \left(\mathbf{f} - \frac{\mathrm{d}\mathbf{u}_2^h}{\mathrm{d}t}\right) \mathrm{d}\Omega + \int_{(\Gamma_t^s)_{2h}} \mathbf{w}_2^h \cdot \mathbf{h_2}\, \mathrm{d}\Gamma. \tag{3.4}$$

The virtual work done by internal stresses, $\delta W_{int}$, may be computed as

$$\delta W_{int} = -\int_{\Omega_0^s} (\delta \mathbf{E} \,:\, \mathbf{S}) \, \mathrm{d}\Omega \,, \tag{3.5}$$

where $\mathbf{S}$ is a second Piola–Kirchhoff stress tensor and $\delta\mathbf{E}$ is a variation of Green–Lagrange strain vector.

In Eqs. (3.4) and (3.5) $\Omega_0^s$ and $\Omega_t^s$ are the material domain of a structure in reference and current configuration respectively. The part of the boundary with traction boundary condition is denoted by $(\Gamma_t^s)_{2h}$.

Putting expressions for $W_{ext}$ and $W_{int}$ into Eq. (3.3) we arrive at the variational formulation of structural mechanics problem: find the structural velocity $\mathbf{u}_2^h \in \mathcal{S}_d^h$, such that $\forall \mathbf{w}_2^h \in \mathcal{V}_d^h$:

$$\int_{\Omega_t^s} \mathbf{w}_2^h \cdot \rho_2 \left( \frac{\mathrm{d}\mathbf{u}_2^h}{\mathrm{d}t} - \mathbf{f} \right) \mathrm{d}\Omega + \int_{\Omega_0^s} (\delta \mathbf{E} \,:\, \mathbf{S}) \, \mathrm{d}\Omega - \int_{(\Gamma_t^s)_{2h}} \mathbf{w}_2^h \cdot \mathbf{h_2} \, \mathrm{d}\Gamma = \mathbf{0}. \tag{3.6}$$

## 3.2 Kirchhoff–Love shell formulation

For shells the 3D continuum problem description reduced to that of the shell midsurface that defined as $\Gamma_0^s$ and $\Gamma_t^s$ in the reference and deformed configuration respectively. The transverse normal stress is neglected and it assumed, as a part of the Kirchhoff–Love theory, that the shell director remains normal to its middle surface during the deformation, which implies that the transverse shear strains are zero. As a result, only in-plane stress and strain tensors are considered, and the indices $\alpha = 1, 2$ and $\beta = 1, 2$ are employed to denote their components.

We introduce the following standard shell kinematic quantities and relationships

(see [52, 82] for more details):

$$E_{\alpha\beta} = \varepsilon_{\alpha\beta} + \xi_3 \kappa_{\alpha\beta}, \tag{3.7}$$

$$\varepsilon_{\alpha\beta} = \frac{1}{2}\left(\mathbf{g}_\alpha \cdot \mathbf{g}_\beta - \mathbf{G}_\alpha \cdot \mathbf{G}_\beta\right), \tag{3.8}$$

$$\kappa_{\alpha\beta} = -\frac{\partial \mathbf{g}_\alpha}{\partial \xi_\beta} \cdot \mathbf{g}_3 - (-\frac{\partial \mathbf{G}_\alpha}{\partial \xi_\beta} \cdot \mathbf{G}_3), \tag{3.9}$$

$$\mathbf{g}_\alpha = \frac{\partial \mathbf{x}}{\partial \xi_\alpha}, \tag{3.10}$$

$$\mathbf{G}_\alpha = \frac{\partial \mathbf{X}}{\partial \xi_\alpha}, \tag{3.11}$$

$$\mathbf{g}_3 = \frac{\mathbf{g}_1 \times \mathbf{g}_2}{\|\mathbf{g}_1 \times \mathbf{g}_2\|}, \tag{3.12}$$

$$\mathbf{G}_3 = \frac{\mathbf{G}_1 \times \mathbf{G}_2}{\|\mathbf{G}_1 \times \mathbf{G}_2\|}, \tag{3.13}$$

$$\mathbf{G}^\alpha = (\mathbf{G}_\alpha \cdot \mathbf{G}_\beta)^{-1} \mathbf{G}_\beta. \tag{3.14}$$

Here, $E_{\alpha\beta}$, $\varepsilon_{\alpha\beta}$, and $\kappa_{\alpha\beta}$ are the contravariant components of the in-plane Green–Lagrange strain, membrane strain, and curvature tensors, respectively. The spatial coordinates of the *shell midsurface* in the current and reference configurations are $\mathbf{x} = \mathbf{x}(\xi_1, \xi_2)$ and $\mathbf{X} = \mathbf{X}(\xi_1, \xi_2)$, parameterized by $\xi_1$ and $\xi_2$. $\xi_3$ is a through-thickness coordinate. The covariant surface basis vectors in the current and reference configurations are $\mathbf{g}_\alpha$ and $\mathbf{G}_\alpha$. The unit outward normal vectors to the shell midsurface in the current and reference configurations are $\mathbf{g}_3$ and $\mathbf{G}_3$. The contravariant surface basis vectors in the reference configuration are denoted by $\mathbf{G}^\alpha$.

We select the *local Cartesian basis* vectors as follows:

$$\bar{\mathbf{e}}_1 = \frac{\mathbf{G}_1}{\|\mathbf{G}_1\|}, \tag{3.15}$$

$$\bar{\mathbf{e}}_2 = \frac{\mathbf{G}_2 - (\mathbf{G}_2 \cdot \mathbf{e}_1)\mathbf{e}_1}{\|\mathbf{G}_2 - (\mathbf{G}_2 \cdot \mathbf{e}_1)\mathbf{e}_1\|}, \tag{3.16}$$

that is, the first local basis vector is the normalized first covariant basis vector in the reference configuration. The local Cartesian basis vectors $\bar{\mathbf{e}}_\alpha$ are used in expressing a constitutive relationship for the shell. Because the local basis is orthonormal, we make no distinction between covariant and contravariant quantities, which are expressed with respect to it.

With the above definitions, we calculate the components of the Green–Lagrange strain tensor and its variation in the local coordinate system as

$$\overline{E}_{\alpha\beta} = \overline{\varepsilon}_{\alpha\beta} + \xi_3 \overline{\kappa}_{\alpha\beta}, \tag{3.17}$$

$$\delta\overline{E}_{\alpha\beta} = \delta\overline{\varepsilon}_{\alpha\beta} + \xi_3 \delta\overline{\kappa}_{\alpha\beta}, \tag{3.18}$$

$$\overline{\varepsilon}_{\alpha\beta} = \varepsilon_{\gamma\delta}(\mathbf{G}^\gamma \cdot \overline{\mathbf{e}}_\alpha)(\mathbf{G}^\delta \cdot \overline{\mathbf{e}}_\beta), \tag{3.19}$$

$$\overline{\kappa}_{\alpha\beta} = \kappa_{\gamma\delta}(\mathbf{G}^\gamma \cdot \overline{\mathbf{e}}_\alpha)(\mathbf{G}^\delta \cdot \overline{\mathbf{e}}_\beta), \tag{3.20}$$

$$\delta\overline{\varepsilon}_{\alpha\beta} = \delta\varepsilon_{\gamma\delta}(\mathbf{G}^\gamma \cdot \overline{\mathbf{e}}_\alpha)(\mathbf{G}^\delta \cdot \overline{\mathbf{e}}_\beta), \tag{3.21}$$

$$\delta\overline{\kappa}_{\alpha\beta} = \delta\kappa_{\gamma\delta}(\mathbf{G}^\gamma \cdot \overline{\mathbf{e}}_\alpha)(\mathbf{G}^\delta \cdot \overline{\mathbf{e}}_\beta). \tag{3.22}$$

The variations $\delta\varepsilon_{\gamma\delta}$ and $\delta\kappa_{\gamma\delta}$ may be computed directly by taking the variational derivatives of the expressions given by Eqs. (3.8) and (3.9) with respect to the displacement vector.

We define the vectors of membrane strain and curvature components in the local coordinate system as

$$\overline{\boldsymbol{\varepsilon}} = \begin{bmatrix} \overline{\varepsilon}_{11} \\ \overline{\varepsilon}_{22} \\ \overline{\varepsilon}_{12} \end{bmatrix} \tag{3.23}$$

and

$$\overline{\boldsymbol{\kappa}} = \begin{bmatrix} \overline{\kappa}_{11} \\ \overline{\kappa}_{22} \\ \overline{\kappa}_{12} \end{bmatrix}, \tag{3.24}$$

together with a Green–Lagrange strain vector

$$\overline{\mathbf{E}} = \overline{\boldsymbol{\varepsilon}} + \xi_3 \overline{\boldsymbol{\kappa}}. \tag{3.25}$$

We assume St. Venant–Kirchhoff material law and write the following stress–strain relationship in the local coordinate system:

$$\overline{\mathbf{S}} = \overline{\mathbf{C}}\,\overline{\mathbf{E}}, \tag{3.26}$$

where $\overline{\mathbf{S}}$ is a vector of components of the second Piola–Kirchhoff stress tensor in the local coordinate system, and $\overline{\mathbf{C}}$ is a constitutive material matrix, which is symmetric.

With the above definitions, the expression for the internal virtual work for a composite shell may now be compactly written as

$$\delta W_{int} = -\int_{\Gamma_0^s} \delta\bar{\boldsymbol{\varepsilon}} \cdot \left(\mathbf{A}\bar{\boldsymbol{\varepsilon}} + \mathbf{B}\bar{\boldsymbol{\kappa}}\right) \mathrm{d}\Gamma - \int_{\Gamma_0^s} \delta\bar{\boldsymbol{\kappa}} \cdot \left(\mathbf{B}\bar{\boldsymbol{\varepsilon}} + \mathbf{D}\bar{\boldsymbol{\kappa}}\right) \mathrm{d}\Gamma. \tag{3.27}$$

To model the composite layup of the blade structure, classical laminated plate theory [83] is employed. The shell thickness is denoted by $t_{th}$, the thickness of the $k^{\text{th}}$ ply by $t_k$, and its centroid by $\bar{z}_k$ (see Figure 3.2). With these definitions, in Eq. (3.27), the extensional, coupling, and bending stiffnesses, given by **A**, **B**, and **D** matrices, respectively, may be computed for *any* layup as

$$\mathbf{A} = \int_{t_{th}} \overline{\mathbf{C}}\, d\xi_3 = \sum_{k=1}^{n} \overline{\mathbf{C}}_k t_k, \tag{3.28}$$

$$\mathbf{B} = \int_{t_{th}} \xi_3 \overline{\mathbf{C}}\, d\xi_3 = \sum_{k=1}^{n} \overline{\mathbf{C}}_k t_k \overline{z_k}, \tag{3.29}$$

$$\mathbf{D} = \int_{t_{th}} {\xi_3}^2 \overline{\mathbf{C}}\, d\xi_3 = \sum_{k=1}^{n} \overline{\mathbf{C}}_k \left(t_k \overline{z_k^2} + \frac{t_k^3}{12}\right). \tag{3.30}$$

Here, $\overline{\mathbf{C}}$ is a constitutive material matrix in the local coordinate system given by

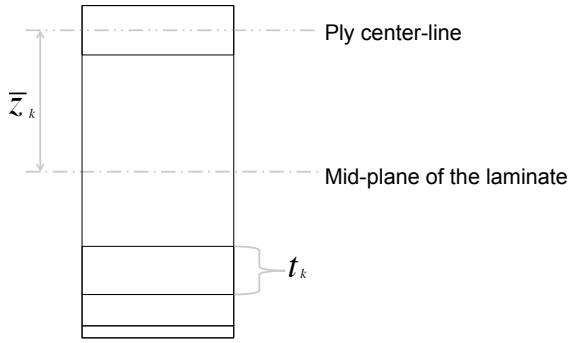


**Figure 3.2**: Composite layup with nonuniform and nonsymmetric distribution of the lamina.

$$\overline{\mathbf{C}}_k = \mathbf{T}^T(\phi_k)\, \overline{\mathbf{C}}_{ort}\, \mathbf{T}(\phi_k), \tag{3.31}$$

$$\mathbf{T}(\phi) = \begin{bmatrix} \cos^2\phi & \sin^2\phi & \sin\phi\cos\phi \\ \sin^2\phi & \cos^2\phi & -\sin\phi\cos\phi \\ -2\sin\phi\cos\phi & 2\sin\phi\cos\phi & \cos^2\phi - \sin^2\phi \end{bmatrix}, \tag{3.32}$$

where $\phi$ denotes the fiber orientation angle in each ply and $\mathbf{C}_{ort}$ is the constitutive matrix for the orthotropic material written with respect to the principal material axes (see [53] for more details).

The complete variational formulation of the rotation-free Kirchhoff–Love shell is stated as follows: find the velocity of the shell midsurface $\mathbf{u}_2^h \in \mathcal{S}_d^h$, such that $\forall \mathbf{w}_2^h \in \mathcal{V}_d^h$,

$$\begin{aligned}
&\int_{\Gamma_t^s} \mathbf{w}_2^h \cdot \overline{\rho_2} t_{th} \left( \frac{\mathrm{d}\mathbf{u}_2^h}{\mathrm{d}t} - \mathbf{f}_2^h \right) \mathrm{d}\Gamma \\
&+ \int_{\Gamma_0^s} \delta\overline{\boldsymbol{\varepsilon}}^h \cdot \left( \mathbf{A}\overline{\boldsymbol{\varepsilon}}^h + \mathbf{B}\overline{\boldsymbol{\kappa}}^h \right) \mathrm{d}\Gamma \\
&+ \int_{\Gamma_0^s} \delta\overline{\boldsymbol{\kappa}}^h \cdot \left( \mathbf{B}\overline{\boldsymbol{\varepsilon}}^h + \mathbf{D}\overline{\boldsymbol{\kappa}}^h \right) \mathrm{d}\Gamma \\
&- \int_{(\Gamma_t^s)_{2h}} \mathbf{w}_2^h \cdot \mathbf{h_2} \, \mathrm{d}\Gamma = 0.
\end{aligned} \tag{3.33}$$

Here, $\overline{\rho_2}$ is the through-thickness-averaged shell density given by

$$\overline{\rho_2} = \frac{1}{t_{th}} \int_{t_{th}} \rho_2 \, \mathrm{d}\xi_3. \tag{3.34}$$

The shell midsurface is described using a patch-wise smooth ($C^1$- or higher-order continuous) geometrical mapping with reduced regularity of the mapping ($C^0$-continuity) at the patch interconnections. This leads to non-integrable singularity at a region with $C^0$-continuity, due to the term in formulation involving second order derivative. To handle this problem, the structural mechanics formulation is augmented with the term $\int_{\Gamma_0^b} \delta\overline{\boldsymbol{\kappa}}^h \cdot \mathbf{D}^b \overline{\boldsymbol{\kappa}}^h \, \mathrm{d}\Gamma$, which represents the contribution of bending strip patches, that added at the interface of original NURBS patches. The material in bending strip patches is assumed to have zero mass, zero membrane stiffness and only the bending stiffness in the direction transverse to the interface. As a result the bending moment is transferred correctly between the NURBS patches (see [18, 52, 53] for more details). The bending strip domain is defined as $\Gamma_0^{\mathrm{b}}$, which is the union of the bending strip patch subdomains, in the reference configuration.

## 3.3 Kirchhoff–Love shell eigenfrequency analysis

In this section we state the eigenvalue problem for the Kirchhoff–Love shell formulation given by Eq. (3.33) with addition of the bending strip term: find all eigenpairs

$\{\mathbf{d}^h, \omega^h\}$, such that $\forall \mathbf{w}_2^h$

$$
\begin{aligned}
&- \int_{\Gamma_t^s} \mathbf{w}_2^h \cdot \rho h_{th} (\omega^h)^2 \mathbf{d}^h \, \mathrm{d}\Gamma \\
&+ \int_{\Gamma_0^s} \delta\bar{\boldsymbol{\varepsilon}}^h \cdot \left( \mathbf{A}\bar{\boldsymbol{\varepsilon}}^h + \mathbf{B}\bar{\boldsymbol{\kappa}}^h \right) \mathrm{d}\Gamma \\
&+ \int_{\Gamma_0^s} \delta\bar{\boldsymbol{\kappa}}^h \cdot \left( \mathbf{B}\bar{\boldsymbol{\varepsilon}}^h + \mathbf{D}\bar{\boldsymbol{\kappa}}^h \right) \mathrm{d}\Gamma \\
&+ \int_{\Gamma_0^b} \delta\bar{\boldsymbol{\kappa}}^h \cdot \mathbf{D}^b \bar{\boldsymbol{\kappa}}^h \, \mathrm{d}\Gamma = 0.
\end{aligned} \tag{3.35}
$$

Here, $\omega^h$ is the natural frequency and $\mathbf{d}^h$ is the corresponding mode shape. The matrix form corresponding to the discrete formulation given by Eq. (3.35) becomes: find the $k^{\text{th}}$ eigenfrequency $\omega_k^h$ and the corresponding eigenvector $\boldsymbol{\psi}_k$, $k = 1, ..., n_{eq}$, where $n_{eq}$ is the number of equations in the linear system, such that

$$
\left( \mathbf{K} - (\omega_k^h)^2 \mathbf{M} \right) \boldsymbol{\psi}_k = \mathbf{0}. \tag{3.36}
$$

In Eq. (3.36), $\mathbf{K}$ and $\mathbf{M}$ are structure stiffness and mass matrices, respectively. The stiffness matrix is evaluated by linearizing the Kirchhoff–Love shell formulation around the undeformed stress-free configuration of the structure.

## 3.4 Validation study of the rotation-free Kirchhoff–Love isogeometric shell formulation for a full-scale wind turbine blades

In the following subsection we present a verification analysis of the rotation-free Kirchhoff–Love isogeometric shell formulation for a two wind turbine blades, that will be used in FSI analysis in Chapter 4.

### 3.4.1 CX-100 blade of Micon 65/13M wind turbine

The CX-100 blade is a conventional carbon-spar blade design [84, 85] with length of 9 m adopted in Micon 65/13M wind turbine design. It based on the ERS-100 blade [85], but, with a substantially reduced spar cap. The NREL S821, S819 and

S820 airfoils are used to define the blade geometry. The details of the blade geometry definition are provided in Table 3.1.

**Table 3.1**: Geometry data for the CX-100 blade.

| Radial Distance (m) | Chord Length (m) | Twist Angle (degrees) | Airfoil Type |
|---|---|---|---|
| 0.200 | 0.356 | 29.6 | Cylinder |
| 0.600 | 0.338 | 24.8 | Cylinder |
| 1.000 | 0.569 | 20.8 | Cylinder |
| 1.400 | 0.860 | 17.5 | NREL S821 |
| 1.800 | 1.033 | 14.7 | NREL S821 |
| 2.200 | 0.969 | 12.4 | NREL S821 |
| 3.200 | 0.833 | 8.3 | NREL S821 |
| 4.200 | 0.705 | 5.8 | NREL S819 |
| 5.200 | 0.582 | 4.0 | NREL S819 |
| 6.200 | 0.463 | 2.7 | NREL S819 |
| 7.200 | 0.346 | 1.4 | NREL S819 |
| 8.200 | 0.232 | 0.4 | NREL S819 |
| 9.000 | 0.120 | 0.0 | NREL S820 |

**Table 3.2**: Mechanical properties of the materials used in CX-100 blade.

| Material Name | $E_1$ $(GPa)$ | $E_2$ $(GPa)$ | $G_{12}$ $(GPa)$ | $\nu_{12}$ | $\rho$ $(kg/m^3)$ | $t_k$ $(mm)$ |
|---|---|---|---|---|---|---|
| Gel coat | 3.44 | 3.44 | 1.38 | 0.30 | 1235 | 0.13 |
| Fill epoxy | 2.41 | 2.41 | 0.96 | 0.30 | 1154 | 0.51 |
| Fiberglass | 7.58 | 7.58 | 4.00 | 0.30 | 1678 | 0.38 |
| End-grain balsa | 0.12 | 0.12 | 0.02 | 0.30 | 230 | 6.35 |
| DBM1708 (+/- 45° fiberglass) | 9.58 | 9.58 | 6.89 | 0.39 | 1814 | 0.89 |
| DBM1208 (+/- 45° fiberglass) | 9.58 | 9.58 | 6.89 | 0.39 | 1814 | 0.56 |
| C520 (0° fiberglass) | 37.30 | 7.60 | 6.89 | 0.31 | 1874 | 1.32 |
| 0° Carbon, 500 gsm | 105.40 | 6.82 | 3.32 | 0.28 | 1480 | 0.63 |
| Carbon-fiberglass triaxial fabric | 84.10 | 8.76 | 4.38 | 0.21 | 1560 | 0.63 |

The blade surface is comprised of five primary zones: leading edge, trailing edge, root, spar cap, and shear web. The zones are shown in Figure 3.4. Each zone is made up of a multilayer composite layup. The different materials used for the layups are summarized in Table 3.2. The root area has many layers of fiberglass plies to strengthen the region where the blade is mounted on the hub flange. The leading and trailing

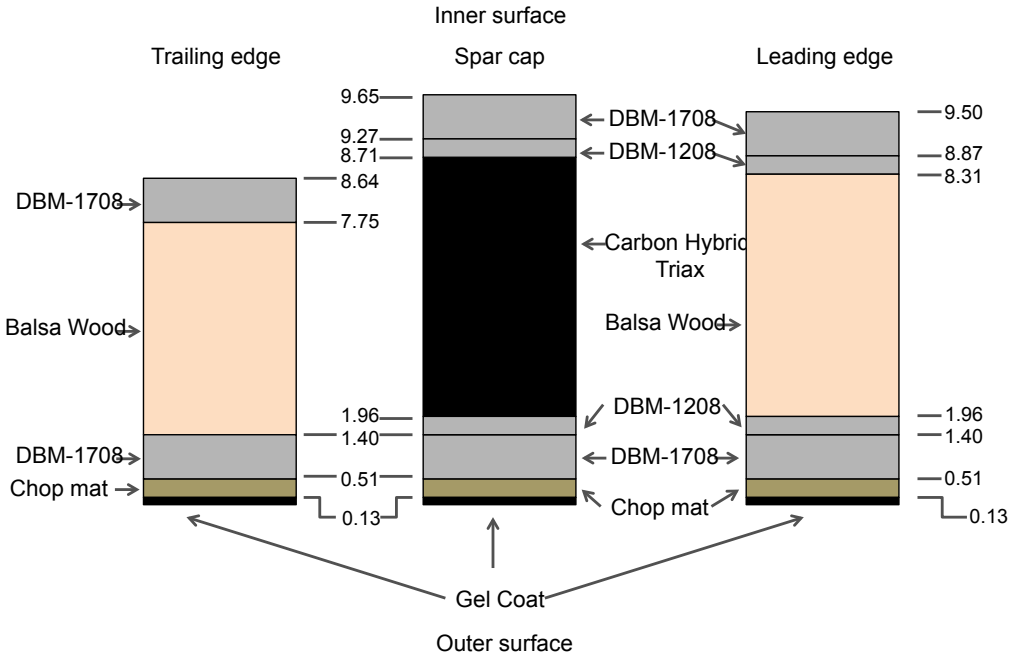


**Figure 3.3**: Layups of the core regions of the trailing edge, leading edge, and spar cap.

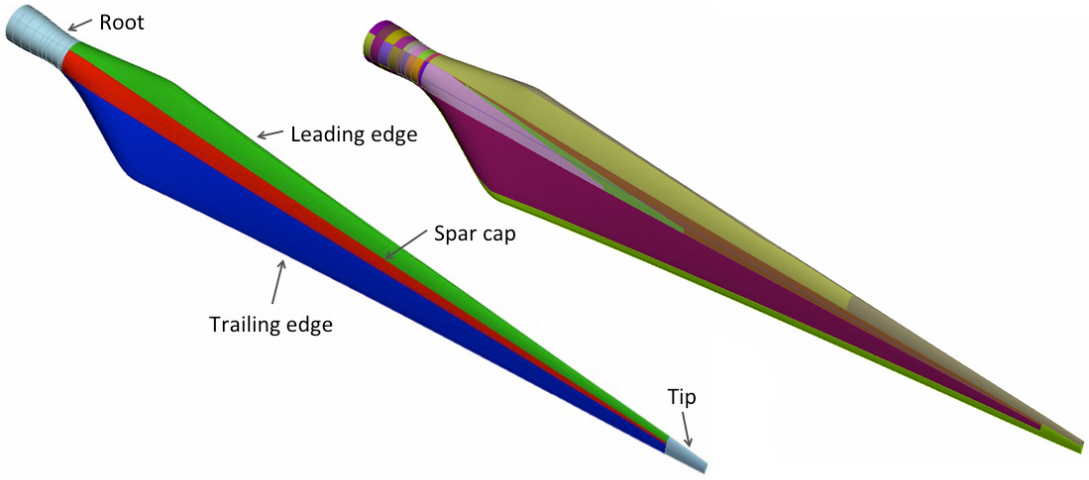


**Figure 3.4**: Left: Five primary sections of the CX-100 blade; Right: 32 distinct material zones of the CX-100 blade.

edge zones have a similar layup. Both include the outer gel coat and fiberglass layers, with the total thickness of 0.51 mm, as well as additional layers of fiberglass material DBM-1708, 0.89 mm each, and one 6.35 mm layer of balsa wood. Balsa wood is only

present in the core section of the blade and not on the edges. The leading edge zone has additional layers of fiberglass material DBM-1208, with a total thickness of 0.56 mm, between the DBM-1708 and balsa core. The layups of the core regions of the trailing and leading edge zones are shown in Figure 3.3. The spar-cap zone has a nonuniform thickness distribution, ranging from 5.79 mm to 9.65 mm, due to the decreasing number of carbon fiber laminate layers (from seven to three) along the blade length. The spar-cap layup is also shown in Figure 3.3, and has the thickest carbon fiber layer. The shear web, which is designed to carry most of the surface loads, has a C-shape structure containing four layers of DBM-1708 fiberglass, 0.74 mm each, and 9.53 mm of balsa wood core. The balsa wood layer is terminated in the tip zone. As a result, the tip region is only comprised of one layer of gel coat and several layers of fiberglass material. This layout leads to 32 zones with constant total thickness and unique laminate stacking in each zone. The effective material properties for each of the zones are computed using the procedures described in the previous section. All 32 zones are identified on the blade surface and are shown in Figure 3.4.

**Table 3.3**: NURBS blade meshes used in the eigenfrequency analysis of CX-100 blade.

| | Number of Control Points | Number of Elements |
|---|---|---|
| Mesh 1 | 3,469 | 1,846 |
| Mesh 2 | 7,411 | 4,647 |
| Mesh 3 | 25,896 | 18,611 |

**Table 3.4**: Blade mass and position of CG for the three meshes used in the eigenfrequency analysis of CX-100 blade.

| | Mass (kg) | CG (m) |
|---|---|---|
| Mesh 1 | 173.34 | 2.224 |
| Mesh 2 | 172.96 | 2.217 |
| Mesh 3 | 173.05 | 2.216 |
| Experiment | 175.54 | 2.38 |

We perform eigenfrequency calculations using the CX-100 blade using three quadratic NURBS meshes. The coarsest mesh has 1,846 elements, while the finest mesh has 18,611 elements. The mesh statistics are summarized in Table 3.3. Table 3.4 gives

**Table 3.5**: Comparison of experimentally measured and computed natural frequencies corresponding to the first few bending modes for the free case.

| Mode: | $1^{st}$ Flapwise (Hz) | $1^{st}$ Eidgewise (Hz) | $2^{nd}$ Flapwise (Hz) |
|---|---|---|---|
| Mesh 1 | 8.28 | 15.92 | 19.26 |
| Mesh 2 | 8.22 | 15.61 | 18.21 |
| Mesh 3 | 8.22 | 15.6 | 18.01 |
| Experiment | 7.6 - 8.2 | 15.7 - 18.1 | 20.2 - 21.3 |

**Table 3.6**: Comparison of experimentally measured and computed natural frequencies corresponding to the first few bending modes for the clamped case.

| Mode: | $1^{st}$ Flapwise (Hz) | $2^{nd}$ Flapwise (Hz) | $3^{rd}$ Flapwise (Hz) |
|---|---|---|---|
| Mesh 1 | 4.33 | 11.82 | 19.69 |
| Mesh 2 | 4.29 | 11.61 | 19.08 |
| Mesh 3 | 4.27 | 11.54 | 18.98 |
| Experiment | 4.35 | 11.51 | 20.54 |

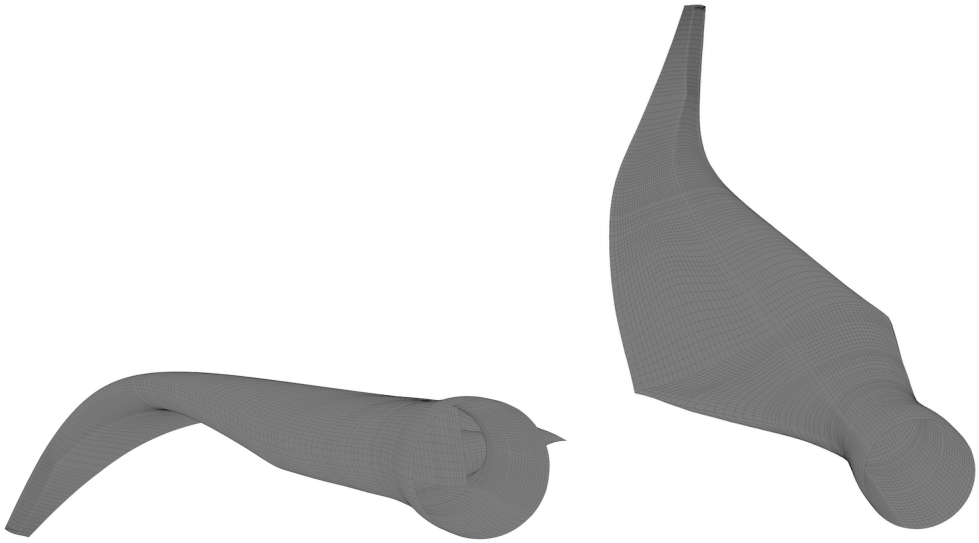

(a) (b)

**Figure 3.5**: First flapwise bending mode (a) and first edgewise bending mode (b) for the free case.

the blade mass and position of the center of gravity (CG). Note that, although the blade geometry is “exact” and stays unchanged with mesh refinement, because the mesh lines

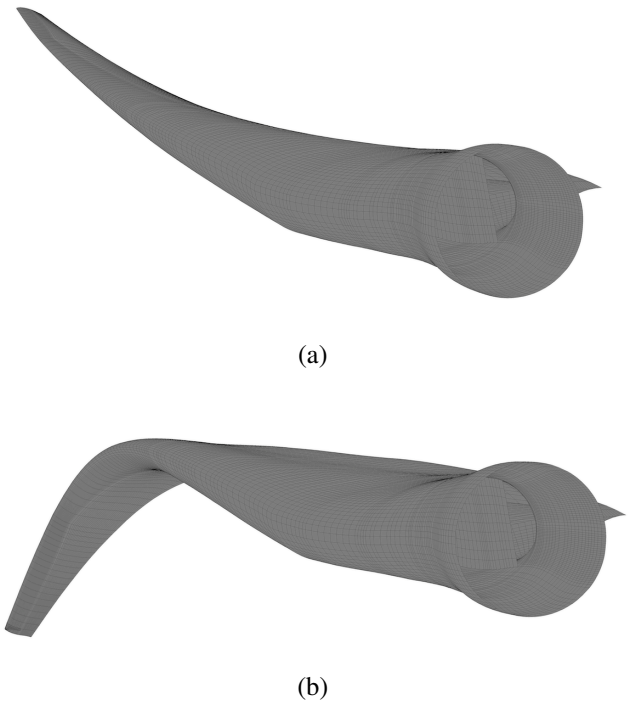

(a)

(b)

**Figure 3.6**: First flapwise bending mode (a) and second flapwise bending mode (b) for the clamped case.

do not conform to the 32 different material zones, there is a very small variation in the blade mass and center-of-gravity position from one mesh to the other.

The eigenfrequency results are compared with the experimental data from [86, 87]. We compute the case with free boundary conditions and the case when the blade is clamped at the root. For the free case the eigenfrequencies for the first and second flapwise bending modes and for the first edgewise bending mode are summarized in Table 3.5. The experimental eigenfrequencies are obtained for this blade at Sandia National Laboratories (SNL), Los Alamos National Laboratory (LANL), and the University of Massachusetts Lowell Structural Dynamics and Acoustics Laboratory (UML SDASL), and reported in [87]. Table 3.5 provides a range of experimental eigenfrequency values. For the clamped case, the eigenfrequencies for the first three bending modes are compared with the results of the tests performed at the National Renewable Energy Laboratory (NREL) [87]. In both cases, the computed natural frequencies are in good agreement with the experimental data (see Table 3.5). The medium mesh shows

a good balance between the computational cost and accuracy of the results. For this reason, this mesh is chosen for the FSI computations presented in Chapter 4. The mode shapes computed using the medium mesh are shown in Figures 3.5 and 3.6.

### 3.4.2 Natural frequency computations of SNL blade design for an offshore wind turbines

A 100 m baseline wind turbine blade design analyzed in this section is developed by Sandia National Laboratory. It was initially developed based on the geometry and composite layup of the 61 m baseline offshore designs employed in the NREL, DOWEC and UpWind projects [4]. The details of blade geometry are provided in Table 3.7. The SNL 100-00 blade was obtained by a simple scaling of the 61 m design and its additional minor modifications to increase the load carrying capacity. The trailing and leading edge reinforcements together with the root build-up were redesigned. Three shear webs were placed to minimize the length of the unsupported panel (see Figure 3.7 for details). The blade laminate has six principal regions: root, spar cap, trailing edge reinforcement,

**Table 3.7**: Geometry data for the SNL 100-00 blade. The nomenclature follows that used in [5]. "Pitch Angle Fraction" is the distance from the leading edge of the blade pitch axis expressed as a cord-length fraction.

| Section Number | Blade Fraction | Chord Length (m) | Twist Angle (deg) | Pitch Angle Fraction | Airfoil Type |
|---|---|---|---|---|---|
| 1 | 0.000 | 5.694 | 13.308 | 0.500 | Cylinder |
| 2 | 0.195 | 7.628 | 12.915 | 0.380 | DU99-W-405 |
| 3 | 0.358 | 6.923 | 9.166 | 0.375 | DU97-W-300 |
| 4 | 0.602 | 5.417 | 4.743 | 0.375 | DU93-W-210 |
| 5 | 0.732 | 4.621 | 2.735 | 0.375 | NACA-64-618 |
| 6 | 0.765 | 4.422 | 2.348 | 0.375 | NACA-64-618 |
| 7 | 0.846 | 3.925 | 1.380 | 0.375 | NACA-64-618 |
| 8 | 0.895 | 3.619 | 0.799 | 0.375 | NACA-64-618 |
| 9 | 0.944 | 2.824 | 0.280 | 0.375 | NACA-64-618 |
| 10 | 0.957 | 2.375 | 0.210 | 0.375 | NACA-64-618 |
| 11 | 0.972 | 1.836 | 0.140 | 0.375 | NACA-64-618 |
| 12 | 0.986 | 1.208 | 0.070 | 0.375 | NACA-64-618 |
| 13 | 1.000 | 0.100 | 0.000 | 0.375 | NACA-64-618 |

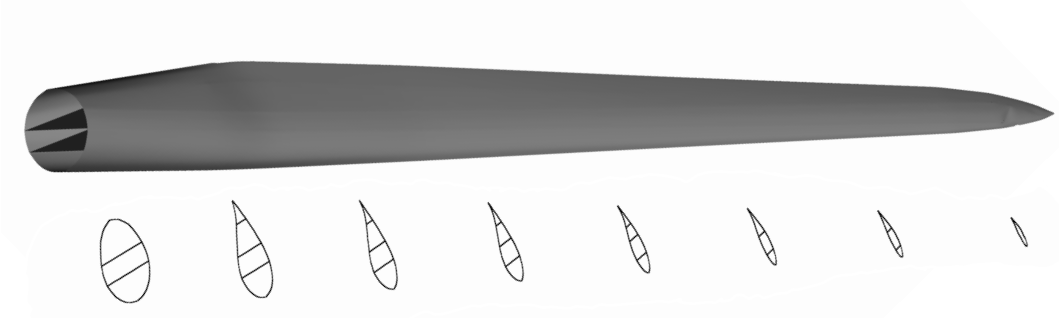

**Figure 3.7**: SNL 100-00 blade shell model with several cross-section cuts to show the arrangement of the three shear webs.

**Table 3.8**: Orthotropic materials used in the SNL 100-00 blade.

| Material Type | Lay-up | $E_1$ (GPa) | $E_2$ (GPa) | $G_{12}$ (GPa) | $\nu_{12}$ | Density (kg/m$^3$) |
|---|---|---|---|---|---|---|
| E-LT-5500/EP-3 | $[0]_2$ | 41.8 | 14 | 2.63 | 0.28 | 1920 |
| Saertex/EP-3 | $[\pm 45]_4$ | 13.6 | 13.3 | 11.8 | 0.51 | 1780 |
| SNL Triax | $[\pm 45]_4[0]_2$ | 27.7 | 13.65 | 7.2 | 0.39 | 1850 |

**Table 3.9**: Isotropic materials used in the SNL 100-00 blade.

| Material Type | $E_1$ (GPa) | $E_2$ (GPa) | $G_{12}$ (GPa) | $\nu_{12}$ | Density (kg/m$^3$) |
|---|---|---|---|---|---|
| Foam | 0.256 | 0.256 | 0.022 | 0.3 | 200 |
| Resin | 3.5 | 3.5 | 1.4 | 0.3 | 1100 |
| Gel Coat | 3.44 | 3.44 | 1.38 | 0.3 | 1235 |

leading edge panels, aft panels and shear webs.

Tables 3.8 and 3.9 list the materials used in the blade design. The root buildup is composed of triaxial material (SNL Triax), and the whole internal and external blade surfaces have a 5 mm layer of this material. As the root buildup tapers down in thickness, the spar cap increases in thickness. The maximum thickness of the spar cap is 136 mm at maximum chord (19.5%), while the minimum thickness of the spar cap is 5 mm, starting at 94.4% of the blade span and continuing almost all the way to the tip. The trailing edge is reinforced with uniaxial laminate E-LT-5500/EP-3 and foam materials. The trailing edge reinforcement has a constant width of 1.0 m that continues until 94.4% span, and

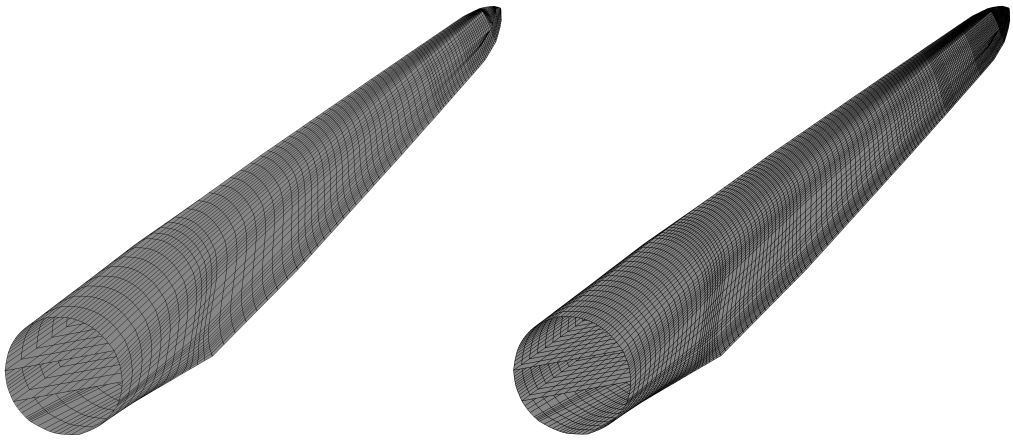

**Figure 3.8**: SNL 100-00 blade NURBS meshes. Left: Medium; Right: Fine.

**Table 3.10**: SNL 100-00 blade NURBS mesh statistics.

| | Elements | Control Points |
|---|---|---|
| Coarse Mesh | 1,166 | 926 |
| Medium Mesh | 3,568 | 3,026 |
| Fine Mesh | 7,416 | 6,628 |

then tapers to the tip. To improve buckling resistance and minimize the weight, foam is also chosen as the core material for the leading panel and aft panels. Longitudinal fibers of E-LT-5500/EP-3 are placed on the spar cap to improve the flapwise bending stiffness. The spar cap has a constant width of 1.5 m. As a result, the two principal shear webs, which begin at 2.4 m and terminate at 94.4 m, are positioned 0.75 m before and after the pitch axis. The third shear web starts at 14.6 m and terminates at 60.2 m, and is positioned at 78% chord at its starting location and 68% chord at its terminal location. A combination of foam and Saertex/EP-3 is used in shear webs to enhance the shear stiffness. An extra 5 mm of epoxy resin is included in the internal blade surface, and the external surface includes 0.6 mm of gelcoat. The same layup is employed for both low- and high-pressure blade surfaces.

We perform the natural frequency analysis of the blade model assumed to be clamped at the root. Three quadratic NURBS meshes of increasing resolution are employed in the computations. The medium and fine meshes and shown in Figure 3.8. The mesh statistics are summarized in Table 3.10. The blade total mass for each mesh

**Table 3.11**: SNL 100-00 blade total mass. Data from reference [4] is presented for comparison.

| | Computed Mass (kg) | Mass from Reference (kg) |
|---|---|---|
| Coarse Mesh | 113,520.9 | 114,172.0 |
| Medium Mesh | 115,969.3 | |
| Fine Mesh | 115,601.6 | |

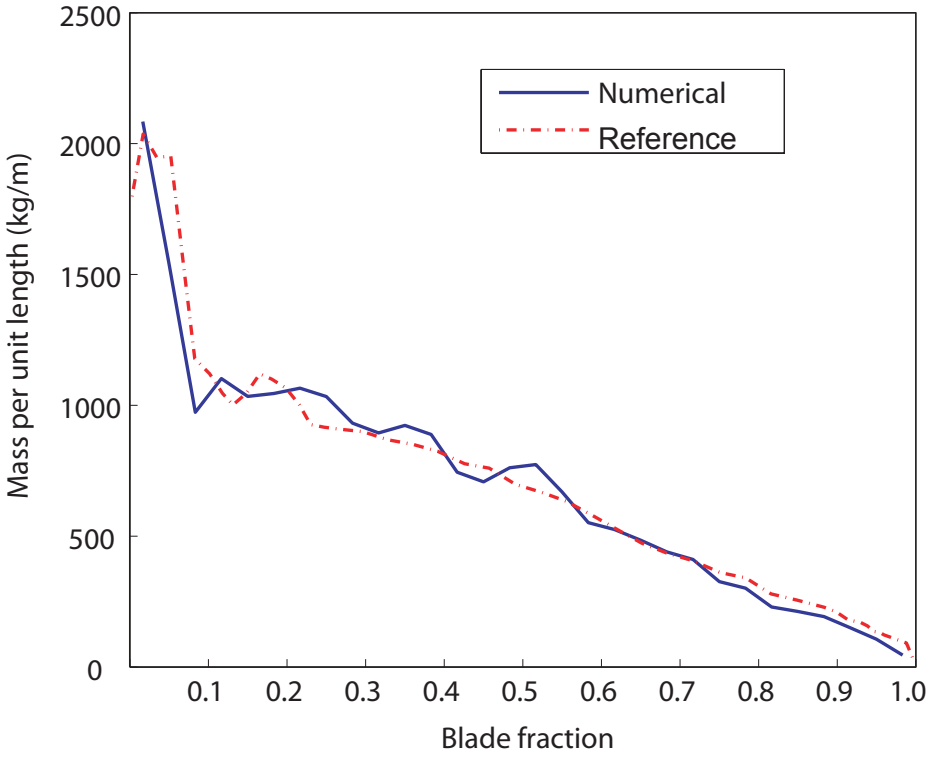


**Figure 3.9**: SNL 100-00 blade mass distribution along the blade axis. Data from [4] are plotted for comparison.

is reported in Table 3.11, and the mass distribution along the blade axis is plotted in Figure 3.9. The eigenfrequencies for the three meshes are summarized in Table 3.12 and, where applicable, compared to the results reported in [6]. Very good agreement is observed in all the quantities reported. Convergence of the natural frequencies occurs from the high side, as expected. This is the first time that natural frequencies beyond the first flapwise and edgewise modes are reported for this blade design.

For the FSI computation presented in Chapter 4 the medium NURBS mesh is

**Table 3.12**: SNL 100-00 blade natural frequencies. The IGA computational results are compared with the reported values from [6], where available. The values from the reference do not come from actual experiments, but from a beam model of the same blade.

| Mode Number and Type | Results from SNL Report (Hz) | IGA Results (Hz) | | |
|---|---|---|---|---|
| | | Coarse Mesh | Medium Mesh | Fine Mesh |
| 1st Flapwise Bending | 0.42 | 0.456 | 0.454 | 0.453 |
| 1st Edgewise Bending | 0.69 | 0.681 | 0.678 | 0.679 |
| 2nd Flapwise Bending | N/A | 1.241 | 1.225 | 1.222 |
| 2nd Edgewise Bending | N/A | 2.225 | 2.178 | 2.171 |
| 3rd Flapwise Bending | N/A | 2.544 | 2.498 | 2.487 |
| 1st Axial Torsion | N/A | 3.882 | 3.725 | 3.666 |

employed. Furthermore, for the FSI computation, the 100 m blade is scaled back to 61 m.

## 3.5 Acknowledgements

Chapter 3, in part, is a reprint of the material as it appears in: "Structural mechanics modeling and FSI simulation of wind turbines," (with M.-C. Hsu, I. Akkerman, J. Tippmann and Y. Bazilevs), *Mathematical Models and Methods in Applied Science*, 2013 and "Novel Structural Modeling and Mesh Moving Techniques for Advanced FSI Simulation of Wind Turbines," (with Y. Bazilevs, X. Deng and J. Yan), *International Journal for Numerical Methods in Engineering*, 2014. The dissertation author was the primary investigator and author of this paper.

# Chapter 4

# Advanced FSI Techniques in Application to HAWT and VAWT

## 4.1 Coupled FSI formulation

To state the FSI formulation with non-mathcing discretization between fluid and structure subdomains we used the approach that is based on augmented Lagrangian formulation (see [88] for more details). At a continuous level the coupled problem may be stated as: find $\mathbf{u}_1 \in \mathcal{S}_u$, $p \in \mathcal{S}_p$, and $\mathbf{u}_2 \in \mathcal{S}_d$, such that $\forall \mathbf{w}_1 \in \mathcal{V}_u$, $q \in \mathcal{V}_p$, and $\mathbf{w}_2 \in \mathcal{V}_d$,

$$
\begin{aligned}
& B_1(\{\mathbf{w}_1, q\}, \{\mathbf{u}_1, p\}; \hat{\mathbf{u}}) - F_1(\{\mathbf{w}_1, q\}) + B_2(\mathbf{w}_2, \mathbf{u}_2) - F_2(\mathbf{w}_2) \\
& - \int_{(\Gamma_t)_\mathrm{I}} (\mathbf{w}_1 - \mathbf{w}_2) \cdot \boldsymbol{\sigma}_1 (\mathbf{u}_1, p)\, \mathbf{n}_1 \, \mathrm{d}\Gamma \\
& - \int_{(\Gamma_t)_\mathrm{I}} \delta\boldsymbol{\sigma}_1 (\mathbf{w}_1, q)\, \mathbf{n}_1 \cdot (\mathbf{u}_1 - \mathbf{u}_2) \, \mathrm{d}\Gamma \\
& + \int_{(\Gamma_t)_\mathrm{I}} (\mathbf{w}_1 - \mathbf{w}_2) \cdot \beta(\mathbf{u}_1 - \mathbf{u}_2) \, \mathrm{d}\Gamma = 0.
\end{aligned} \tag{4.1}
$$

In the above equations, the subscripts 1 and 2 denote the fluid and structural mechanics quantities, and $\beta$ is a penalty parameter. In Eq. (4.1), $B_1$, $F_1$, $B_2$, and $F_2$ are the semi-linear forms and linear functionals corresponding to the fluid and structural mechanics problems defined by Eqs. (2.5) and (3.33), respectively. The last three terms of Eq. (4.1)

enforce weak compatibility of the kinematics and tractions at the fluid–structure interface $(\Gamma_t)_\mathrm{I}$. The proposed approach, in the continuum setting, provides a framework for formulating FSI methods to handle nonmatching fluid and structural interface discretizations.

In the variational formulation given by Eq. (4.1), the trial and test function spaces of the fluid and structural subproblems are independent of each other. By setting $\mathbf{w}_2 = 0$ the variational form of fluid mechanics problem with weak imposition of Dirichlet boundary condition on a fluid velocity may be obtained as

$$\begin{aligned} & B_1(\{\mathbf{w}_1, q\}, \{\mathbf{u}_1, p\}; \hat{\mathbf{u}}) - F_1(\{\mathbf{w}_1, q\}) \\ & - \int_{(\Gamma_t)_\mathrm{I}} \mathbf{w}_1 \cdot \boldsymbol{\sigma}_1 (\mathbf{u}_1, p)\, \mathbf{n}_1 \, \mathrm{d}\Gamma \\ & - \int_{(\Gamma_t)_\mathrm{I}} \delta\boldsymbol{\sigma}_1 (\mathbf{w}_1, q)\, \mathbf{n}_1 \cdot (\mathbf{u}_1 - \mathbf{u}_2) \, \mathrm{d}\Gamma \\ & + \int_{(\Gamma_t)_\mathrm{I}} \mathbf{w}_1 \cdot \tau_\mathrm{B} (\mathbf{u}_1 - \mathbf{u}_2) \, \mathrm{d}\Gamma = 0, \end{aligned} \tag{4.2}$$

where essential boundary conditions come from the structural velocity at the fluid-structure interface.

Setting $\{\mathbf{w}_1, q\} = 0$ gives the variational formulation of the structural mechanics problem:

$$B_2(\mathbf{w}_2, \mathbf{u}_2) - F_2(\mathbf{w}_2) - \int_{(\Gamma_t)_\mathrm{I}} \mathbf{w}_2 \cdot (-\boldsymbol{\sigma}_1 \mathbf{n}_1 - + \tau_\mathrm{B} (\mathbf{u}_1 - \mathbf{u}_2)) \, \mathrm{d}\Gamma = 0, \tag{4.3}$$

which states that at the fluid-structure interface the structural problem is driven by the fluid traction vector $\mathbf{t_1}$, that is a combination of the fluid Cauchy stress and a penalty force.

From Eqs. (4.2) and (4.3) it is clear, that the fluid mechanics problem is responsible for satisfying the kinematic compatibility condition, while the structural subproblem is responsible for satisfying the traction compatibility condition.

To conclude the coupled FSI formulation we present the equation of a mesh motion in the aerodynamics subdomain, which is governed by the equations of elastostatics

with jacobian-based stiffening- [45–49] to preserve the good mesh quality for the entire computation. In the continuum setting, the mesh displacement can be computed from the following variational formulation: find the mesh displacement from its referential configuration, $\hat{\mathbf{y}} \in \mathcal{S}_m$, such that $\forall \mathbf{w} \in \mathcal{V}_m$:

$$\int_{\Omega_{\tilde{t}}} \epsilon(\mathbf{w}) \cdot \mathbf{D}\epsilon(\hat{\mathbf{y}}(\mathbf{t}) - \hat{\mathbf{y}}(\tilde{\mathbf{t}}))\, \mathrm{d}\boldsymbol{\Omega} = \mathbf{0}, \tag{4.4}$$

where $\Omega_{\tilde{t}}$ and $\hat{\mathbf{y}}(\tilde{t})$ are the fluid subdomain and its displacement vector, respectively, at time $\tilde{t} < t$ and considered known, $\mathcal{S}_m$ and $\mathcal{V}_m$ are the sets of trial and test functions for the fluid-domain motion, $\epsilon$ is the strain vector evaluated using the spatial coordinate on $\Omega_{\tilde{t}}$, and $\mathbf{D}$ is the elasticity tensor (see [89] for more details).

The discretization of Eqs. (4.2-4.4) leads to a coupled, nonlinear equation system that need to be solved at every time step. Within each time step, the coupled equations are solved using an inexact Newton approach. In solving the linear equation systems involved at every nonlinear iteration, the GMRES search technique [90] is used with a diagonal preconditioner. A simple block-iterative FSI solution strategy [89] is employed to solve the coupled discrete FSI equations at each nonlinear iteration within a time step. The block-iterative approach is a strongly-coupled FSI technique where, at the level of nonlinear iterations, increments of the fluid, structure and mesh-moving discrete unknowns are computed sequentially as follows: 1. We obtain the fluid solution increment holding the structure and mesh fixed. 2. We update the fluid solution, compute the aerodynamic force on the structure and compute the structural solution increment. 3. We update the structural solution and use elastic mesh motion to update the fluid domain velocity and position.

## 4.2 A novel mesh moving technique for sliding interfaces in motion

To enable the FSI simulation of VAWT or the FSI simulations of HAWT during yawing rotation, a new mesh moving technique is developed and presented in this

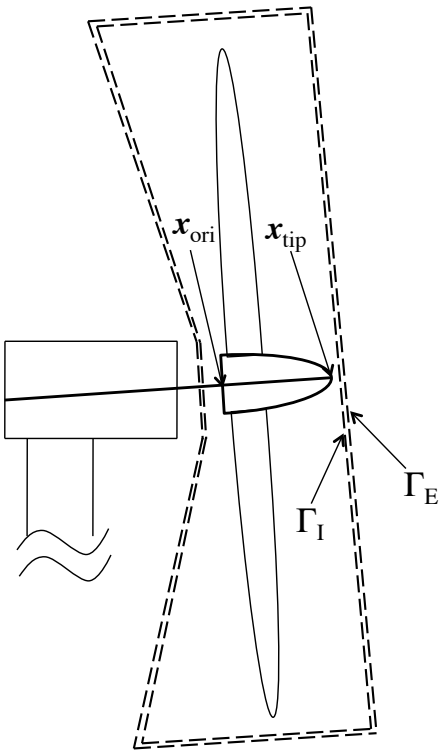


**Figure 4.1**: Illustration of the wind turbine, the sliding interface (dashed line), and the key locations on the nacelle. A slight offset is used to illustrate that the sliding interface has two definitions, $\Gamma_I$ and $\Gamma_E$. In the numerical formulation the two interfaces occupy the same region in 3D space.

section. We denote by $\Gamma_I$ and $\Gamma_E$ the two sides of the sliding interface coming from the interior and exterior subdomains (see Figure 4.1).

We begin with describing the motion of $\Gamma_I$. For this, we let $\mathbf{x}$ and $\mathbf{X}$ denote the position vector of the points on $\Gamma_I$ in the current and reference configuration, respectively. We define $\mathbf{x}_{ori}$ and $\mathbf{x}_{tip}$ to be the current-configuration positions of the back and tip of the nacelle (see Figure 4.1), and we let $\mathbf{X}_{ori}$ and $\mathbf{X}_{tip}$ be their reference-configuration counterparts. We restrict the motion of $\Gamma_I$ to be that of a rigid object and write

$$\mathbf{x} = \mathbf{R}(\mathbf{X} - \mathbf{X}_{ori}) + \mathbf{x}_{ori}. \tag{4.5}$$

While $\mathbf{x}_{ori}$ is obtained directly from the motion of the wind-turbine structure, the main challenge here is to obtain a suitable rotation matrix $\mathbf{R}$ in the above equation. For this,

we extract the instantaneous mean angular velocity of the wind-turbine rotor as

$$\boldsymbol{\omega} = \mathbf{J}^{-1}\mathbf{m}, \tag{4.6}$$

where $\mathbf{J}$ is the rotor moment-of-inertia tensor in the current configuration given by

$$\mathbf{J} = \int_{\Omega_R} \rho \left( (\mathbf{x} - \mathbf{x}_{\text{ori}}) \cdot (\mathbf{x} - \mathbf{x}_{\text{ori}})\mathbf{I} - (\mathbf{x} - \mathbf{x}_{\text{ori}}) \otimes (\mathbf{x} - \mathbf{x}_{\text{ori}}) \right) \, d\Omega, \tag{4.7}$$

and $\mathbf{m}$ is the rotor angular momentum given by

$$\mathbf{m} = \int_{\Omega_R} (\mathbf{x} - \mathbf{x}_{\text{ori}}) \times \rho \mathbf{u} \, d\Omega. \tag{4.8}$$

In the above integrals $\Omega_R$ is the rotor structural domain in the current configuration, $\rho$ is the rotor material density, $\mathbf{u}$ is the rotor velocity and $\mathbf{I}$ is the identity tensor. This technique of extracting $\boldsymbol{\omega}$ was recently employed in [91] to remove the spinning component of the structure in FSI modeling of parachute clusters.

Given the rotor instantaneous mean angular velocity $\boldsymbol{\omega}$, we compute the rotation matrix $\mathbf{R}$ needed in Eq. (4.5) using the following ODE (see, e.g., [81]):

$$\frac{\mathrm{d}}{\mathrm{d}t}\mathbf{R} = \boldsymbol{\omega} \times \mathbf{R}, \tag{4.9}$$

where the cross-product is taken column-wise.

To handle $\Gamma_E$ in the computations we use a similar approach. We also restrict the motion of $\Gamma_E$ to be that of a rigid object and write

$$\mathbf{x} = \mathbf{R}_\tau(\mathbf{X} - \mathbf{X}_{\text{ori}}) + \mathbf{x}_{\text{ori}}, \tag{4.10}$$

where the rotation matrix $\mathbf{R}_\tau$ is obtained from the ODE:

$$\frac{\mathrm{d}}{\mathrm{d}t}\mathbf{R}_\tau = \boldsymbol{\omega}_\tau \times \mathbf{R}_\tau. \tag{4.11}$$

The above ODE is driven by the angular velocity vector $\boldsymbol{\omega}_\tau$, which we define as

$$\boldsymbol{\omega}_\tau = \boldsymbol{\omega} - (\boldsymbol{\omega} \cdot \mathbf{n}_{\text{rot}})\mathbf{n}_{\text{rot}}, \tag{4.12}$$

where

$$\mathbf{n}_{\text{rot}} = \frac{\mathbf{x}_{\text{tip}} - \mathbf{x}_{\text{ori}}}{\|\mathbf{x}_{\text{tip}} - \mathbf{x}_{\text{ori}}\|}. \tag{4.13}$$

Equation (4.12) effectively removes the spinning component from the motion of $\Gamma_E$, as desired. The location of the nacelle tip $\mathbf{x}_{tip}$ is also obtained directly from the motion of the wind-turbine structure.

Both Eqs. (4.9) and (4.11) are integrated in time using the midpoint rule, which guarantees that $\mathbf{R}$ and $\mathbf{R}_\tau$ retain their orthonormal property, and thus remain true rotation matrices. This result is due to [92].

Long-time FSI simulations using of the above mesh-moving technique may encounter a slight misalignment between $\Gamma_I$ and $\Gamma_E$. In this case, it is necessary to periodically correct the motion of $\Gamma_E$ to make sure that it is aligned with $\Gamma_I$. This may be accomplished using a modified version of Eq. (4.10):

$$\mathbf{x} = \mathbf{R}_{cor}\mathbf{R}_\tau(\mathbf{X} - \mathbf{X}_{ori}) + \mathbf{x}_{ori}, \tag{4.14}$$

where $\mathbf{R}_{cor}$ is the rotation matrix between $\mathbf{n}_I$ and $\mathbf{n}_E$, the two outward unit normal vectors to $\Gamma_I$ and $\Gamma_E$, respectively. (That is, $\mathbf{R}_{cor}$ is such that $\mathbf{n}_I = \mathbf{R}_{cor}\mathbf{n}_E$.) The normal vectors may be taken, for example, on the inflow plane of the cylindrical domain. The matrix $\mathbf{R}_{cor}$ may be computed explicitly using the Rodrigues formula [93],

$$\mathbf{R}_{cor} = \cos\theta\mathbf{I} + \sin\theta\boldsymbol{\Upsilon} + (1 - \cos\theta)\mathbf{u} \otimes \mathbf{u}, \tag{4.15}$$

where $\theta$ is the angle between the two normal vectors, $\mathbf{u}$ is the rotation axis defined as

$$\mathbf{u} = \frac{\mathbf{n}_I \times \mathbf{n}_E}{\|\mathbf{n}_I \times \mathbf{n}_E\|}, \tag{4.16}$$

and the components of $\boldsymbol{\Upsilon}$ are given by

$$\Upsilon_{ik} = \varepsilon_{ijk}u_j, \tag{4.17}$$

where $\varepsilon_{ijk}$ are the components of the alternator tensor, and the Einstein summation convention is employed.

## 4.3 FSI simulations of the Micon 65/13M wind turbine

We start with the FSI simulations of the Micon 65/13M wind turbine [84] (see Figure 4.2). This is a three-blade, fixed-pitch, upwind turbine with the total rotor diameter of 19.3 m and rated power of 100 kW. The hub is located at the height of 23 m,

**Figure 4.2**: Micon 65/13M test wind turbine at the USDA-ARS site in Bushland, TX

with a mounting flange positioned 0.6 m from the centerline of the low-speed shaft. The wind turbine stands on a tubular steel tower, with a base diameter of 1.9 m. The drive train generator operates at 1200 rpm, while the rotor spins at a nominal speed of 55 rpm. The Micon 65/13M wind turbine was used for the Long-Term Inflow and Structural Testing (LIST) program [94] at the USDA-ARS test facility in Bushland, Texas. This project was initiated by Sandia National Laboratories in 2001 to explore the use of carbon fiber in wind turbine blades. The wind turbine is equipped with CX-100 blades, those structural model used in current FSI simulations was validated in Section 3.4.1.

FSI simulations of the full Micon 65/13M wind turbine are carried out at realistic operational condition. A constant inflow wind speed of 10.5 m/s and fixed rotor speed of 55 rpm are prescribed. These correspond to the operating conditions reported for the field tests in [84]. The air density and viscosity are 1.23 kg/m$^3$ and $1.78 \times 10^{-5}$ kg/(m·s), respectively. Zero traction boundary conditions are prescribed at the outflow and no-penetration boundary conditions are prescribed at the top, bottom, and side surfaces of the outer (stationary) computational domain. No-slip boundary conditions are prescribed at the rotor, nacelle, and tower, and are imposed weakly.

Figure 4.3 shows the computational domain and Figure 4.4 mesh used in this study. The mesh consists of 5,134,916 linear elements, which are triangular prisms in

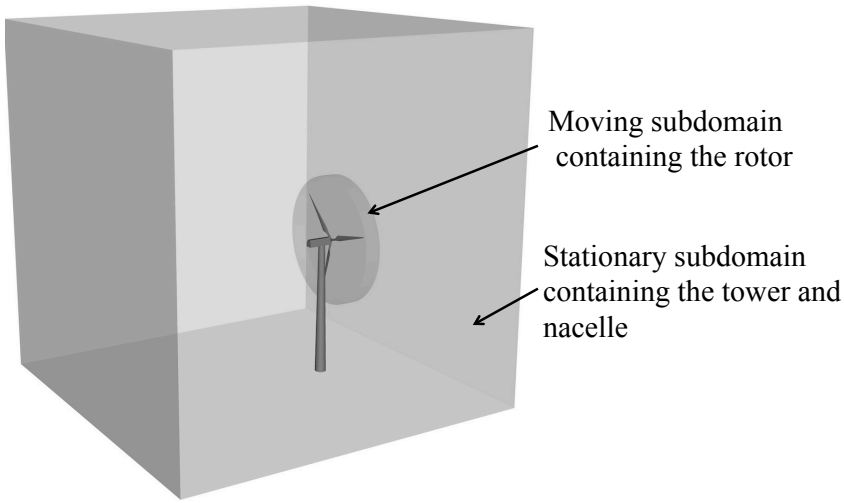


**Figure 4.3**: Setup for the full-wind-turbine simulation. An interior moving subdomain, which encloses the wind-turbine rotor, and an exterior stationary subdomain, which houses the nacelle and tower, are employed.

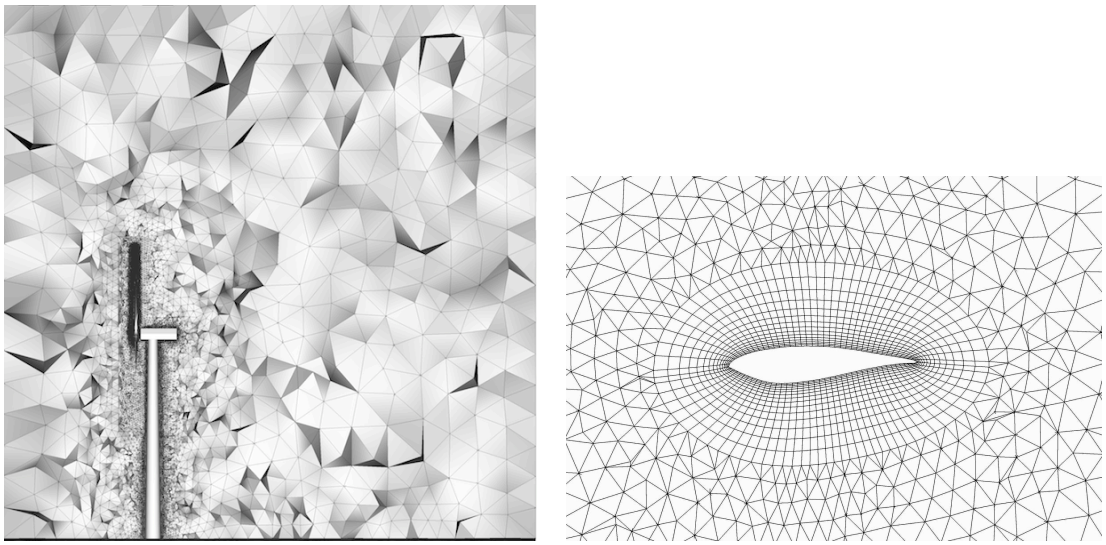

(a) (b)

**Figure 4.4**: (a) The computational domain and problem mesh with the refined inner region for better flow resolution near the rotor; (b) A 2D blade cross-section at $r/R = 70\%$ to illustrate the boundary-layer mesh.

the rotor boundary layers and tetrahedra everywhere else in the domain. The mesh is refined in the rotor and tower regions for better flow resolution near the wind turbine. The size of the first element in the wall-normal direction is 0.002 m, and 15 layers of prismatic elements were generated with a growth ratio of 1.2. Figure 4.4 shows a 2D blade cross-section at 70% spanwise station to illustrate the boundary-layer mesh used in the computations.

The computations were carried out in a parallel computing environment. The mesh is partitioned into subdomains using METIS [79], and each subdomain is assigned to a compute core. The parallel implementation of the methodology may be found in [95].

The fluid and structural equations are integrated in time using the Generalized-$\alpha$ method [69, 96, 97] with the time-step size of $3.0 \times 10^{-5}$ s for all cases. In each time step, block-iterative FSI coupling [49, 98, 99] is employed, which is efficient and stable for the application considered here.

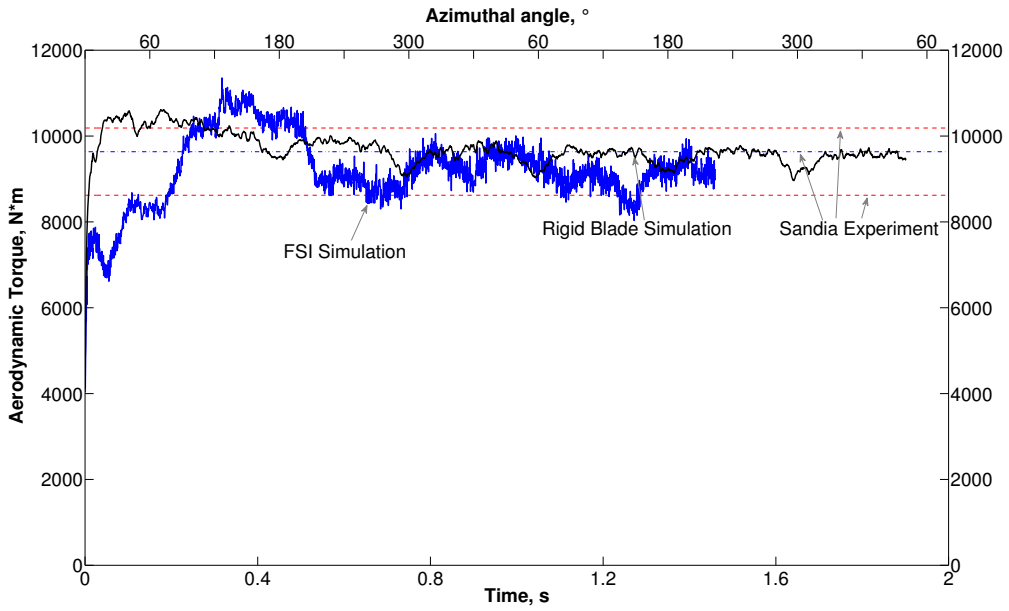


**Figure 4.5**: Aerodynamic torque history for the FSI and rigid-blade simulations. The experimental range for the aerodynamic torque and its average value are provided for comparison and are plotted using dashed lines.

In Figure 4.5 the time history of the aerodynamic torque is plotted. As can be

seen from the plot, using FSI, we capture the high frequency oscillations caused by the bending and torsional motions of the blades. In the case of the rigid blade the only high-frequency oscillations in the torque curve are due to the trailing-edge turbulence. For the rigid blade case the effect of the tower on the aerodynamic torque is more pronounced, while in the case of FSI it is not as visible due to the relatively high torque oscillations. The 'dips' in the aerodynamic torque can be seen at 60°, 180°, and 300° azimuthal angle, which is precisely when one of the three blades is passing the tower.

The computed values of the aerodynamic torque are plotted together with field test results from [84]. The upper and lower dashed lines indicate the aerodynamic torque bounds, while the middle dashed line gives its average value. Both the aerodynamic and FSI results compare very well with the experimental data.

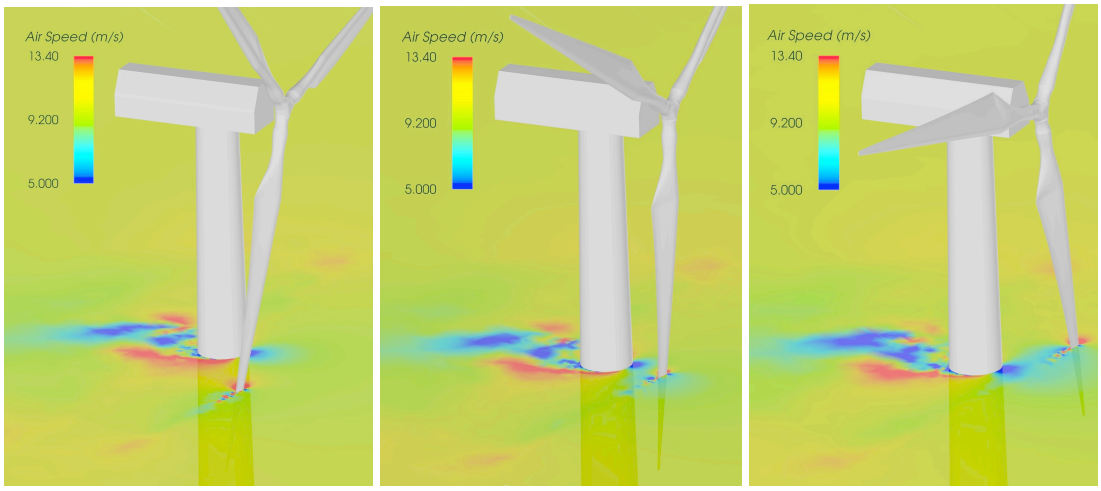


**Figure 4.6**: Wind speed contours at 80% spanwise station as the blade passes the tower.

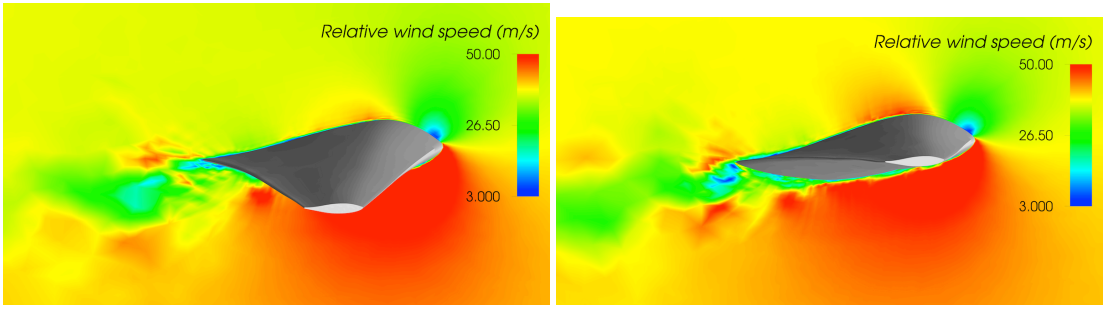


**Figure 4.7**: Relative wind speed at the 70% spanwise station for the FSI simulation at $t = 0.86$ s (left) and $t = 1.06$ s (right). The blade deflection is clearly visible.

Figure 4.6 shows the flow field as the blade passes the tower. Figure 4.7 shows the relative wind speed at the 70% spanwise station rotated to the reference configuration to illustrate the blade deflection and complexity of boundary-layer turbulent flow. Finally, isosurfaces of vorticity colored by flow speed are shown in Figure 4.8

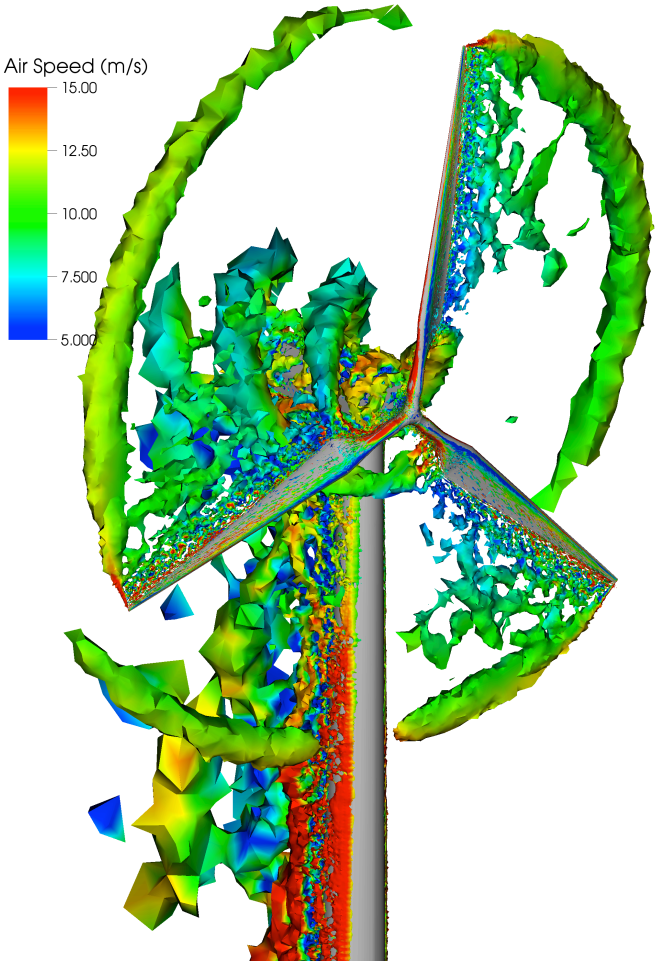


**Figure 4.8**: Vorticity isosurfaces at a time instant colored by velocity magnitude.

## 4.4 FSI simulations of a HAWT under yawing motion

We present a preliminary, ongoing FSI simulation of a 5MW offshore wind turbine undergoing yawing motion. The wind turbine is equipped with 61 m blades designed by Sandia. The structural model of a blade used in current FSI simulations was

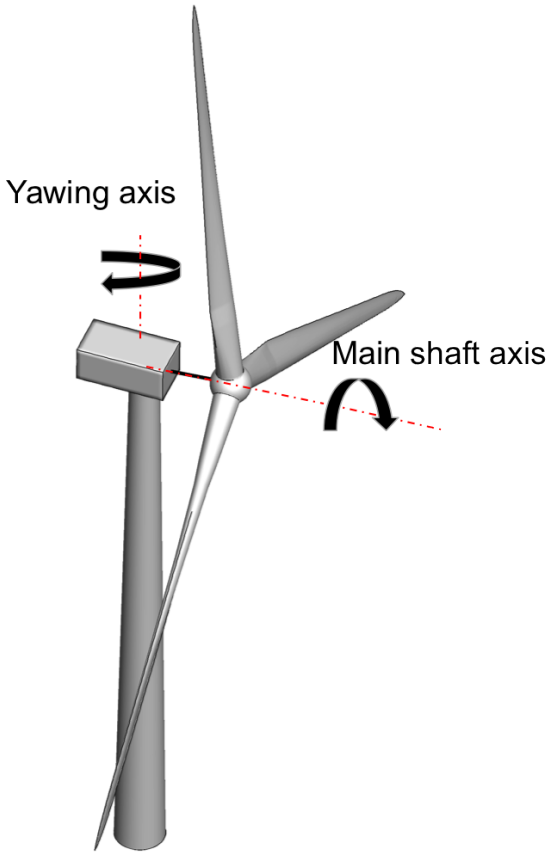


**Figure 4.9**: HAWT model with two main rotational axis.

validated in Section 3.4.2. The wind turbine rotor is positioned at 80 m above ground and is tilted by 5° to avoid the blade hitting the tower as the rotor spins. (Another way to have sufficient tower clearance is to "prebend" the rotor blades into the wind. See [100] for details.) Furthermore, the wind turbine rotor plane is initially placed at 15° relative to the wind direction. A fixed yawing rotational speed is applied to the gearbox to slowly turn the rotor into the wind at 0.03 rad/s (see Figure 4.9). The inflow wind speed is set to 11.4 m/s. The initial rotor speed is set to 12.1 rpm, and the rotor is allowed to spin freely during the prescribed yawing motion.

The structural mechanics mesh of the full turbine has 13,273 quadratic NURBS shell elements and two quadratic NURBS beam elements. The aerodynamics mesh has a total of 5,458,185 linear elements. Triangular prisms are employed in the blade boundary layers, and tetrahedral elements are used elsewhere in the aerodynamics domain.

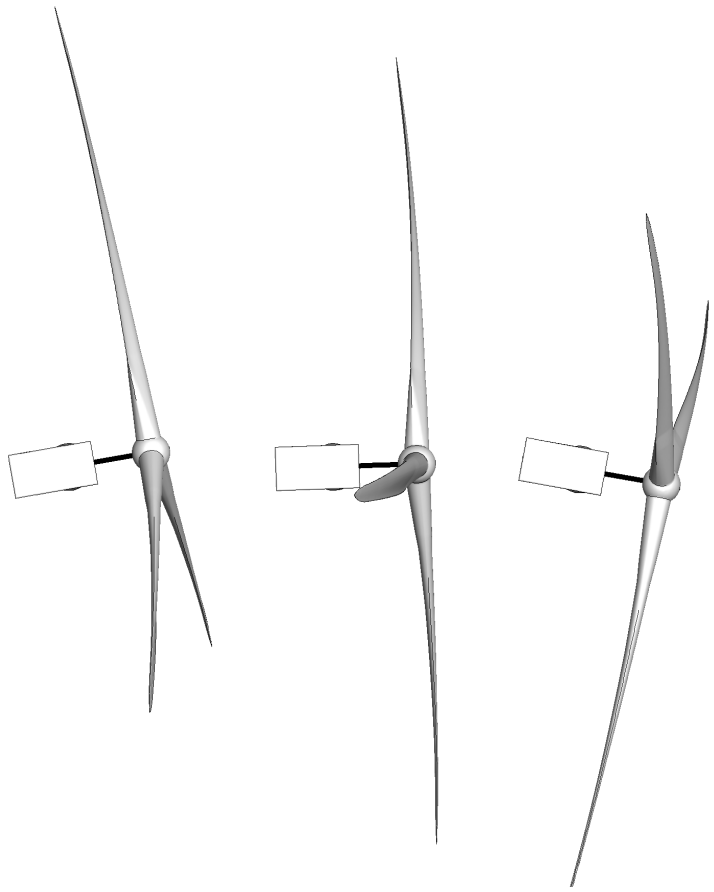

**Figure 4.10**: FSI simulation of a HAWT undergoing a yawing motion. Snapshots of the top view of the wind-turbine structure current configuration. The blades appear to be quite flexible and care needs to be taken when designing the rotating subdomain to avoid the flexing blade crossing its boundary.

The size of the first boundary-layer element in the wall-normal direction is 1 cm, and the time step of 0.0001 s is employed in the computation.

Snapshots of the structure deformed configuration are shown in Figure 4.10, while isosurfaces of vorticity colored by flow speed are shown in Figure 4.11. Figures 4.12 and 4.13 show the time history of the axial component of the aerodynamic torque and angular speed (i.e., the component in the direction of the vector $\mathbf{n}_{\text{rot}}$ in Eq. (4.13)). Both are slowly increasing as the rotor turns into the wind, as expected. The level of the computed aerodynamic torque is consistent with the earlier simulations

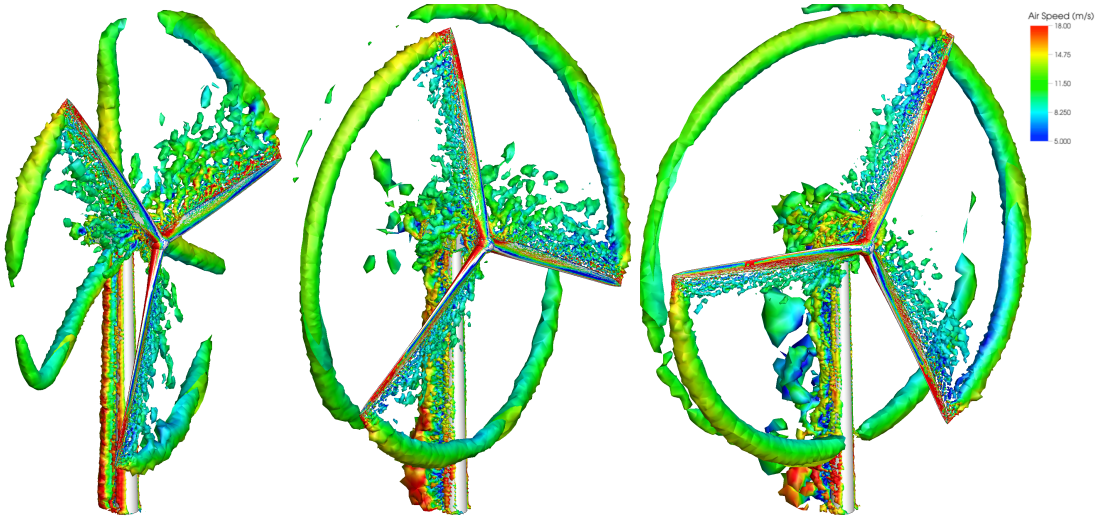


**Figure 4.11**: FSI simulation of a HAWT undergoing a yawing motion. Snapshots of vorticity colored by air speed illustrating the air flow complexity.

for this wind turbine operating under similar wind- and rotor-speed conditions (see, e.g., [5, 18, 21, 22, 25, 27, 50]).

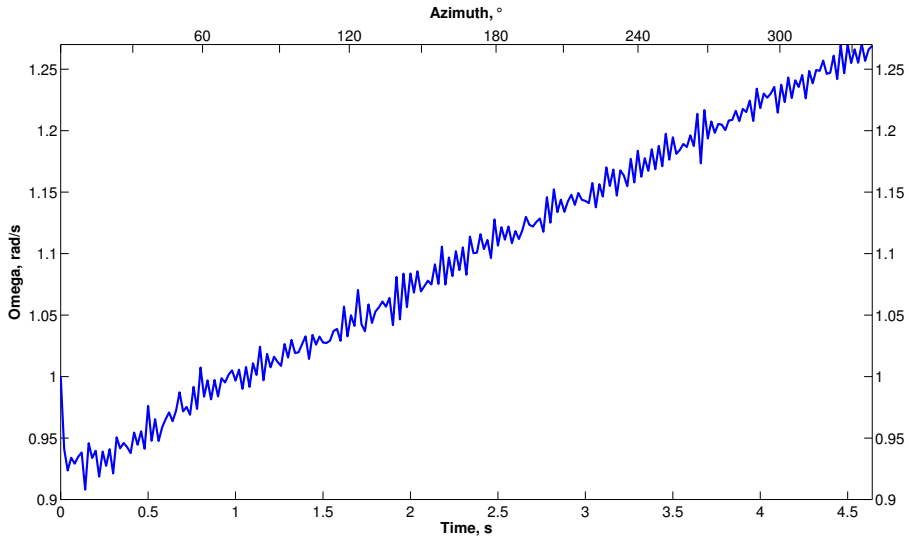


**Figure 4.12**: FSI simulation of a HAWT undergoing a yawing motion. Time history of the angular speed.

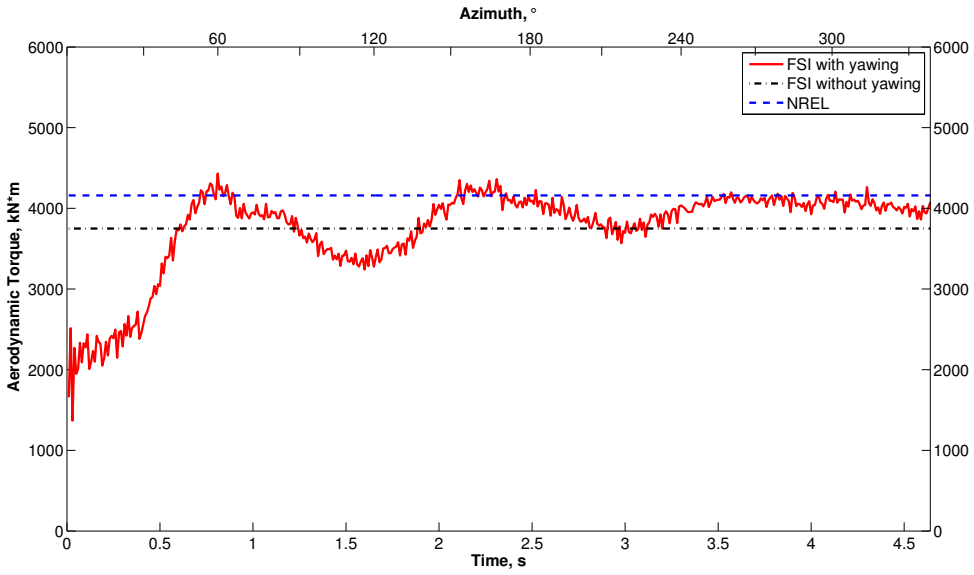


**Figure 4.13**: FSI simulation of a HAWT undergoing a yawing motion. Time history of the rotor aerodynamic torque.

## 4.5 FSI simulations of the Windspire VAWT and start-up issue in VAWTs

We present an FSI simulation of a 1.2 kW VAWT, which is a three-bladed, medium-solidity Darrieus turbine designed by Windspire Energy [36]. The details of wind turbine geometry together with aerodynamic validation using a field-test data are presented in Section 2.3.2. The structural model is presented in Figure 4.14. The rotor and struts are made of aluminum, and the tower is made of steel. Quadratic NURBS are employed for both the beam and shell discretizations. The total number of beam elements is 116, and total number of shell elements is 7,029.

As a part of FSI simulations, we perform a preliminary investigation of the start-up issues in VAWTs using the FSI methodology described earlier and the structural model of the Windspire design. We fix the inflow wind speed at 11.4 m/s, and consider three initial rotor speeds: 0 rad/s, 4 rad/s and 12 rad/s. Of interest is the transient response of the system. In particular, we will focus on how the rotor angular speed responds to the prescribed initial conditions, and what is the range of the tower tip

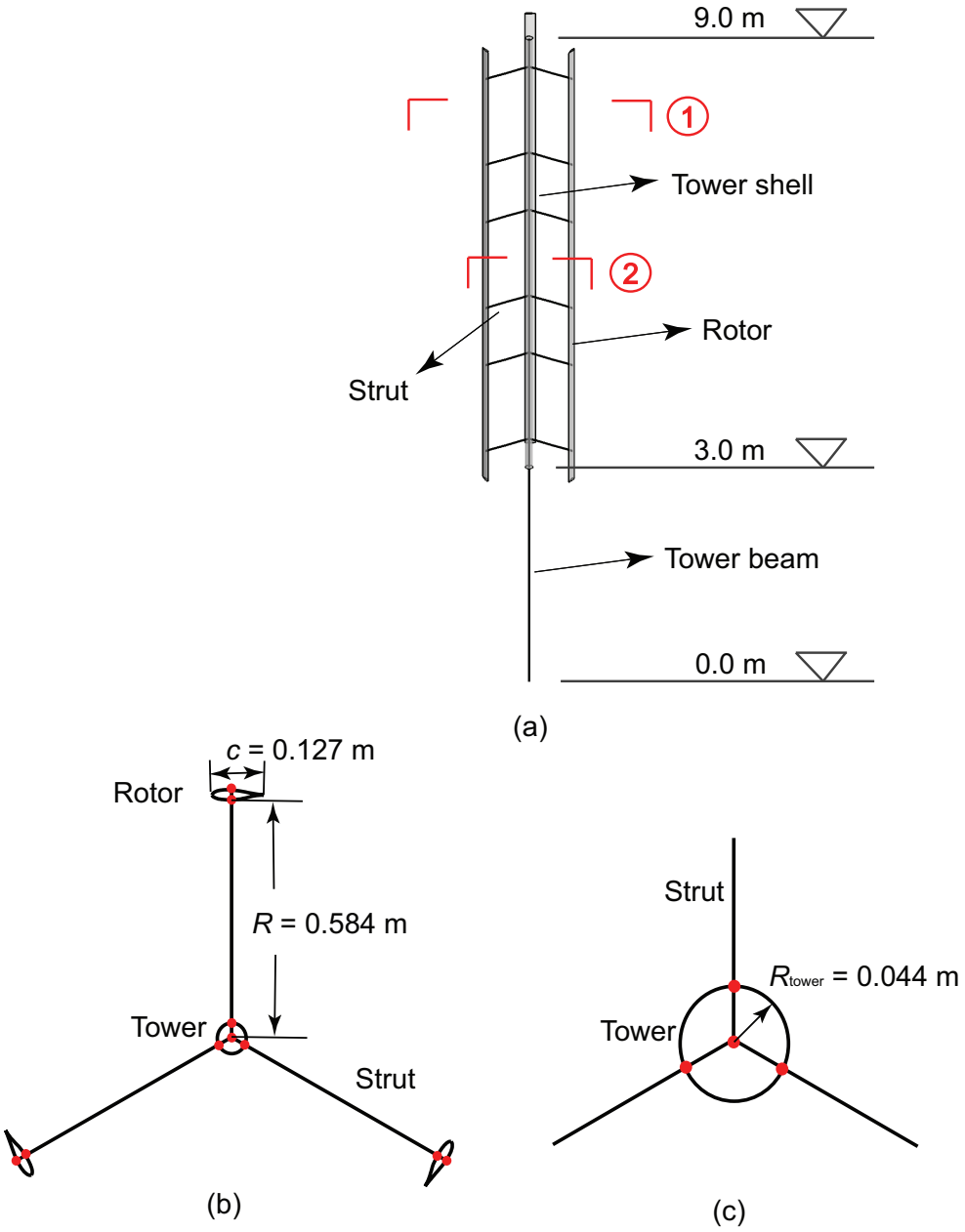


**Figure 4.14**: Windspire VAWT structural model with dimensions included: (a) Full model using isogeometric NURBS-based rotation-free shells and beams; (b) Model cross-section 1 showing attachment of the struts to the blades and tower shell; (c) Model cross-section 2 showing attachment of the struts and tower shell.

displacement during the VAWT operation. The VAWT is allowed to spin freely and accelerate under the action of the ambient wind. The time step in the computations is set to $2.0 \times 10^{-5}$ s.

The mesh moving technique described in Section 4.2 is applied to this case in a straightforward fashion. The radius and height of the inner cylindrical domain that encloses the rotor are 1.6 m and 7 m, respectively. That is, the cylindrical domain extends 0.5 m above and below the rotor blades. The rotor axis direction $\mathbf{n}_{\text{rot}}$ is defined according to Eq. (4.13), where the points $\mathbf{x}_{\text{ori}}$ and $\mathbf{x}_{\text{tip}}$ are located at the bottom and top intersections of the tower beam and shell, respectively. The instantaneous rotor angular velocity is computed from Eq. (4.6), the spinning component is removed as per Eq. (4.12), and the two angular velocities are used to update the sliding-interface mesh positions. We fluid mesh was adopted from the aerodynamics simulations presented in Section 2.3.2

The time history of rotor speed is shown in Figures 4.15–4.17. For the 0 rad/s case the rotor speed begins to increase suggesting this configuration is favorable for self-starting. For the 4 rad/s case, the rotor speed has a nearly linear acceleration region

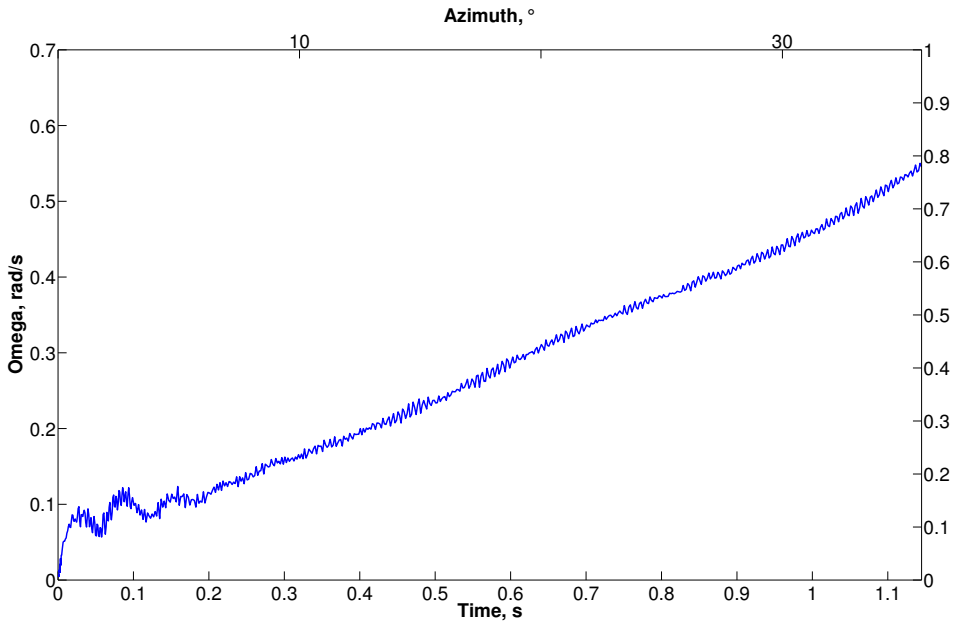


**Figure 4.15**: Time history of the rotor speed starting from 0 rad/s.

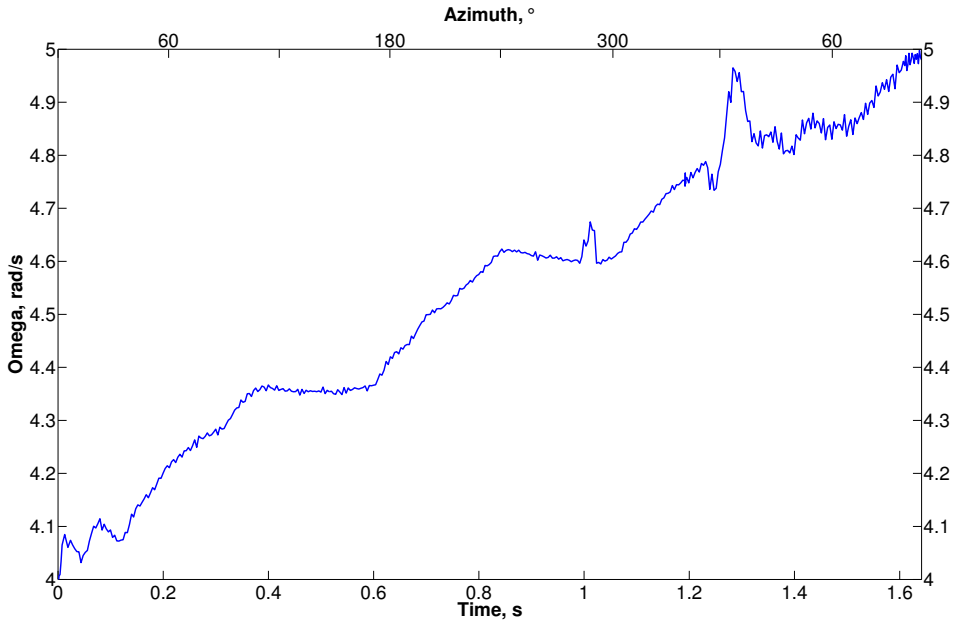


**Figure 4.16**: Time history of the rotor speed starting from 4 rad/s.

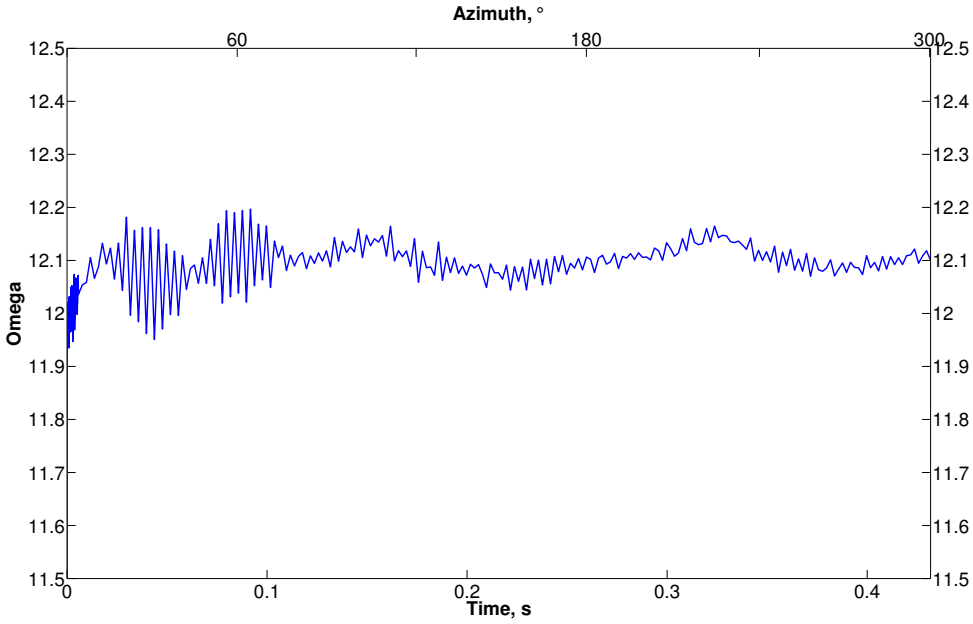


**Figure 4.17**: Time history of the rotor speed starting from 12 rad/s.

followed by a *plateau* region. In [16] the plateau region is defined as the regime when the turbine operates at nearly constant (i.e., steady-state like) rotational speed. From the angular position of the blades in Figure 4.16 it is evident that the plateau region occurs approximately every 120° when one of the blades is in a stalled position. It lasts until the blade clears the stalled region, and the lift forces are sufficiently high for the rotational speed to start increasing again. As the rotational speed increases, the angular velocity is starting to exhibit local unsteady behavior in the plateau region. While the overall growth of the angular velocity for the 4 rad/s case is promising for the VAWT to self start, the situation is different for the 12 rad/s case (see Figure 4.17). Here the rotor speed has little dependence on the angular position and stays nearly constant, close to its initial value. It is not likely that the rotor speed will reach to the operational levels in these conditions without an applied external torque, or a sudden change in wind speed,

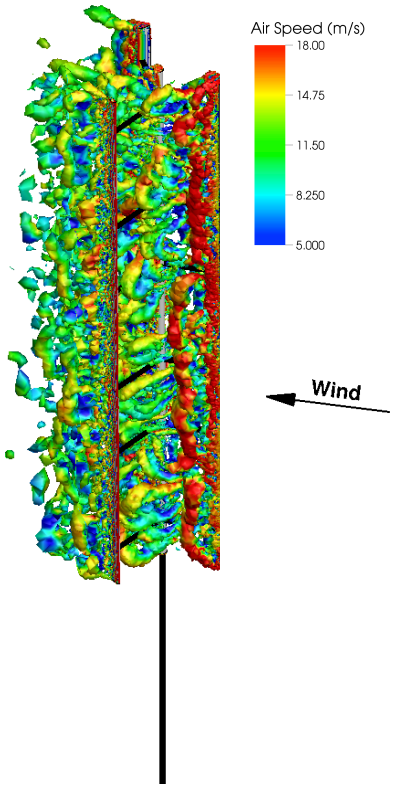


**Figure 4.18**: Vorticity isosurfaces at a time instant colored by velocity magnitude for the 4 rad/s case.

which is consistent with the findings of [17].

Figure 4.18 shows, for a full turbine, a snapshot of vorticity colored by flow speed for the 4 rad/s case. Figure 4.19 zooms on the rotor and shows several flow vorticity snapshots during the rotation cycle. The figures indicate the complexity of the underlying flow phenomena and the associated computational challenges. Note the presence of quasi-2D vortex tubes that are created due to massive flow separation, and that quickly disintegrate and turn into fine-grained 3D turbulence further downstream.

Figure 4.20 shows the turbine current configuration at two time instances during the cycle for the 4 rad/s case. The displacement is mostly in the direction of the wind, however, lateral tower displacements are also observed as a result of the rotor spinning motion. The displacement amplitude is around 0.10-0.12 m, which we find reasonable given the tower height of 9 m, and one of the VAWT design objectives being that the structure is not too flexible. This is also the case for the 0 rad/s and 12 rad/s cases.

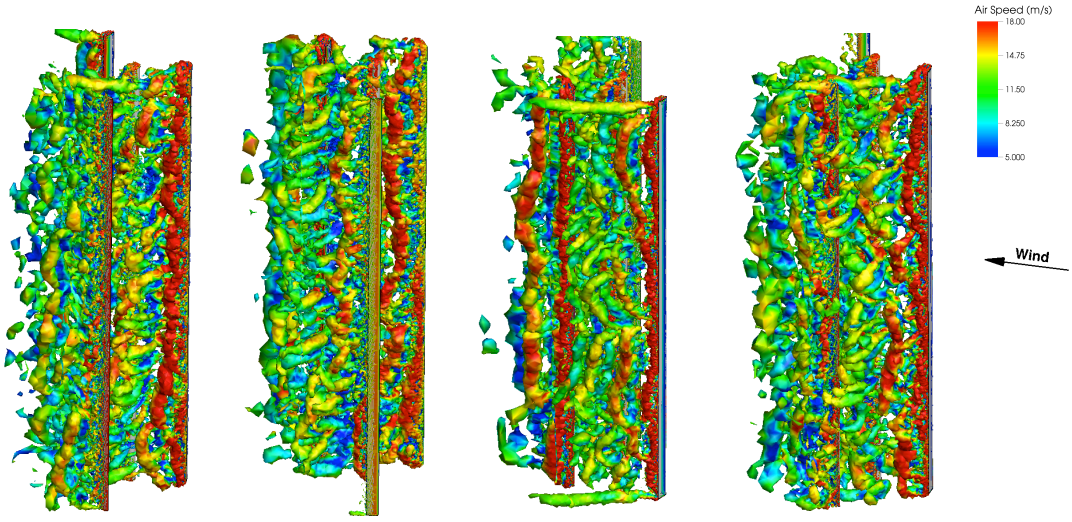


**Figure 4.19**: Vorticity isosurfaces of vorticity colored by velocity magnitude for the 4 rad/s case. Zoom on the rotor. From left to right: Vorticity at 1.12 s,1.24 s,1.40 s and 1.50 s.

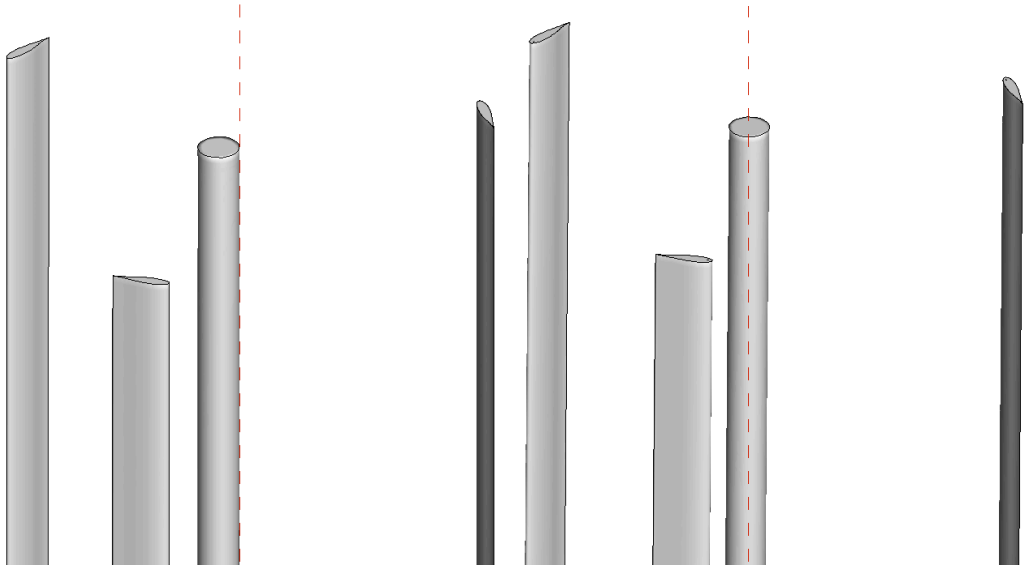

**Figure 4.20**: Turbine current configuration at two time instances for the 4 rad/s case. The tower centerline in the reference configuration is shown using the dashed line to illustrate the range of turbine motion during the cycle. The range of the tower tip displacement during the cycle is about 0.10-0.12 m.

## 4.6 Acknowledgements

Chapter 4, in part, is a reprint of the material as it appears in: "Structural mechanics modeling and FSI simulation of wind turbines," (with M.-C. Hsu, I. Akkerman, J. Tippmann and Y. Bazilevs), *Mathematical Models and Methods in Applied Science*, 2013 and "FSI Modeling of Vertical- Axis Wind Turbines," (with Y. Bazilevs, X. Deng, J. Yan, M. Kinzel and J.O. Dabiri), *Journal of Applied Mechanics*, 2014 and "Novel Structural Modeling and Mesh Moving Techniques for Advanced FSI Simulation of Wind Turbines," (with Y. Bazilevs, X. Deng and J. Yan), *International Journal for Numerical Methods in Engineering*, 2014. The dissertation author was the primary investigator and author of this paper.

# Chapter 5

# Conclusions

In this dissertation more advanced FSI simulations of wind turbines, such as rotor yawing for HAWTs, and full-machine FSI of VAWTs were targeted. A structural model of wind turbines design was constructed and discretized using the recently-proposed isogeometric rotation-free shell and beam formulations. This approach presents a good combination of accuracy due to the structural geometry representation using smooth, higher-order functions, and efficiency due to the fact that only displacement degrees of freedom are employed in the formulation. By constructing a detailed material model of wind turbine blade with non-symmetric, multilayer layup we were able to reproduce the experimentally measured eigenfrequencies of the CX-100 blade of Micon 65/13M HAWT. To our knowledge, this is the first full-scale validation of the IGA-based thin-shell composite formulation.

The ALE-VMS technique for aerodynamics modeling was augmented with an improved version of the sliding interface formulation, which allows the interface to move in space as a rigid object and accommodate the global turbine deflections in addition to the rotor spinning motion. We performed a detailed validation study on a full scale Darrieus H-type VAWT. The pure aerodynamics computation produced good agreement with reported wind tunnel and field-test data. A simulation of two side-by-side wind turbines was also performed.

Using novel mesh moving techniques we were able to simulate a large scale 5MW HAWT undergoing yawing motion. We also present FSI simulations of full-scale Micon 65/13M wind turbine with the CX-100 blades mounted on its rotor. The results

of the aerodynamic and FSI simulations shows a good agreement with field test data for this wind turbine. The FSI simulation captures high-frequency oscillations in the aerodynamic torque, which are caused by the blade structural response. In the future work we plan to explore methods and devices to mitigate such high-frequency rotor vibrations.

Dynamic FSI modeling of VAWTs in 3D and at full scale were reported for the first time in this dissertation with investigation of turbine start-up issues. From the FSI computations we see that for given wind conditions the rotor naturally accelerates at lower values of angular speed. However, as the angular speed grows, the rotor may encounter a dead band region. That is, the turbine self-starts, but then it is trapped in a lower rotational speed than is required for optimal performance, and some additional input (e.g., a wind gust or applied external torque) is required to get the rotor to accelerate further. There may be multiple dead band regions that the turbine needs to overcome, with external forcing applied, before it reaches the target rotational speed. In the future, to address some of these issues, we plan to couple our FSI formulation with an appropriate control strategy (see, e.g., [101]) to simulate more realistic VAWT operation scenarios.

The numerical examples presented in this dissertation illustrate the successful application of the proposed techniques to the FSI simulation of wind turbines at full scale.

# Bibliography


[1] J. O. Dabiri. Potential order-of-magnitude enhancement of wind farm power density via counter-rotating vertical-axis wind turbine arrays. *Journal of Renewable and Sustainable Energy*, 3:043104, 2011.

[2] Caltech field laboratory for optimized wind energy (flowe). Available at: http://dabiri.caltech.edu/research/wind-energy.html.

[3] A. Huskey, A. Bowen, and D. Jager. Wind turbine generator system power performance test report for the mariah windspire 1-kw wind turbine. *National Renewable Energy Laboratory Technical Report NREL/TP-500-46192*, 2009.

[4] D. T. Griffith and T. D. Ashwill. The Sandia 100-meter all-glass baseline wind turbine blade: SNL100-00. *Sandia Report SAND2011-3779*, 2011.

[5] Y. Bazilevs, M.-C. Hsu, I. Akkerman, S. Wright, K. Takizawa, B. Henicke, T. Spielman, and T. E. Tezduyar. 3D simulation of wind turbine rotors at full scale. Part I: Geometry modeling and aerodynamics. *International Journal for Numerical Methods in Fluids*, 65:207–235, 2011.

[6] J. Bennett. The effect of mass and web spacing on the loads and structural response of increasing wind turbine blade size. *MS Thesis, Royal Institute of Technology, Sweden*, 2012.

[7] Renewable power generation costs in 2012: An overview. Technical report, International Renewable Energy Agency, 2012. Available at: http://www.irena.org/Publications/.

[8] Annual energy outlook 2014, doe/eia-0383(2014). Report, U.S. Energy Information Administration, April 2014. Available at: http://www.eia.gov/forecasts/aeo/.

[9] Eu energy in figures, statistical pocketbook 2014. Report, European Commission, 2014. doi:10.2833/24150.

[10] Levelized cost of electricity renewable energy technologies. Study, FRAUNHOFER INSTITUT FOR SOLAR ENERGY SYSTEMS ISE, November 2013.

[11] L. Vita, U. S. Paulsen, and T. F. Pedersen. A novel floating offshore wind turbine concept: New developments. *in: EWEC 2010, URL http://www.ewec2010.info/index.php?id=182*, 2010.

[12] L. Vita, U. S. Paulsen, H. A. Madsen, H. P. Nielsen, P. A. Berthelsen, and S. Cartsensen. Design and aero-elastic simulation of a 5mw floating vertical axis wind turbine. *(omae2012-83470), in: Proceedings of the 31st International Conference on Ocean, Offshore, and Arctic Engineering, Rio de Janeiro, Brazil*, 7:383–393, 2012, ISBN 978-0-7918-4494-6.

[13] E. Hau. *Wind Turbines: Fundamentals, Technologies, Application, Economics. 2nd Edition*. Springer, Berlin, 2006.

[14] B. Kirke and L. Lazauskas. Enhancing the performance if a vertical axis wind turbine using a simple variable pitch system. *Wind Engineering*, 15(4):187–195, 1991.

[15] R. Dominy, P. Lunt, A. Bickerdyke, and J. Dominy. Self-starting capability of a darrieus turbine. *Proceedings of the Institution of Mechanical Engineers, Part A: Journal of Power and Energy*, 221(1):111–120, 2007.

[16] N. Hill, R. Dominy, G. Ingram, and J. Dominy. Darrieus turbines: the physics of self-starting. *Proc. IMechE Part A: J. Power and Energy*, 223(1):21–29, 2009.

[17] J. R. Baker. Features to aid or enable self starting of xed pitch low solidity vertical axis wind turbines. *J. Wind Eng. Ind. Aerodyn.*, 15:369–380, 1983.

[18] Y. Bazilevs, M.-C. Hsu, J. Kiendl, R. Wüchner, and K.-U. Bletzinger. 3D simulation of wind turbine rotors at full scale. Part II: Fluid–structure interaction modeling with composite blades. *International Journal for Numerical Methods in Fluids*, 65:236–253, 2011.

[19] R. Chow and C. P. van Dam. Verification of computational simulations of the NREL 5 MW rotor with a focus on inboard flow separation. *Wind Energy*, 2012. doi:10.1002/we.529.

[20] A. Bechmann, N. N. Sørensen, and F. Zahle. CFD simulations of the MEXICO rotor. *Wind Energy*, 14:677–689, 2011.

[21] K. Takizawa, B. Henicke, T. E. Tezduyar, M.-C. Hsu, and Y. Bazilevs. Stabilized space–time computation of wind-turbine rotor aerodynamics. *Computational Mechanics*, 48:333–344, 2011.

[22] K. Takizawa, B. Henicke, D. Montes, T. E. Tezduyar, M.-C. Hsu, and Y. Bazilevs. Numerical-performance studies for the stabilized space–time computation of wind-turbine rotor aerodynamics. *Computational Mechanics*, 48:647–657, 2011.

[23] N. N. Sørensen and S. Schreck. Computation of the National Renewable Energy Laboratory Phase-VI rotor in pitch motion during standstill. *Wind Energy*, 2012. doi:10.1002/we.480.

[24] Ming-Chen Hsu, I. Akkerman, and Y. Bazilevs. Finite element simulation of wind turbine aerodynamics: Validation study using NREL Phase VI experiment. *Wind Energy*, published online, DOI: 10.1002/we.1599, 2013.

[25] K. Takizawa, T. E. Tezduyar, S. McIntyre, N. Kostov, R. Kolesar, and C. Habluetzel. Space–time VMS computation of wind-turbine rotor and tower aerodynamics. *Computational Mechanics*, 53:1–15, 2014.

[26] A. Korobenko, M.C. Hsu, I. Akkerman, J. Tippmann, and Y. Bazilevs. Structural mechanics modeling and fsi simulation of wind turbines. *Mathematical Models and Methods in Applied Science*, 23:249–272, 2013.

[27] M.-C. Hsu and Y. Bazilevs. Fluid–structure interaction modeling of wind turbines: simulating the full machine. *Computational Mechanics*, 50:821–833, 2012.

[28] Y. Bazilevs, A. Korobenko, X. Deng, and J. Yan. Novel structural modeling and mesh moving techniques for advanced fsi simulation of wind turbines. *International Journal for Numerical Methods in Engineering*, 2014.

[29] P. Stein, M.-C. Hsu, Y. Bazilevs, and K. Beucke. Operator- and template-based modeling of solid geometry for isogeometric analysis with application to vertical axis wind turbine simulation. *Computer Methods in Applied Mechanics and Engineering*, 213–216:71–83, 2012.

[30] F. Scheurich, T. Fletcher, and R. Brown. Simulating the aerodynamic performance and wake dynamics of a vertical-axis wind turbine. *Wind Energy*, 14:159–177, 2011. Published online. DOI: 10.1002/we.409.

[31] F. Scheurich and R. Brown. Modelling the aerodynamics of vertical-axis wind turbines in unsteady wind conditions. *Wind Energy*, 2012. Published online. DOI: 10.1002/we.532.

[32] K. McLaren, S. Tullis, and S. Ziada. Computational fluid dynamics simulation of the aerodynamics of a high solidity, small-scale vertical axis wind turbine. *Wind Energy*, 15:349–361, 2012. Published online. DOI: 10.1002/we.472.

[33] A. Korobenko, M.-C. Hsu, I. Akkerman, and Y. Bazilevs. Aerodynamic simulation of vertical-axis wind turbines. *Journal of Applied Mechanics*, 81(2):021011, 2013.

[34] J. M. Jonkman and M. L. Buhl Jr. FAST user's guide. Technical Report NREL/EL-500-38230, National Renewable Energy Laboratory, Golden, CO, 2005.

[35] P. C. Klimas. Darrieus rotor aerodynamics. *Transactions of the ASME. Journal of Solar Energy Engineering*, 104:102–105, 1982.

[36] Windspire energy. Available at: http://www.windspireenergy.com/.

[37] Y. Bazilevs, Ming-Chen Hsu, K. Takizawa, and T. E. Tezduyar. ALE-VMS and ST-VMS methods for computer modeling of wind-turbine rotor aerodynamics and fluid–structure interaction. *Mathematical Models and Methods in Applied Sciences*, 22(supp02):1230002, 2012.

[38] Y. Bazilevs, M.-C. Hsu, J. Kiendl, R. Wuechner, and K.-U. Bletzinger. 3D simulation of wind turbine rotors at full scale. part II: Fluid-structure interaction. *International Journal of Numerical Methods in Fluids*, 65:236–263, 2011.

[39] T. J. R. Hughes, W. K. Liu, and T. K. Zimmermann. Lagrangian–Eulerian finite element formulation for incompressible viscous flows. *Computer Methods in Applied Mechanics and Engineering*, 29:329–349, 1981.

[40] K. Takizawa, Y. Bazilevs, and T. E. Tezduyar. Space–time and ALE-VMS techniques for patient-specific cardiovascular fluid–structure interaction modeling. *Archives of Computational Methods in Engineering*, to appear, 2011.

[41] Y. Bazilevs and T. J. R. Hughes. Weak imposition of Dirichlet boundary conditions in fluid mechanics. *Computers and Fluids*, 36:12–26, 2007.

[42] Y. Bazilevs, C. Michler, V. M. Calo, and T. J. R. Hughes. Weak Dirichlet boundary conditions for wall-bounded turbulent flows. *Computer Methods in Applied Mechanics and Engineering*, 196:4853–4862, 2007.

[43] Y. Bazilevs, C. Michler, V. M. Calo, and T. J. R. Hughes. Isogeometric variational multiscale modeling of wall-bounded turbulent flows with weakly enforced boundary conditions on unstretched meshes. *Computer Methods in Applied Mechanics and Engineering*, 199:780–790, 2010.

[44] M.-C. Hsu, I. Akkerman, and Y. Bazilevs. Wind turbine aerodynamics using ALE–VMS: Validation and the role of weakly enforced boundary conditions. *Computational Mechanics*, 50:499–511, 2012. doi:10.1007/s00466-012-0686-x.

[45] T. E. Tezduyar, M. Behr, S. Mittal, and A. A. Johnson. Computation of unsteady incompressible flows with the finite element methods – space–time formulations, iterative strategies and massively parallel implementations. In *New Methods in Transient Analysis*, PVP-Vol.246/AMD-Vol.143, pages 7–24, New York, 1992. ASME.

[46] T. Tezduyar, S. Aliabadi, M. Behr, A. Johnson, and S. Mittal. Parallel finite-element computation of 3D flows. *Computer*, 26(10):27–36, 1993.

[47] A. A. Johnson and T. E. Tezduyar. Mesh update strategies in parallel finite element computations of flow problems with moving boundaries and interfaces. *Computer Methods in Applied Mechanics and Engineering*, 119:73–94, 1994.

[48] T. E. Tezduyar. Finite element methods for flow problems with moving boundaries and interfaces. *Archives of Computational Methods in Engineering*, 8:83–130, 2001.

[49] T. E. Tezduyar and S. Sathe. Modeling of fluid–structure interactions with the space–time finite elements: Solution techniques. *International Journal for Numerical Methods in Fluids*, 54:855–900, 2007.

[50] Y. Bazilevs, Ming-Chen Hsu, and M. A. Scott. Isogeometric fluid–structure interaction analysis with emphasis on non-matching discretizations, and with application to wind turbines. *Computer Methods in Applied Mechanics and Engineering*, 249-252:28–41, 2012.

[51] Y. Bazilevs and T. J. R. Hughes. NURBS-based isogeometric analysis for the computation of flows about rotating components. *Computational Mechanics*, 43:143–150, 2008.

[52] J. Kiendl, K.-U. Bletzinger, J. Linhard, and R. Wüchner. Isogeometric shell analysis with Kirchhoff–Love elements. *Computer Methods in Applied Mechanics and Engineering*, 198:3902–3914, 2009.

[53] J. Kiendl, Y. Bazilevs, M.-C. Hsu, R. Wüchner, and K.-U. Bletzinger. The bending strip method for isogeometric analysis of Kirchhoff–Love shell structures comprised of multiple patches. *Computer Methods in Applied Mechanics and Engineering*, 199:2403–2416, 2010.

[54] S.B. Raknes, X. Deng, Y. Bazilevs, D.J. Benson, K.M. Mathisen, and T. Kvamsdal. Isogeometric rotation-free bending-stabilized cables: Statics, dynamics, bending strips and coupling with shells. *Computer Methods in Applied Mechanics and Engineering*, 263:127–143, 2013.

[55] T. J. R. Hughes, J. A. Cottrell, and Y. Bazilevs. Isogeometric analysis: CAD, finite elements, NURBS, exact geometry, and mesh refinement. *Computer Methods in Applied Mechanics and Engineering*, 194:4135–4195, 2005.

[56] J. A. Cottrell, T. J. R. Hughes, and Y. Bazilevs. *Isogeometric Analysis: Toward Integration of CAD and FEA*. Wiley, Chichester, 2009.

[57] L. Piegl and W. Tiller. *The NURBS Book (Monographs in Visual Communication), 2nd ed.* Springer-Verlag, New York, 1997.

[58] R. Bravo, S. Tullis, and S. Ziada. Performance testing of a small vertical-axis wind turbine. *Proceedings of the 21st Canadian Congress of Applied Mechanics*, pages 470–471, 2007.

[59] Y. Bazilevs, V. M. Calo, J. A. Cottrel, T. J. R. Hughes, A. Reali, and G. Scovazzi. Variational multiscale residual-based turbulence modeling for large eddy simulation of incompressible flows. *Computer Methods in Applied Mechanics and Engineering*, 197:173–201, 2007.

[60] I. Akkerman, Y. Bazilevs, V. M. Calo, T. J. R. Hughes, and S. Hulshoff. The role of continuity in residual-based variational multiscale modeling of turbulence. *Computational Mechanics*, 41:371–378, 2008.

[61] I. Akkerman, Y. Bazilevs, C. E. Kees, and M. W. Farthing. Isogeometric analysis of free-surface flow. *Journal of Computational Physics*, 230:4137–4152, 2011.

[62] A. N. Brooks and T. J. R. Hughes. Streamline upwind/Petrov-Galerkin formulations for convection dominated flows with particular emphasis on the incompressible Navier-Stokes equations. *Computer Methods in Applied Mechanics and Engineering*, 32:199–259, 1982.

[63] T. J. R. Hughes and T. E. Tezduyar. Finite element methods for first-order hyperbolic systems with particular emphasis on the compressible Euler equations. *Computer Methods in Applied Mechanics and Engineering*, 45:217–284, 1984.

[64] T. E. Tezduyar and Y. J. Park. Discontinuity capturing finite element formulations for nonlinear convection-diffusion-reaction equations. *Computer Methods in Applied Mechanics and Engineering*, 59:307–325, 1986.

[65] T. J. R. Hughes, L. P. Franca, and M. Balestra. A new finite element formulation for computational fluid dynamics: V. Circumventing the Babuška–Brezzi condition: A stable Petrov–Galerkin formulation of the Stokes problem accommodating equal-order interpolations. *Computer Methods in Applied Mechanics and Engineering*, 59:85–99, 1986.

[66] T. E. Tezduyar and Y. Osawa. Finite element stabilization parameters computed from element matrices and vectors. *Computer Methods in Applied Mechanics and Engineering*, 190:411–430, 2000.

[67] T. E. Tezduyar. Computation of moving boundaries and interfaces and stabilization parameters. *International Journal for Numerical Methods in Fluids*, 43:555–575, 2003.

[68] T. J. R. Hughes, G. Scovazzi, and L. P. Franca. Multiscale and stabilized methods. In E. Stein, R. de Borst, and T. J. R. Hughes, editors, *Encyclopedia of Computational Mechanics, Vol. 3, Fluids*, chapter 2. Wiley, 2004.

[69] Y. Bazilevs, V. M. Calo, T. J. R. Hughes, and Y. Zhang. Isogeometric fluid–structure interaction: theory, algorithms, and computations. *Computational Mechanics*, 43:3–37, 2008.

[70] M.-C. Hsu, Y. Bazilevs, V. M. Calo, T. E. Tezduyar, and T. J. R. Hughes. Improving stability of stabilized and multiscale formulations in flow simulations at small time steps. *Computer Methods in Applied Mechanics and Engineering*, 199:828–840, 2010.

[71] Y. Bazilevs and I. Akkerman. Large eddy simulation of turbulent Taylor–Couette flow using isogeometric analysis and the residual–based variational multiscale method. *Journal of Computational Physics*, 229:3402–3414, 2010.

[72] K. Takizawa and T. E. Tezduyar. Multiscale space–time fluid–structure interaction techniques. *Computational Mechanics*, 48:247–267, 2011.

[73] C. Johnson. *Numerical solution of partial differential equations by the finite element method*. Cambridge University Press, Sweden, 1987.

[74] S. C. Brenner and L. R. Scott. *The Mathematical Theory of Finite Element Methods, 2nd ed.* Springer, 2002.

[75] A. Ern and J. L. Guermond. *Theory and Practice of Finite Elements*. Springer, 2004.

[76] D. N. Arnold, F. Brezzi, B. Cockburn, and L. D. Marini. Unified analysis of Discontinuous Galerkin methods for elliptic problems. *SIAM Journal of Numerical Analysis*, 39:1749–1779, 2002.

[77] T. E. Tezduyar, M. Behr, and J. Liou. A new strategy for finite element computations involving moving boundaries and interfaces – the deforming-spatial-domain/space–time procedure: I. The concept and the preliminary numerical tests. *Computer Methods in Applied Mechanics and Engineering*, 94(3):339–351, 1992.

[78] T. E. Tezduyar, M. Behr, S. Mittal, and J. Liou. A new strategy for finite element computations involving moving boundaries and interfaces – the deforming-spatial-domain/space–time procedure: II. Computation of free-surface flows, two-liquid flows, and flows with drifting cylinders. *Computer Methods in Applied Mechanics and Engineering*, 94(3):353–371, 1992.

[79] G. Karypis and V. Kumar. A fast and high quality multilevel scheme for partitioning irregular graphs. *SIAM Journal on Scientific Computing*, 20:359–392, 1999.

[80] M.-C. Hsu, I. Akkerman, and Y. Bazilevs. High-performance computing of wind turbine aerodynamics using isogeometric analysis. *Computers & Fluids*, 49:93–100, 2011.

[81] T. Belytschko, W. K. Liu, and B. Moran. *Nonlinear Finite Elements for Continua and Structures*. Wiley, 2000.

[82] M. Bischoff, W. A. Wall, K. -U. Bletzinger, and E. Ramm. Models and finite elements for thin-walled structures. In E. Stein, R. de Borst, and T. J. R. Hughes, editors, *Encyclopedia of Computational Mechanics, Vol. 2, Solids, Structures and Coupled Problems*, chapter 3. Wiley, 2004.

[83] J. N. Reddy. *Mechanics of Laminated Composite Plates and Shells: Theory and Analysis, 2nd ed.* CRC Press, Boca Raton, FL, 2004.

[84] J.R. Zayas and W.D. Johnson. 3X-100 blade field test. *Wind Energy Technology Department, Sandia National Laboratories*, page Report, 2008.

[85] D. Berry and T. Ashwill. Design of 9-meter carbon-fiberglass prototype blades: CX-100 and TX-100. 2007. Report of the Sandia National Laboratories.

[86] J.R. White, D.E. Adams, and M.A.Rumsey. Modal analysis of CX-100 rotor blade and Micon 65/13 wind turbine. pages Structural Dynamics and Renewable Energy, Volume 1, Conference Proceedings of the Society for Experimental Mechanics Series 10, 2011.

[87] T. Marinone, B. LeBlanc, J. Harvie, C. Niezrecki, and P. Avitabile. Modal testing of a 9 m CX-100 turbine blades. pages Topics in Experimental Dynamics Substructuring and Wind Turbine Dynamics, Volume 2, Conference Proceedings of the Society for Experimental Mechanics Series 27, 2012.

[88] Y. Bazilevs, M.-C. Hsu, and M. A. Scott. Isogeometric fluid–structure interaction analysis with emphasis on non-matching discretizations, and with application to wind turbines. *Computer Methods in Applied Mechanics and Engineering*, 249-252:28–41, 2012. doi:10.1016/j.cma.2012.03.028.

[89] Y. Bazilevs, K. Takizawa, and T. E. Tezduyar. *Computational Fluid–Structure Interaction: Methods and Applications*. Wiley, 2013.

[90] Y. Saad and M. Schultz. GMRES: A generalized minimal residual algorithm for solving nonsymmetric linear systems. *SIAM Journal of Scientific and Statistical Computing*, 7:856–869, 1986.

[91] K. Takizawa, T. E. Tezduyar, J. Boben, N. Kostov, C. Boswell, and A. Buscher. Fluid–structure interaction modeling of clusters of spacecraft parachutes with modified geometric porosity. *Computational Mechanics*, 52:1351–1364, 2013.

[92] T. J. R. Hughes and J. Winget. Finite rotation effects in numerical integration of rate constitutive equations arising in large-deformation analysis. *International Journal for Numerical Methods in Engineering*, 15:1862–1867, 1980.

[93] O. Rodrigues. Des lois geometriques qui regissent les deplacements dun systeme solide dans lespace, et de la variation des coordonnees provenant de ces deplacements consideres independamment des causes qui peuvent les produire. *Journal de Mathematiques*, 5:380–440, 1840.

[94] J. H. Sutherland, P. L. Jones, and B.A. Neal. The long-term inflow and structural test program. 2001. Proceedings of the 2001 ASME Wind Energy Symposium, p.162.

[95] M.-C. Hsu, I. Akkerman, and Y. Bazilevs. High-performance computing of wind turbine aerodynamics using isogeometric analysis. *Computers & Fluids*, 49:93–100, 2011.

[96] J. Chung and G. M. Hulbert. A time integration algorithm for structural dynamics withimproved numerical dissipation: The generalized-$\alpha$ method. *Journal of Applied Mechanics*, 60:371–75, 1993.

[97] K. E. Jansen, C. H. Whiting, and G. M. Hulbert. A generalized-$\alpha$ method for integrating the filtered Navier-Stokes equations with a stabilized finite element method. *Computer Methods in Applied Mechanics and Engineering*, 190:305–319, 2000.

[98] T. E. Tezduyar, S. Sathe, and K. Stein. Solution techniques for the fully-discretized equations in computation of fluid–structure interactions with the space–time formulations. *Computer Methods in Applied Mechanics and Engineering*, 195:5743–5753, 2006.

[99] T. E. Tezduyar, S. Sathe, R. Keedy, and K. Stein. Space–time finite element techniques for computation of fluid–structure interactions. *Computer Methods in Applied Mechanics and Engineering*, 195:2002–2027, 2006.

[100] Y. Bazilevs, M.-C. Hsu, J. Kiendl, and D. J. Benson. A computational procedure for prebending of wind turbine blades. *International Journal for Numerical Methods in Engineering*, 89:323–336, 2012.

[101] Y. Bazilevs, M. C. Hsu, and M. T. Bement. Adjoint-based control of fluid–structure interaction for computational steering applications. *Procedia Computer Science*, 18:1989–1998, 2013.